Atomistic Simulations of Dislocation Core Reconfiguration in FCC Metals and Alloys

By

Anas Abu-Odeh

A dissertation submitted in partial satisfaction of the

requirements for the degree of

Doctor of Philosophy

in

Engineering - Materials Science and Engineering

in the

Graduate Division

of the

University of California, Berkeley

Committee in charge:

Professor Mark Asta, Chair
Professor Daryl Chrzan
Professor Peter Hosemann

Spring 2023

Atomistic Simulations of Dislocation Core Reconfiguration in FCC Metals and Alloys

Abstract

Atomistic Simulations of Dislocation Core Reconfiguration in FCC Metals and Alloys

by

Anas Abu-Odeh

Doctor of Philosophy in Engineering - Materials Science and Engineering

University of California, Berkeley

Professor Mark Asta, Chair

Dislocations are line defects present in crystalline materials that govern the plastic deformation of metals and metallic alloys. These defects are described by continuum approaches in the far field, but the center of a dislocation core requires atomistic detail. The computational efficiency of continuum approaches allows for the use of mesoscale models probing length and time scales beyond those available in atomistic simulations. However, many of the assumptions involved which sacrifice finer details associated with dislocation core reconfiguration have been left unchecked. This dissertation presents the methodology and results of atomistic simulations applied to three main dislocation processes relevant for mesoscale modeling of FCC metals and alloys. The first is the process of dislocation climb, where dislocations migrate through the absorption/emission of point defects. Mesoscale models typically assume a dislocation to be an ideal cylindrical sink. This assumption is only valid when there is a sufficient density of jogs along the dislocation line, and through the combination of atomistic calculations of jog free energies and analytical theory, it is shown that obtaining such a sufficient density of jogs requires high homologous temperatures and/or a high supersaturation of defects. The second application is on the process of dislocation cross-slip in the presence of short-range ordering (SRO). Mesoscale models typically do not include the effect of solutes on cross-slip, and if they do, assume them to be distributed in a random fashion instead of having SRO. Through the atomistic calculation of many dislocation cross-slip energy barriers with and without the presence of SRO, it is shown that the effect of SRO on planar defect energies can significantly increase the cross-slip energy barrier, potentially reducing cross-slip rates by orders of magnitude and altering work-hardening processes during deformation. The third and final application is on the process of core restructuring of Lomer/Lomer-Cottrell dislocations as a function of stress and alloy composition. Mesoscale models assume that these dislocations, which are central to the work-hardening of FCC metals and alloys, evolve under stress through only one mechanism. It is shown through atomistic simulations that a variety of evolution mechanisms, including twin nucleation, can occur through the core restructuring of these dislocations depending on the local stress and alloy composition.

Contents

Acknowledgments

I would like to thank my father, my mother, and my brother for being my most consistent source of grounding and happiness. I would also like to thank Kahraman Demir and Haider Ali Bhatti for helping me persevere through lockdown lunacy.

I would like to thank my advisor, Mark Asta, for his great guidance, patience, encouragement, and willingness to have a discussion with me about anything. I would also like to thank Maeva Cottura and Tarun Allaparti, as their help and contributions allowed for the completion of this work. I would also like to thank Andrew Minor, John W. Morris Jr., Daryl Chrzan, and David Olmsted for many fruitful discussions as they served as inspiration and litmus tests for many of the ideas presented here.

There were multiple financial sources that made it possible for me to carry out the work in this dissertation. I would like to acknowledge a fellowship through the National Science Foundation Graduate Fellowship Research Program (Grant No. DGE 1752814). I would also like to acknowledge funding from the U.S. Office of Naval Research under grant No. N00014-17-1-2283. I would also like to acknowledge a fellowship from the UC National Laboratory Fees Research Program of the University of California, Grant Number L21GF3646.

This work made use of computational resources provided by the Extreme Science and Engineering Discovery Environment (XSEDE), which is supported by National Science Foundation under Grant No. ACI-1548562, as well as use of the Savio computational cluster resource provided by the Berkeley Research Computing program at the University of California, Berkeley (supported by the UC Berkeley Chancellor, Vice Chancellor for Research, and Chief Information Officer).

Chapter 1

Introduction

Dislocations are line defects in crystalline materials that are responsible for the majority of plastic deformation in metals and metallic alloys. They are characterized by a Burgers vector ($\vec{b}$) and a line direction ($\vec{l}$). The Burgers vector defines the displacement that results between two crystalline regions after a dislocation glides in the slip plane that separates them. The angle between the Burgers vector and the line direction defines the dislocation's character (edge, mixed, or screw), which carry different types of displacement fields. The different types of displacement fields associated with different dislocation characters result in different dislocation-defect interactions, including dislocation-dislocation, dislocation-vacancy, and dislocation-solute interactions. Fully understanding the physical underpinnings of the mechanical properties of metals and metallic alloys requires an in-depth understanding of a variety of dislocation interactions and behaviors at different length scales. This dissertation focuses on a narrow, but crucial, aspect of dislocation behavior that impacts creep and work-hardening behavior in face-centered cubic (FCC) crystal structures: dislocation core reconfiguration.

1.1 Modeling Dislocation Behavior across Length and Time Scales

While dislocation behavior directly impacts experimentally measurable properties of materials, it is remarkably difficult to probe the reconfiguration process of dislocation cores through experimental techniques as they occur on small length (∼nm) and time ($\sim10^{-13}$ s) scales. Computer modeling and simulation provides an attractive alternative approach to study such phenomena as a variety of techniques exist to probe dislocation behavior at a variety of length and time scales (Figure 1.1).

On the smaller end of the scale spectrum exist simulations based on density-functional theory (DFT), which is an ab-initio technique that provides approximations for the electronic energy that governs the quantum-mechanical bonding between atoms. This allows for direct calculation of the lattice constant, elastic constants, stacking fault energies, and compact dislocation core structures and energies [1]. The computational expense of DFT calculations becomes prohibitive when including only a few hundred atoms. Thus, while DFT calculations provide valuable insight, they are not well suited for non-compact dislocation cores as well as dislocation reconfiguration processes that occur at the nanometer scale or higher.

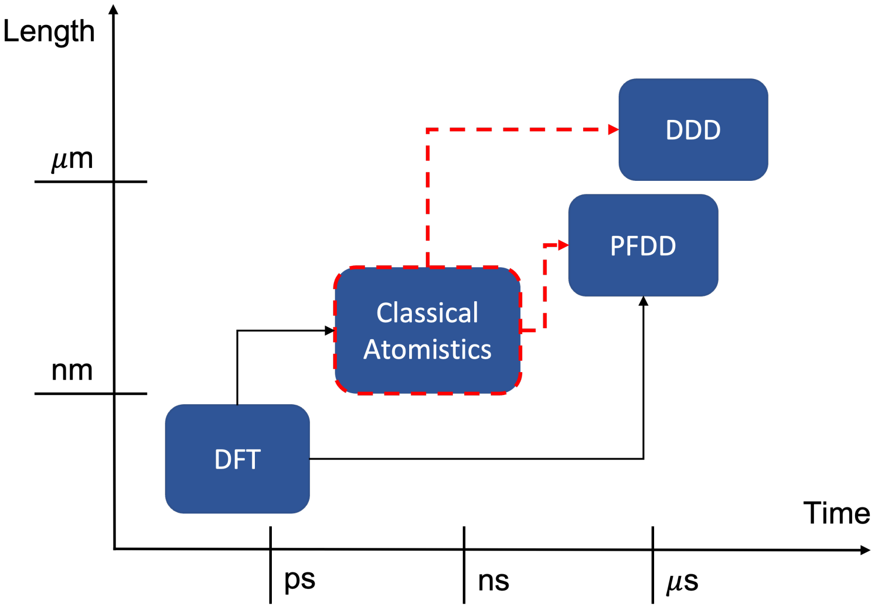

Figure 1.1: Various simulation methodologies to model dislocation phenomena across length and time scales. The dashed red lines represent the scale of focus of this dissertation as well as the potential impact on larger scale modeling.

Classical atomistic simulations alleviate some of these difficulties. These techniques use descriptions of atomic bonding, known as interatomic potentials, that circumvent the need for the explicit representation of electrons, and instead provide the energy of an atomic configuration as a function of the coordinates of the atoms. Interatomic potentials can be fit to DFT reference data. This allows for a significant increase in computational efficiency compared to DFT calculations, and have recently allowed for simulations of hundreds of millions of atoms [2]. As classical atomistic simulations allow for the efficient probing of dislocation core reconfiguration at atomic resolution, this will be the technique of choice in this dissertation. While appropriate for the studies presented in later chapters, classical atomistic simulations still suffer from simulating ensembles of dislocations due to being limited to high dislocation densities and strain-rates. This makes them generally ill-suited for modeling creep and work-hardening behavior.

Mesoscale modeling techniques such as discrete dislocation dynamics (DDD) and phase-field dislocation dynamics (PFDD) can circumvent these issues [3]. DDD simulations do not require the representation of atoms and instead focus on the representation of dislocations as connected nodes. The motion of these nodes are updated over time based on a given mobility parameter and a driving force based on the applied stress, elastic energy, and dislocation core energy. The generation and annihilation of dislocation segments and junctions follow predefined rules. Due to the nodal representation of dislocations and rule-based topological evolution, DDD represents the most computationally efficient way to simulate ensembles of dislocations [4, 5]. PFDD adopts a different approach and instead represents regions in a material volume by order parameters which describe whether a plane has been affected by dislocation slip. Dislocation cores are represented as interfaces between regions of slip, and the motion of these interfaces are dictated by a kinetic equation that depends on a free energy functional of the order parameter. PFDD is a flexible technique that allows for both simulation of dislocation cores [6] and ensembles of dislocations [7] (although not as efficiently as DDD), as well as, through the appropriate modification of the free energy functional, interactions with other microstructural features (e.g., precipitates [8] and grain boundaries [9]). While both DDD and PFDD (as well as other techniques) can be useful tools at the mesoscale, they rely on simplifying assumptions that can modify the evolution of a system of dislocations. Additionally, they are strongly dependent on parameterization from lower length scale models (DFT and classical atomistics).

The insights from classical atomistic simulations presented in this dissertation serve not only to further fundamental understanding of dislocation core reconfiguration, but also to challenge prevailing assumptions used in mesoscale modeling. It is anticipated that these insights will aid in the development of future mesoscale models, which will lead to better linkages between results from atomistic simulations and mechanical properties observed from experiments.

1.2 Dislocations in FCC Crystals

The dominant type of dislocations in FCC crystals lie on $\{111\}$ type slip planes and have a Burgers vector of $\frac{a}{2}\langle\bar{1}10\rangle$ type, where a is the lattice constant. FCC metals and alloys tend to be ductile due to the presence of twelve independent slip systems (four $\{111\}$ slip planes with three $\langle\bar{1}10\rangle$ slip directions each) [10]. While plastic deformation is largely governed by the ability for dislocations to glide in these slip systems, the ability for dislocations to reconfigure their cores can strongly impact creep and work-hardening behaviors. Additionally, special types of dislocations that do not lie on $\{111\}$ slip planes play an important role in work-hardening. Here, a brief review of the salient features of edge, screw, and Lomer dislocations in FCC metals and alloys is given.

Edge Dislocations

Edge dislocations, as well as dislocations with different characters, on $\{111\}$ slip planes tend to be dissociated in FCC systems (Figure 1.2). Instead of an initial "perfect" edge dislocation with a Burgers vector of $\vec{b}_e$, the dislocation adopts a configuration of two partial dislocations, with Burgers vectors of $\vec{b}_{pl}$ and $\vec{b}_{pt}$ (the sum of which equals $\vec{b}_e$) for the leading and trailing partial dislocations, respectively. As the elastic energy of a dislocation scales with $|\vec{b}|^2$, the dissociated configuration is more energetically favorable than the "perfect" configuration as $|\vec{b}_{pl}|^2+|\vec{b}_{pt}|^2$ is less than $|\vec{b}_e|^2$. The partial dislocations are separated by a stacking fault, which is representative of a region of lattice plane stacking that resembles a hexagonal close packed (HCP) lattice rather than a FCC lattice. The dissociation distance between the two partial dislocations is determined by minimizing the contributions of the interaction energy between them in addition with the stacking fault energy.

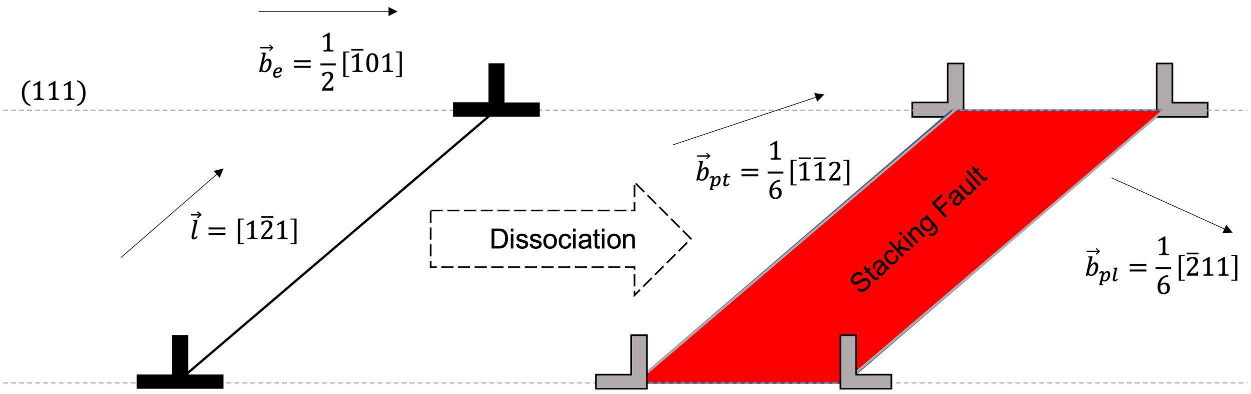

Figure 1.2: Dissociation of a "perfect" edge dislocation to a dissociated edge dislocation on a (111) plane. The black line and symbols represent a "perfect" edge dislocation, the grey lines and symbols represent partial dislocations, and the red region is the stacking fault.

Edge dislocations carry with them both compressive and tensile pressure fields on opposite sides of the slip plane [10]. This causes them to interact strongly with point defects that have a volumetric misfit. In alloys with solutes that contain large misfit volumes, this is expected to strongly influence an edge dislocation's resistance to glide [11]. This is also expected to cause a strong attraction of both vacancies and self-interstitials, which allows for an edge dislocation to act as a sink for these defects. When these point defects are absorbed at the core of a dislocation, regions of the dislocation migrate to {111} planes parallel to the initial slip plane through a process known as dislocation climb [12]. The ability for an edge dislocation to climb influences high-temperature deformation processes, annealing of quenched in defects, and irradiation-induced creep. The process of dislocation climb requires the dislocation core to reconfigure in away to nucleate defects known as jogs. The free energy of nucleation of these defects affects the rate of dislocation climb, and is the subject of Chapter 3.

Screw Dislocations

Similar to edge dislocations, screw dislocations on {111} slip planes in FCC systems tend to be dissociated as it reduces the elastic energy of the dislocation (Figure 1.3). While "perfect" screw dislocations do not have an appreciable pressure field, the partial dislocations have some edge character which can cause them to have somewhat stronger interactions with point defects.

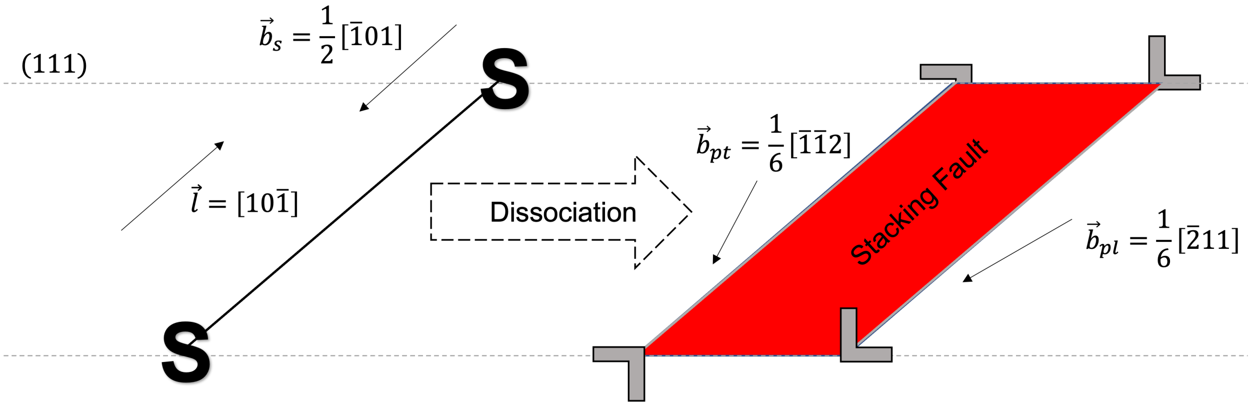

Figure 1.3: Dissociation of a "perfect" screw dislocation to a dissociated screw dislocation on a (111) plane. The black line and symbols represent a "perfect" screw dislocation, the grey lines and symbols represent partial dislocations, and the red region is the stacking fault.

As screw dislocations have the net Burgers vector and line direction to be parallel (or anti-parallel) to each other, this allows them to glide on {111} planes that intersect an original {111} slip plane. The process of a screw dislocation switching slip planes is known as cross-slip, and the rate of cross-slip of screw dislocations is expected to influence work-hardening behavior [13]. When screw dislocations are dissociated, the cross-slip process requires a reconfiguration of the dislocation core. The details of this reconfiguration are strongly dependent on the local chemical environment in an alloy, and can lead to a variety of cross-slip energy barriers. The effect of short-range ordering of solutes on cross-slip energy barriers in an alloy is the subject of Chapter 4.

Lomer Dislocations

Lomer dislocations are special types of edge dislocations that lie on {100} planes. Unlike the {111} family of planes, {100} planes are not close packed planes and the glide of dislocations on these planes is expected to be difficult. Additionally, dissociation of Lomer dislocations within {100} planes is not observed. These dislocations are expected to form as a result of a reaction of dislocations gliding on intersecting {111} planes [14]. While the Lomer dislocation represents a compact core, it can adopt a core configuration that is dissociated across the two intersecting {111} planes [15], also known as a Lomer-Cottrell dislocation. Depending on the shear stress applied on the dislocation, the core can also further reconfigure into many more complicated configurations (the details of which will be presented in Chapter 5). As these dislocations act as barriers to motion of other dislocations on {111} slip planes, the various adopted configurations of these dislocations is expected to impact work-hardening behavior in FCC metals and alloys. The reconfiguration of Lomer and Lomer-Cottrell dislocation cores as a function of applied stress and alloy composition is the subject of Chapter 5.

1.3 Dissertation Outline

The remainder of this dissertation is organized as follows. Chapter 2 focuses on summarizing simulation methodology that are used in Chapters 3-5. We start by presenting the embedded-atom method, the interatomic potential form that is used for all the presented studies, as well as the average-atom potential formalism, which approximates the behavior of random alloys. We then discuss the nudged-elastic band method, as well as the climbing-image extension, as a tool for calculating transition state energy barriers. A discussion on Monte Carlo methods follows next, summarizing the procedures and parameters required for various thermodynamic ensembles (canonical, semi-grand canonical, variance-constrained semi-grand canonical). We briefly discuss the use of molecular dynamics as it is used in Chapters 3-4. Finally, we also discuss the four commonly used boundary conditions that are employed for atomistic simulations of dislocations as well as their advantages and disadvantages.

In Chapter 3, we present a study on the first dislocation core reconfiguration process discussed in this dissertation: dislocation climb. We briefly review a theory for dislocation climb, which describes in to what degree dislocation climb is attachment-limited or diffusion-limited depending on temperature and vacancy supersaturation. Mesoscale models incorporating dislocation climb contributions to creep tend to assume a diffusion-limited regime for the sake of simplicity [16, 17, 18]. In this study we show that this regime is only valid for relatively high homologous temperatures and vacancy supersaturation when estimating a jog density along edge dislocations from atomistic simulations. The regime of validity is narrowed even further when considering a low stacking fault energy FCC metal.

In Chapter 4, we present a study on the next dislocation core reconfiguration process discussed in this dissertation: dislocation cross-slip. Specifically, we elucidate the effect of short-range ordering (SRO) on the cross-slip process in a FCC alloy. In mesoscale models, cross-slip is typically independent of local solute environment, or, in the rare case where it is not, is assumed to be affected by a random distribution of solutes [19]. In this study we use atomistic simulations to show how SRO can strongly modify cross-slip activation energy barriers, and how this modification can affect dynamic recovery rates, an important contribution to work-hardening.

In Chapter 5, we present a study on the final dislocation core reconfiguration process discussed in this dissertation: the reconfiguration of Lomer/Lomer-Cottrell dislocation cores under varying applied stresses and composition. Mesoscale models typically assume that these dislocations reconfigure only through an “unzipping” mechanism [20, 21, 22], and do not account for the effect of local alloy composition. In this study we use atomistic simulations and uncover a variety of Lomer/Lomer-Cottrell dislocation core configurations under different applied stresses and local compositions, including one that promotes twin nucleation, that are expected to affect work-hardening.

Chapter 6 summarizes the main results of this dissertation and provides direction for potential future work.

Chapter 2

Simulation Methods

2.1 Embedded-Atom Method

The key assumption in classical atomistic simulations is the form of the interatomic potential. Properties of atomic configurations are derived from the appropriate description of their energies. In this dissertation, the embedded-atom method (EAM) potential form is used to describe energies of various dislocation configurations. The EAM model is chosen as it reasonably describes salient features of metallic bonding while being computationally efficient to evaluate. In the EAM approach, the energy (E) of an atomic configuration is given by [23]:

$$E = \sum_i F_{s_i}\Big(\sum_{j\neq i} \rho_{s_j}(R_{ij})\Big) + \frac{1}{2}\sum_{i,j(j\neq i)} V_{s_i s_j}(R_{ij}). \tag{2.1}$$

The last term in Eq. 2.1 represents the pair interaction contribution between all pairs of atoms i and j, where s_i and s_j are their respective elemental species and $V_{s_i s_j}$ is the pair interaction energy as a function of the distance between atoms, R_{ij}. The key feature of the EAM model is the first term in Eq. 2.1, also known as the embedding term. The embedding term represents the energy of embedding an atom (F_{s_i}) as a function of the local electron density (ρ_{s_j}), which is assumed to be radially symmetric. This contribution to the energy of a system represents a many-body effect that causes the strength of atomic bonds to be dependent on other bonds, which is a necessary effect to account for at defects such as dislocations. The EAM model is well suited to study the dislocation behavior in the FCC systems investigated in this dissertation (the pure Al and Cu systems in Chapter 3 [24], the Ni-Al alloy system in Chapter 4 [25], and the Cu-Ni alloy system in Chapter 5 [26]).

Average-Atom Potentials

When obtaining the average properties of random alloys using atomistic simulations, it is typically necessary to average over many different configurations as local compositional fluctuations can cause local variations in properties such as, for example, stacking fault energies. An alternative approach to averaging over many different configurations is to use an average-atom potential [27]. In this approach, each atom in an alloy is replaced with a fictitious "average-atom" creating a homogeneous disordered state. Through an averaging procedure of Eq. 2.1 over all possible site occupations in a completely random alloy, the energy (E_A) of an average-atom system is [27]:

$$E_A = \sum_i F_A\Big(\sum_{j\neq i} \rho_A(R_{ij})\Big) + \frac{1}{2}\sum_{i,j(j\neq i)} V_{AA}(R_{ij}), \tag{2.2}$$

where ρ_A is the average electron density given by:

$$\rho_A(R_{ij}) = \sum_X c_X \rho_X(R_{ij}), \tag{2.3}$$

F_A is the average embedding function given by:

$$F_A\Big(\sum_{j\neq i} \rho_A(R_{ij})\Big) = \sum_X c_X F_X\Big(\sum_{j\neq i} \rho_A(R_{ij})\Big), \tag{2.4}$$

and V_{AA} is the average pair interaction energy given by:

$$V_{AA}(R_{ij}) = \sum_{X,Y} c_X c_Y V_{XY}(R_{ij}). \tag{2.5}$$

In Eqs. 2.3-2.5, the summations over X and Y represent summations over different species, and c_X and c_Y represent the concentrations of those species. The only assumption in the averaging procedure leading to the above equations is the truncation of a Taylor expansion of the embedding function after first order in ρ_A. It is worth noting that the above equations do not represent a simple averaging of the elemental potentials of the constituent species of the alloy, as evidenced by the inclusion of cross-interaction terms in Eq. 2.5.

When compared to configurational averaging of properties obtained from true random alloys, the average-atom approach results in good agreement with many properties, including lattice constants, cohesive energies, surface energies, solute energies, solute misfit volumes, elastic constants, and stacking fault energies [27]. Thus, the average-atom approach allows for a convenient starting point for initial dislocation configurations before introducing explicit solutes in the cross-slip study in Chapter 4. Additionally, it allows for an enormous simplification in the treatment of boundary conditions in Chapter 5. While convenient, the average-atom approach can not account for chemical heterogeneity such as ordering, clustering, or segregation at defects. However, these behaviors can be treated as perturbations to an average-atom state [28, 29].

2.2 Nudged-Elastic Band Method

Chapters 3 and 4 appeal to concepts in harmonic transition state theory [30], where thermally activated events are dictated by an activation energy barrier. This requires finding the minimum energy pathway (MEP) between the initial and final states of a thermally activated event. The nudged-elastic band (NEB) method provides an approach to obtain the MEP [31]. The NEB method requires the creation of N images, with the initial and final images representing the initial and final states, and intermediate images typically provided through a linear interpolation of the atomic coordinates of the initial and final states. For each image, i, there is a corresponding set of atomic coordinates, $\mathbf{R}_i$. The MEP is found by minimizing the forces, $\mathbf{F}_i$, on intermediate states, which are given by:

$$\mathbf{F}_i = \mathbf{F}_i^s|_{\parallel} - \nabla E(\mathbf{R}_i)|_{\perp}. \tag{2.6}$$

The first term in Eq. 2.6 is a spring force along a local tangent given by:

$$\mathbf{F}_i^s|_{\parallel} = k(|\mathbf{R}_{i+1} - \mathbf{R}_i| - |\mathbf{R}_i - \mathbf{R}_{i-1}|)\hat{\boldsymbol{\tau}}_i, \tag{2.7}$$

where k is a chosen spring constant and $\hat{\boldsymbol{\tau}}_i$ is the normalized local tangent at image i. The second term in Eq. 2.6 is a true force perpendicular to the local tangent given by:

$$\nabla E(\mathbf{R}_i)|_{\perp} = \nabla E(\mathbf{R}_i) - \nabla E(\mathbf{R}_i) \cdot \hat{\boldsymbol{\tau}}_i \hat{\boldsymbol{\tau}}_i. \tag{2.8}$$

The spring force in Eq. 2.7 keeps the images spaced apart from each other and the true force in Eq. 2.8 prevents the images from deviating from the MEP. In some cases, it may be desirable to add an additional spring force to Eq. 2.6 that acts perpendicular to the local tangent to prevent kinks from forming along the MEP [32].

Climbing-Image Nudged-Elastic Band Method

Extracting an energy barrier from the MEP requires knowledge of the difference between the energy at the saddle point and energy at the initial state. The NEB approach as described earlier does not provide the value of the energy at the saddle point. To obtain this value, the MEP obtained from the NEB method needs to be further refined using the climbing-image NEB (CI-NEB) method [33]. In this approach, the image with the highest energy, i_{max}, has a force applied to it that is different than Eq. 2.6:

$$\mathbf{F}_{i_{max}} = -\nabla E(\mathbf{R}_{i_{max}}) + 2\nabla E(\mathbf{R}_{i_{max}}) \cdot \hat{\boldsymbol{\tau}}_i \hat{\boldsymbol{\tau}}_i. \tag{2.9}$$

The second term in Eq. 2.9 is what allows image i_{max} to climb uphill in energy until it reaches the saddle point. Note that image i_{max} is not affected by a spring force parallel to the local tangent. Once the CI-NEB method has converged, the activation energy barrier is given by $E(\mathbf{R}_{i_{max}}) - E(\mathbf{R}_1)$.

2.3 Monte Carlo

In Chapter 4, SRO states are established using a hybrid molecular dynamics/Monte Carlo approach in the variance-constrained semi-grand canonical ensemble. This thermodynamic ensemble is chosen due to the ability to its ability to be implemented in a parallel manner. Discussing Monte Carlo in this ensemble first requires a short discussion of both the canonical and the semi-grand canonical ensembles. What follows is a summary of these ensembles as discussed in Ref. [34].

Canonical Ensemble

The canonical ensemble is representative of a system that maintains a constant number of species, volume, and temperature. In this ensemble, the probability of a state with a set of atomic coordinates, $\mathbf{R}$, and a set of species that occupy those coordinates, $\mathbf{s}$, is:

$$P_C(\mathbf{R},\mathbf{s}) = Z_C^{-1}\mathrm{exp}\Big(-\beta E(\mathbf{R},\mathbf{s})\Big), \tag{2.10}$$

where Z_C is the partition function which normalizes the probability, and β is equal to $(k_BT)^{-1}$, where k_B is the Boltzmann constant and T is the absolute temperature. In order to sample occupational degrees of freedom consistent with the above probability distribution, two atoms with unlike species are randomly chosen, and a trial move is proposed which swaps the positions of those atoms. This trial move is accepted with a probability of:

$$P_C^{acc} = \min\{1, \mathrm{exp}\Big(-\beta[E(\mathbf{R},\mathbf{s}_t) - E(\mathbf{R},\mathbf{s}_i)]\Big)\}, \tag{2.11}$$

where t represents the trial state and i represents the initial state. The sequential acceptance/rejection of many trial moves is what constitutes a Monte Carlo (MC) simulation. Equilibrium is reached once $E(\mathbf{R},\mathbf{s})$ stops decreasing as a function of number of trial moves and instead fluctuates around an average value. States that are sampled at this stage represent the most probable states and their most probable fluctuations according to Eq. 2.10. While MC simulations in this ensemble are desirable when fixing the concentration of an alloy, the canonical ensemble is not well suited for taking advantage of parallel hardware, making it difficult to implement for large systems.

Semi-Grand Canonical Ensemble

The semi-grand canonical (SGC) ensemble is representative of a system that maintains a constant number of atoms, difference in chemical potentials between species, volume, and temperature. For a binary alloy in this ensemble, the probability of a state is:

$$P_{SGC}(\mathbf{R},\mathbf{s}) = Z_{SGC}^{-1}\mathrm{exp}\Big(-\beta[E(\mathbf{R},\mathbf{s}) + \Delta\mu N\hat{c}(\mathbf{s})]\Big), \tag{2.12}$$

where Z_{SGC} is the appropriate partition function, $\Delta\mu$ is the chemical potential difference between the two species, N is the total number of atoms, and $\hat{c}(\mathbf{s})$ is the concentration of the second species in a state with $\mathbf{s}$. In order to sample occupational degrees of freedom consistent with the above probability distribution, an atom is chosen at random, and a trial move is proposed which transmutes the species of that atom. This trial move is accepted with a probability of:

$$P^{acc}_{SGC} = \min\{1, \exp\Big(-\beta[E(\mathbf{R}, \mathbf{s}_t) - E(\mathbf{R}, \mathbf{s}_i) + \Delta\mu N\big(\hat{c}(\mathbf{s}_t) - \hat{c}(\mathbf{s}_i)\big)]\Big)\}. \tag{2.13}$$

Equilibrium is reached once $E(\mathbf{R}, \mathbf{s}) + \Delta\mu N\hat{c}(\mathbf{s})$ stops decreasing as a function of number of trial moves and instead fluctuates around an average value. States that are sampled at this stage represent the most probable states and their most probable fluctuations according to Eq. 2.12. Due to the nature of the trial moves in this ensemble, SGC-MC simulations can take advantage of parallel hardware. However, the fluctuations in composition in this ensemble may be undesirable depending on the application.

Variance-Constrained Semi-Grand Canonical Ensemble

The variance-constrained semi-grand canonical (VC-SGC) ensemble is an extension of the SGC ensemble that reduces compositional fluctuations. For a binary alloy in this ensemble, the probability of a state is:

$$P_{VC-SGC}(\mathbf{R}, \mathbf{s}) = Z^{-1}_{VC-SGC}\exp\Big(-\beta[E(\mathbf{R}, \mathbf{s}) + N\hat{c}(\mathbf{s})\big(\phi + \kappa N\hat{c}(\mathbf{s})\big)]\Big), \tag{2.14}$$

where Z_{VC-SGC} is the appropriate partition function, and ϕ and κ are parameters that affect the ensemble average and variance in composition, respectively. When κ is set to zero, the VC-SGC ensemble becomes the SGC ensemble as ϕ becomes equivalent to $\Delta\mu$. As κ goes to infinity and ϕ is set to $-2\kappa N\hat{c}(\mathbf{s})$, the canonical ensemble is recovered. In order to sample occupational degrees of freedom consistent with the above probability distribution, an atom is chosen at random, and a trial move is proposed which transmutes the species of that atom. This trial move is accepted with a probability of:

$$P^{acc}_{VC-SGC} = \min\{1, \exp\Big(-\beta\big[E(\mathbf{R}, \mathbf{s}_t) - E(\mathbf{R}, \mathbf{s}_i) + N\big(\hat{c}(\mathbf{s}_t) - \hat{c}(\mathbf{s}_i)\big)\big(\phi + \kappa N[\hat{c}(\mathbf{s}_t) + \hat{c}(\mathbf{s}_i)]\big)\big]\Big)\}. \tag{2.15}$$

Equilibrium is reached once $E(\mathbf{R}, \mathbf{s}) + N\hat{c}(\mathbf{s})\big(\phi + \kappa N\hat{c}(\mathbf{s})\big)$ stops decreasing as a function of number of trial moves and instead fluctuates around an average value. States that are sampled at this stage represent the most probable states and their most probable fluctuations according to Eq. 2.14. Similar to SGC-MC, VC-SGC-MC simulations can take advantage of parallel hardware due to the nature of the trial moves [34]. The VC-SGC ensemble provides an advantage over the SGC ensemble as it can limit the compositional fluctuations during MC simulations. As large cells on the order of hundreds of thousands of atoms are used in Chapter 4, MC in the VC-SGC ensemble is used to efficiently equilibrate an SRO state while maintaining a nearly fixed composition.

2.4 Molecular Dynamics

In Chapters 3 and 4, molecular dynamics (MD) simulations are used to sample low-energy states through simulated annealing as well as to sample displacive degrees of freedom in a hybrid MD/MC approach. MD simulations propagate the positions of atoms forward in time through the knowledge of the atoms' velocity and acceleration, which is crucially dependent on the negative gradient of the potential energy of the atom as described by a given interatomic potential. The equations of motion are modified when requiring a constant temperature and/or pressure [35]. The MD simulations in this dissertation are solely for the initial set up of zero temperature energy minimization or CI-NEB calculations, which provide the main results in later chapters. For the interested reader, further details of MD simulations can be found in Refs. [35, 36].

2.5 Boundary Conditions for the Atomistic Simulation of Dislocations

Fully Periodic Boundary Conditions

Simulations in Chapter 3 use fully periodic boundary conditions. In this case, illustrated in Figure 2.1(a), the simulation cell interacts with infinitely many replicas tessellated with each other at the boundaries. It is necessary to have a dislocation dipole in the simulation cell as the net Burgers vector in the cell must be zero in order for the system to be fully periodic. The simulation cells must also be initialized with displacement fields that account for the presence of dislocations in the periodic replicas, as well as a homogeneous strain to account for the plastic strain generated by the dislocation dipole [37, 38, 1]. The advantage of this approach is that there is no need to account for spurious effects at surfaces or fixed boundaries, and it allows for well-defined dislocation core energies for compact dislocation cores [39]. For extended dislocation cores, such as those found in FCC metals and alloys, this approach may artificially limit the dissociation distance of the dislocations, and convergence studies of the dissociation width as a function of cell size are needed.

Fixed Boundary Conditions

Simulations in Chapter 4 use fixed boundary conditions. In this case, illustrated in Figure 2.1(b), the simulation cell is partitioned into an inner atomistic region, which contains the dislocation core, and an outer continuum region, which contains long range displacements associated with the dislocation as predicted by linear elasticity theory. The advantage of this approach is in its simplicity, as there is no need to account for periodic dislocation-dislocation interactions. Dislocation core energies can be obtained from this approach, although it requires the measurement of energy of the dislocation for many different simulation cell sizes [40]. If the inner region is too small, spurious forces can build up at the boundary between

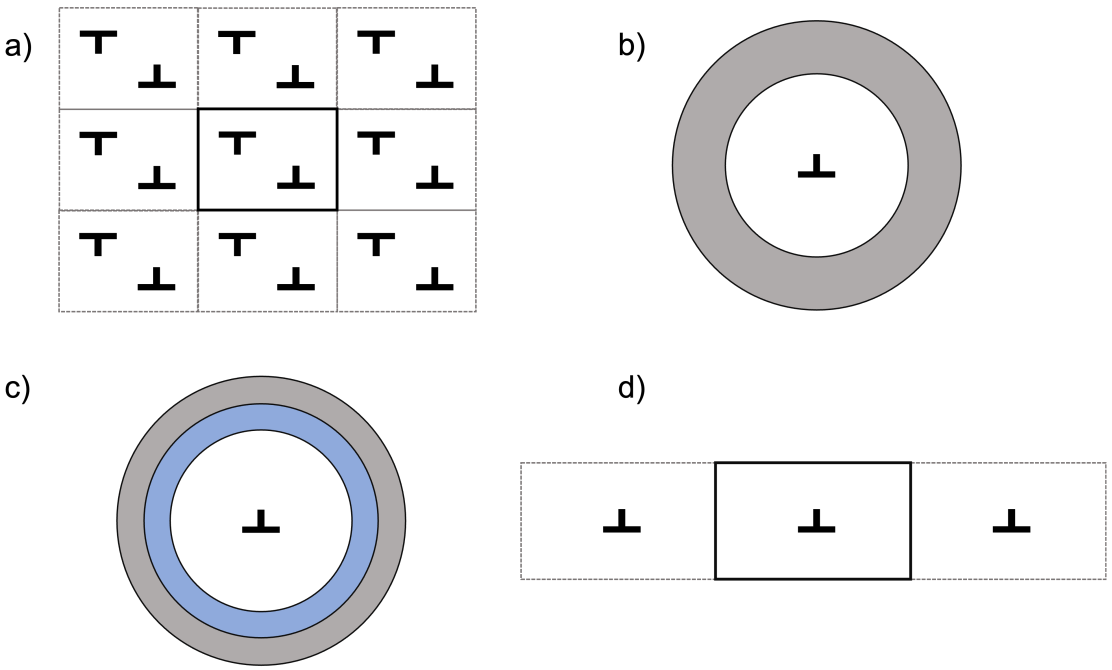

Figure 2.1: a) Fully periodic boundary conditions where the simulation cell is in the middle with solid lines. Only nearby periodic replicas are shown but the simulation cell is interacting with infinitely many replicas. b) Fixed boundary conditions where the inner atomistic region (white) contains the dislocation core is surrounded by an outer continuum region (grey). c) Flexible boundary conditions where a buffer region (blue) separates an inner atomistic region and an outer continuum region. d) Free-surface boundary conditions where only the nearest replicas of the middle simulation cell are shown. The cell interacts with infinitely many replicas along the glide direction. In all of the above cases, the systems are periodic in and out of the page.

the two regions during the atomistic relaxation of the inner region. This can affect the dislocation core structure and convergence studies of the dislocation structure as a function of size are needed. Additionally, due to the fixed displacement fields in the outer region, the system will artificially resist dislocation motion under an applied stress [41].

Flexible Boundary Conditions

Simulations in Chapter 5 use flexible boundary conditions. In this case, illustrated in Figure 2.1(c), the simulation cell is partitioned into an inner atomistic region, an outer continuum region, and an intermediate buffer region. After the relaxation of atomic positions in the inner region, the spurious forces in the buffer region are minimized through the use of Green's functions, which map those forces to atomic displacements in the simulation cell [42]. This allows for the simulation cell to have a displacement field that is flexible with respect to the dislocation position and configuration, in contrast to the fixed boundary condition approach. Converged core structures can be obtained with smaller cells compared to those needed using fixed boundary conditions. The main disadvantage of flexible boundary conditions is the added complexity of the simulation procedure involving Green's functions to reduce the spurious forces in the buffer region.

Free-Surface Boundary Conditions

While none of the studies presented in this dissertation use a free-surface boundary condition, it is worth briefly discussing for the sake of completeness. In this case, illustrated in Figure 2.1(d), a simulation cell with a single dislocation is periodic in the glide direction but not in the direction normal to the glide plane. The dislocation must be placed in the middle of the two surfaces to avoid surface image effects. This is the preferred approach for dislocation mobility simulations [43, 44, 45], as glide can occur in and out of the simulation cell without the influence of nearby dislocations with oppositely signed Burgers vectors that can periodically accelerate/decelerate glide. However, one should keep in mind that as this essentially results in an infinite array of dislocation with the same Burgers vector, there is a driving force for the simulation cell to bend or twist, depending on the dislocation character.

Chapter 3

Insights into Dislocation Climb Efficiency in FCC Metals from Atomistic Simulations[1]

3.1 Introduction

In the plastic deformation of crystals, climb is a process that enables dislocations to overcome obstacles in a slip plane through the absorption or emission of vacancies. Driving forces for climb arise due to supersaturation of point defects and elastic stress, providing a mechanism to evolve the system towards equilibrium. Dislocation climb under both types of driving forces is influenced by the rate of arrival of vacancies, and when their flux is the rate-limiting factor, analytical theories can be developed for steady-state climb velocities. However, it has long been appreciated [12, 47, 48] that limited availability of jogs along a dislocation line can lead to a reduction in climb velocity relative to this diffusion-limited value. As reviewed in the next section, the notion of a climb *efficiency*, defined as the ratio of the actual climb velocity to the ideal diffusion-limited value [12], has been introduced to quantify such deviations.

Climb rates in different FCC metals with quenched-in vacancy loops have been determined by transmission electron microscopy through the measurement of the shrinkage kinetics under annealing conditions, which are related to the vacancy emission rate [49, 50]. These experiments have shown that in FCC metals, there is a trend for lower stacking fault energy (SFE) metals to have lower climb efficiencies. Other less direct experiments, which estimate the driving forces for climb based on quenching conditions and mechanical stresses, lead to similar conclusions [51]. While there is consensus on this qualitative trend related to

---

[1] The results presented in this chapter and the corresponding Supplementary Material document have been published as a regular article titled "*Insights into Dislocation Climb Efficiency in FCC Metals from Atomistic Simulations*" in Acta Materialia, **193**, pp. 172-181, (2020), doi: 10.1016/j.actamat.2020.04.047 by Anas Abu-Odeh, Maeva Cottura, and Mark Asta [46]. The material is presented here with the permission of co-authors and publishers.

the decrease in climb efficiency with decreasing stacking fault energy, quantitative relations between driving force and climb efficiency that can be compared to available theoretical models (see below) are challenging to derive directly from currently available experimental data. This is due to the presence of combined contributions to the driving force arising from curvature, external stress, and vacancy supersaturation, and the possible role of a combination of different diffusion mechanisms. For example, detailed measurements and analyses of vacancy loop growth in FCC Al [52, 51] led to estimates for climb efficiency assuming growth due to the absorption of vacancies emitted by smaller loops. However later studies proposed a mechanism where a vacancy loop could migrate through “self-climb” as a consequence of short-circuit diffusion in the dislocation core [53, 54] and the effect of this mechanism on the climb efficiency estimates has not been undertaken. Climb efficiencies were also estimated based on experiments for FCC Au displaying dislocation networks [55]; these microstructures displayed stacking fault tetrahedra (SFT), which can have diffusivities that are orders of magnitude faster than mono-vacancies [56] and the effect of this transport mechanism on the estimated efficiencies remains unclear. In light of the these types of complicating factors characteristic of realistic microstructures, mesoscale and atomistic simulation methods are of interest as they provide a complementary framework to derive fundamental relations between driving forces and climb rates.

Mesoscale methods such as discrete dislocation dynamics (DDD) and phase field models (PFM) offer an attractive framework to model dislocation climb processes. However, for such applications, models and associated assumptions have to include the relative contributions of vacancy diffusion and “attachment” processes associated with the concentration of jogs and vacancy attachment to them. A number of DDD models assume diffusion-limited climb rates, where barriers for attachment of vacancies to the dislocation are considered unimportant [16, 17, 18], which is suitable for metals with high climb efficiencies. By contrast, the model introduced by Gao *et al.* assumes attachment-limited kinetics suitable for a low-jog density along the dislocation line [57]. Additional DDD models have introduced parameters to describe the effects of non-ideal climb efficiencies [58, 59] whose values must be derived from microscopic theories. PFM implementations provide an alternative framework for modeling dislocation climb processes. The PFM models introduced by Ke *et al.* [60] and that of Geslin *et al.* [61, 62] allow for mixed attachment and diffusion-limited behavior through the introduction of an attachment kinetics parameter that must be fit to experiments or atomistic simulations. Liu *et al.* illustrated the importance of accurately describing the mixed kinetics of climb in a PFM of low-angle grain boundaries where, depending on the kinetics of vacancy attachment, the variation of grain boundary sink strength can influence void nucleation under vacancy supersaturation [63]. Gu *et al.* also demonstrated that a deviation from a dislocation being a perfect sink/source of vacancies can change the self-healing time of perturbed low-angle grain boundaries [64].

To enhance predictive capabilities in the modeling of dislocation climb, information about vacancy and jog properties can be derived from calculations at the atomic scale. Relevant atomistic computational work can be summarized as follows. Density-functional theory (DFT) calculations on the effect of solutes on the SFE in Ni and vacancy diffusion effects on climb were carried out by Yu and Wang [65], assuming that the energy of the jog is governed by the cost of constricting the two Shockley partials, which is believed to provide an upper bound [48]. Sarkar *et al.* used diffusive molecular dynamics (MD) to study the evolution of a jog-pair in FCC Cu [66], and a displacive-diffusive path associated with climb was identified. In further atomistic studies, Baker and Curtin employed a mixture of accelerated MD simulations and solutions to a discrete diffusion equation to investigate jog-pair formation in FCC Al [67]. Lau *et al.* investigated the jog structure and vacancy attachment energies for a mixed dislocation in BCC Fe using the nudged elastic band (NEB) method [68]. Using the energies from this study, Kabir *et al.* parameterized a kinetic Monte Carlo (kMC) model to simulate climb velocity under a high supersaturation of vacancies and to extrapolate creep behavior [69]. It was shown that an analytical equation of climb matched these results, although the high dislocation densities in these simulations complicate extrapolation to conditions more typical of creep experiments [70]. Swinburne *et al.* parameterized a kMC model to study the significant effects of self-climb versus vacancy mediated climb on interstitial loops in Fe and W, and the effects are postulated to be of the same magnitude for FCC materials [54]. These studies demonstrate the insights into climb behavior that can be derived from atomistic simulations, and the use of quantities calculated at this scale in mesoscale models.

To build on the modeling work summarized above, this study employs atomistic simulations to investigate the energetics underlying jog formation and vacancy attachment for representative high and low stacking fault FCC metals, Al and Cu, respectively. The energetics obtained from these simulations are used to understand consequences for climb efficiencies within the kinetic theory of climb developed by Balluffi [12]. In addition, energetic barriers associated with constriction of vacancy aggregates into jog-pairs and vacancy diffusion towards extended jogs are explored using the NEB method [31, 33]. To motivate the atomistic calculations undertaken in this work, Section §3.2 presents a summary of the dislocation climb theory due to Balluffi [12]. Section §3 describes the simulation setup and computational details. Results for jog-pair formation energetics and the change in vacancy migration barriers near a jog are presented in Section §4, and Section §5 applies Balluffi's climb theory to quantify climb efficiencies in Al compared to Cu. Section §6 provides a summary of the main conclusions from this work.

3.2 Dislocation Climb Theory

In this section we review the theoretical model for dislocation climb due to Balluffi [12], which motivates the atomistic calculations described in the next section. The model considers dislocation climb under vacancy supersaturation driving forces, and involves six main assumptions:

1. the dislocation is straight, unconstrained, and is in a low index direction
2. jogs nucleate homogeneously by vacancy aggregation along the core

3. vacancies reaching the core diffuse rapidly to the jogs
4. the dislocation is undissociated
5. vacancy quasi-equilibrium is maintained at the jogs
6. the energy of embryonic jog pairs increases monotonically with size

The model considers the diffusion of vacancies to jogs, which are treated as ellipsoidal sinks situated at an equilibrium spacing along the dislocation line (Figure 3.1). The solution to the diffusion equation provides a steady-state velocity (v_{mixed}) in the so-called "mixed" kinetic regime given by:

$$v_{mixed} = 2\pi D b^2 \frac{2Z}{\lambda} \frac{\left[\, c(R) - c^0 \,\right]}{\left[\, \ln\left(\frac{2Z}{\lambda}\frac{\lambda}{b}\right) + \frac{2Z}{\lambda} \ln\left(\frac{R}{\lambda}\right) \,\right]} \tag{3.1}$$

where $c(R)$ is the supersaturated concentration of vacancies in the bulk material at a distance R far from the jog. c^0 is the vacancy concentration in equilibrium with the jogs, taken to be the equilibrium bulk vacancy concentration consistent with the assumption of local thermodynamic equilibrium. D represents the bulk vacancy diffusivity and b is the Burgers vector. The mean-free path of a vacancy in the dislocation core (Z) is given by:

$$Z = \sqrt{2} b \exp\left(\frac{\Delta W_{sm}}{2kT}\right) \tag{3.2}$$

where $\Delta W_{sm} = E_b - E_c$ is the difference between the self-migration energy, defined as the sum of the formation energy and the migration energy, of a vacancy in the bulk (E_b) and the core (E_c). k is the Boltzmann constant and T is the absolute temperature. The equilibrium distance between jogs (λ) along the dislocation is given by the expression:

$$\lambda = b \exp\left(\frac{\Delta F^*_{jogpair}}{2kT}\right) \tag{3.3}$$

where $\Delta F^*_{jogpair}$ is the free energy change associated with jog-pair formation. This free energy change is multiplied by 1/2 because it is assumed that each jog contributes equally to the jog-pair formation energy. In this model, the thermodynamic driving force for dislocation climb is given by the difference in vacancy chemical potential ($\Delta\mu$) at the jogs versus in the far field. In the dilute limit, this value is given by:

$$\Delta\mu = kT \ln\left(\frac{c(R)}{c^0}\right) \tag{3.4}$$

In applying this theory, R is taken as half the value of the average dislocation spacing:

$$R = \frac{1}{2}\rho^{-\frac{1}{2}} \tag{3.5}$$

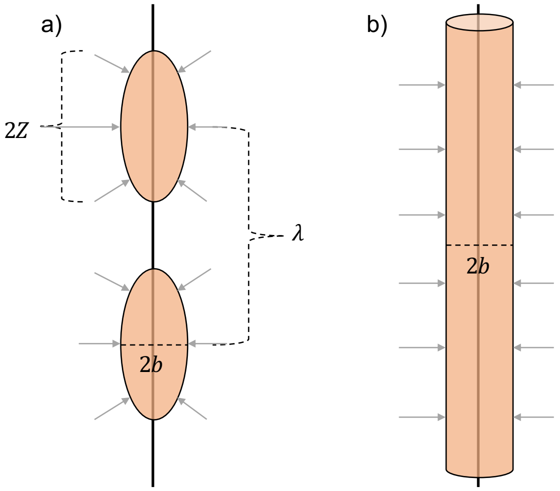

Figure 3.1: Representation of vacancy sinks when a) $\frac{2Z}{\lambda} < 1$ and when b) $\frac{2Z}{\lambda} \geq 1$. Vacancies fluxes are schematically represented by the gray arrows.

where ρ is the dislocation density.

The critical condition of $\frac{2Z}{\lambda} = 1$ represents the overlapping of the ellipsoidal sinks (see Fig. 1), and in this limit Eq. 3.1 becomes:

$$v_{diff-control} = 2\pi D b^2 \frac{[c(R) - c^0]}{\ln{(R/b)}}, \tag{3.6}$$

which represents the diffusion controlled limit of the climb velocity. The actual climb velocity (v_{actual}) depends on the ratio of Z to λ, and is given by:

$$v_{actual} = \begin{cases} v_{mixed}, & \text{if } \frac{2Z}{\lambda} < 1. \\ v_{diff-control}, & \text{otherwise.} \end{cases} \tag{3.7}$$

The climb efficiency, η, is then defined as:

$$\eta = \frac{v_{actual}}{v_{diff-control}} \tag{3.8}$$

and provides a measure of the reduction in climb velocity relative to the idealized diffusion-limited case.

The limiting case of $\eta = 1$ corresponds to ideal diffusion-limited climb velocities, while values of $\eta < 1$ indicate the importance of attachment processes at the jogs in limiting the climb velocity. Mesoscale models of climb that incorporate mixed kinetics are dependent on ratios similar to Z/λ [58, 59] or are dependent on λ [62]. These values are difficult to derive directly from experimental measurements, and an alternative is to determine them from simulations at the atomic scale. The next section discusses the applications of atomistic simulations for FCC metals in this context.

Material	C_{11} (GPa)	C_{12} (GPa)	C_{44} (GPa)	a_{lat} (Å)
Al	110	61	33	4.045
Cu	175	128	84	3.639

Table 3.1: Elastic constants and lattice constants for the EAM potentials of Al and Cu [24] used in the atomistic simulations.

3.3 Simulation Details

The system used for the simulations of Al and Cu consists of two [110](111)-type edge dislocations arranged in a periodic quadrupole configuration [39]. For both systems, the x, y, z directions of the simulation cells are parallel to the $[1\bar{1}0]$, [111] and $[\bar{1}\bar{1}2]$ directions, respectively. The dislocations were introduced in the FCC lattice using the BABEL package [71, 72], which employs the Stroh formalism of anisotropic linear elasticity theory [73, 74] to solve for the strain fields around the dislocations using periodic boundary conditions following Cai *et al.* [37]. Material parameters required for initializing the cell include the crystal structure, elastic constants, and lattice constant, which are taken from the embedded-atom-method (EAM) potentials for Al and Cu employed in the simulations [24] (Table 3.1). The atomic positions were relaxed using the FIRE minimization scheme [75] implemented in the open-source LAMMPS [76] software to allow each edge dislocation to dissociate into two partials separated by a stacking fault. Then, the shape of the triclinic cells was relaxed using the conjugate gradient minimization scheme in order to relieve any residual shear stress from the periodic boundary conditions. Finally, the atomic positions were relaxed again using the FIRE minimization algorithm with a force convergence of 0.001 eV/Å.

The final dimensions of the Al and Cu relaxed cells are represented in Fig. 3.2, containing 573,120 and 1,146,240 atoms, respectively. The Al and Cu cells have the same x- and y-length relative to their lattice constants. The Cu cell is twice as long in the z-direction (i.e. the dislocation line direction) than for Al in anticipation of the stronger jog-jog interaction energy with periodic images due to the need for core constrictions (see Section §3.4 below). Particular attention must also be taken when choosing the size of the area of the z-face (i.e. the plane normal to the dislocation line direction), as it will determine how close neighboring dislocations are, which can affect the jog-pair formation energy, especially for Cu. The given cell size for Al is found to be large enough to avoid significant finite size effects. From convergence tests examining the dependence of the calculated jog-pair formation energy on system size, coupled with a model for this dependence based on an observed correlation with the dissociation distance between partial dislocations, it is estimated that with the z-face areas used in the simulation results for jog-pair formation energies in Cu are converged with respect to system size to within approximately 14%. Details of this analysis are given in the Supplementary Material document for this chapter.

Using the simulation cells described above, the energy of embryonic jog pairs were inves-

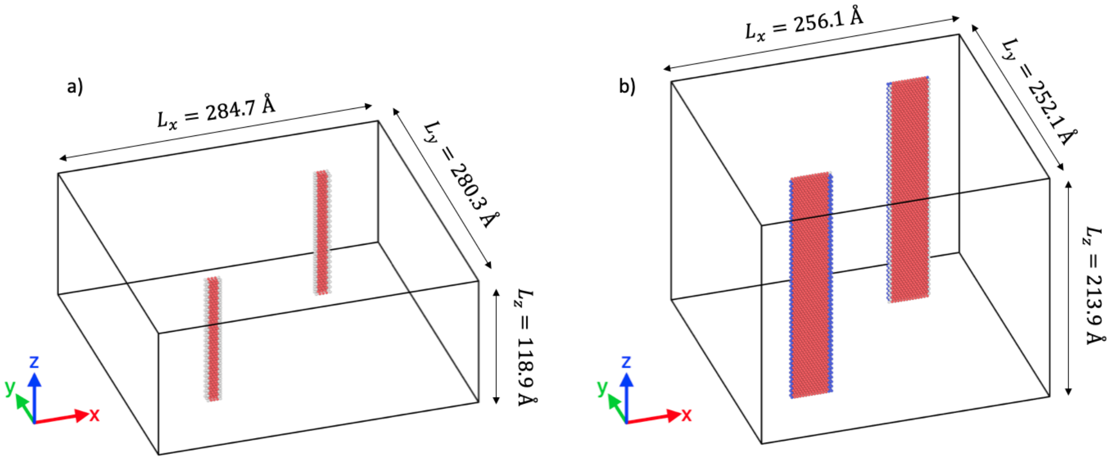

Figure 3.2: Simulation box containing two edge dislocations after relaxation for a) Al and b) Cu. Atoms in FCC environments were deleted according to the common neighbor analysis performed with OVITO [77, 78]. Red atoms represent the stacking fault region, and the remaining atoms represent the partial dislocations.

tigated using two alternative algorithms as presented in Section §3.4. In the first, which we will refer to as "non-annealed", an atom with the highest potential energy in the compressive region of the dislocation near one of the two partials of an otherwise perfect dissociated dislocation is deleted to form a vacancy. The procedure is similar to the one applied by Dos Reis *et al.* [79] for advancing a constricted jog on a dislocation with a nanovoid. After introducing the vacancy, the simulation cell was relaxed using FIRE minimization with a force convergence of 0.001 eV/Å. The atomic sites on the rows above and below (with respect to the z-axis of the simulation cell) the original vacancy on the dislocation core are searched to find the next minimum energy vacancy site and the corresponding atom is deleted, followed by a FIRE relaxation with a convergence of 0.001 eV/Å. The process is repeated, searching atomic rows directly above and below the vacancy aggregation until the desired number of vacancies have been absorbed by the dislocation. The resulting energy, $E_{jogpair}$, of the defect introduced by the vacancies is given by:

$$E_{jogpair} = E_1 - N_1 * E_{coh} - (E_2 - N_2 * E_{coh}) \tag{3.9}$$

where E_1 is the total energy of the cell with the dislocations and the added vacancies, N_1 is the number of atoms in that cell, E_2 is the total energy of the cell with just the dislocations, N_2 is the number of atoms in that cell, and E_{coh} is the cohesive energy per atom, which for FCC Al is -3.4107 eV/atom, and for FCC Cu is -3.2831 eV/atom, with the interatomic potential models employed in these calculations. The quantity $E_{jogpair}$ defined in Eq. (3.9) allows for the calculation of the critical free energy change needed in Eq. (3.3), which is derived as the maximum of the quantity:

$$\Delta F_{jogpair}(N_{vacs}) = E_{jogpair}(N_{vacs}) - N_{vacs} * \Delta\mu \tag{3.10}$$

where N_{vacs} is the number of vacancies absorbed by the dislocation, and $\Delta\mu$ is the chemical potential driving force defined in Eq. (3.4).

The process outlined in the previous paragraph leads to the formation of jog pairs, but does not guarantee that the minimum-energy path is followed. Hence, a second process was used to relax the system once a given number of vacancies had been introduced to form the non-annealed structures. This process involves a simulated-annealing type of simulation, whereby the temperature of the system is raised to a relatively high homologous temperature (600 K for Al, 900 K for Cu) and subsequently quenched. This allows a quick exploration of lower energy basins that may not be accessible to the previous process by giving the atoms enough thermal energy to overcome energetic barriers. Specifically, finite-temperature molecular-dynamics simulations were performed in an NVT ensemble with a Langevin thermostat and a timestep of 0.003 ps. After 1000 timestep runs were performed to bring the system to thermal equilibrium, the simulation was run for another 1000-50000 timesteps for 5 iterations, with the structure of the cell output after each iteration. The final snapshots after each of these iterations were quenched using the FIRE minimization scheme to a force convergence of 0.01 eV/Å. The lower timestep range was used as a screening stage to find the smallest number of vacancies absorbed that would yield a lower energy structure than that obtained from the energy-minimization process of the previous paragraph. Then, the annealing procedure was applied to successively smaller amounts of vacancies, with an increased number of timesteps, until vacancy aggregates that were higher in energy than the next largest aggregate were relaxed to a lower energy state. From the final structure in the simulated annealing process (which was minimized again to a force convergence of 0.001 eV/Å), the minimization search described in the previous paragraph was repeated to investigate the evolution of the defect structure and associated energetics. This last step is to see if the energy of the jog pair structure at a sufficiently large number of absorbed vacancies matches that from the energetic path determined by the non-annealed search.

The annealed structures obtained from the simulated-annealing procedure outlined above were lower in energy relative to the non-annealed structures obtained from the vacancy-absorption and energy minimization process. The energy difference between annealed and non-annealed structure was most pronounced for Cu, as discussed in Section §3.4. The energy barrier associated with the transformation from the non-annealed to annealed structure for Cu was investigated using the NEB [31, 33] method. Such NEB calculations were performed for four annealed and non-annealed jog structures at various values of absorbed vacancies. Due to a sharp transition point in the minimum energy path, 48 images were used between the initial (non-annealed) and final (annealed) state. Afterwards, two more iterations of NEB each with 48 images were carried out, with the initial and final state taken as fixed images within the minimum-energy pathway derived from the previous iteration, in order to increase the density of images near the saddle point. Energy versus reaction coordinate plots and convergence of energy barriers with NEB iterations are given in the Supplementary Material document for this chapter. These calculations were performed with a convergence criteria of 0.01 eV/Å.

The NEB method was also employed for the calculated results presented in §3.4 to investigate vacancy migration barriers near a jog. In these simulations, a jog-pair structure was created on a dislocation with a jog spacing of half of the simulation cell height. This was done by deleting atoms on the extra half plane associated with the edge dislocation before relaxing the dislocations as outlined above. For extended and constricted jogs in both Al and Cu, a series of climbing image NEB [31, 33] calculations were performed of a vacancy following a tensile, compressive, or side path to the jog based on a chain of 5 closed-packed jumps in the desired direction as illustrated in Fig. 3.6. The force convergence used for the tensile and compressive paths was 0.01 eV/Å with 5 images used for each jump. The side paths were relaxed to a convergence of 0.03 eV/Å. This was done to avoid convergence issues due to the dislocation bowing out due to its attraction to the vacancy. This gives an upper bound of the jump barriers because as the dislocation bows towards the vacancy, some of the barriers in the path will decrease or disappear.

3.4 Simulation Results

In this section, we describe the results of the atomistic simulations in the context of the theoretical model reviewed in Section §3.2. Beforehand, we review the underlying assumptions of this model. First, the simulation geometries are designed to consider straight edge dislocations in an otherwise perfect crystal, such that they correspond to the assumptions 1 and 2 of the theoretical model. They are also designed to be consistent with assumption 3, which follows the idea that dislocation core diffusion is generally vacancy mediated. While molecular dynamics studies of vacancy and interstitial diffusivities in edge dislocations in Al [80] and Cu [81] show that this is valid in Al, for Cu both the interstitial and vacancy mechanism have been found to contribute equally. However, since our intent in this study, consistent with the theoretical model, is to study climb under vacancy supersaturation conditions, assumption 3 is viewed to be reasonable. Assumption 4, which states that the dislocations are not dissociated, is generally not true for FCC materials. However, this should not present a problem for the analysis below since the effects of dissociation are inherently included in the calculations of jog-pair formation energy. Assumption 5 is satisfied if it can be shown that the barrier for each jump of a vacancy from the bulk to the jog is never larger than the bulk migration barrier, and that the barriers to the jog are appreciably smaller than the reverse path [48]. Assumption 5 would break down if a high-energy barrier prevents the vacancy from easily being absorbed by an extended jog, e.g., it would require the partial dislocations to constrict first. We will investigate this issue using results of NEB calculations in Section §3.4, and show that the assumption holds for the present cases studied. Finally, assumption 6 is valid if there is no high-energy vacancy complex that forms before the nucleation of a jog-pair. This is explored by using a mix of molecular statics and simulated thermal annealing in §3.4.

We note that the Balluffi model neglects explicit incorporation of the interactions of the stress field of a dislocation with vacancies. These interactions will change the equilibrium vacancy concentrations near the dislocation as well as the mobilities underlying vacancy diffusion. PFM results [60, 62] for dislocation climb that have considered such elastic interaction effects suggest that they have a relatively small effect on the resulting climb velocity, especially when no applied stress is present. Thus, in the application of the Balluffi model to investigate climb efficiency these effects will not be considered further in what follows.

Structure and Energetics of Jogs

Figure 3.3 plots formation energies of dislocations with jogs and vacancy clusters as a function of the number of absorbed vacancies, with insets illustrating several representative structures. Results are presented for both non-annealed (green for Cu and blue for Al) and annealed (red for Cu and orange for Al) structures. The annealing search results in lower jog-pair formation energies, particularly for Cu, as the thermal fluctuations are able to overcome the barrier associated with constricting the vacancy clusters across the partials. Considering first the results for Cu, it is seen from the inset that the absorption of up to ten vacancies leads to the formation of an extended vacancy cluster centered on one of the two partial dislocations in the non-annealed samples. In these non-annealed samples the formation energy and area of these vacancy clusters increases monotonically until 32 vacancies are absorbed, at which point the vacancy-cluster structure collapses to form a jog-pair structure illustrated by the bottom right inset. This latter structure is consistent with the idea of a “well-formed” jog-pair structure in the theoretical model of Balluffi [12]. This jog-pair structure features one compact constricted jog (top) and one extended jog (bottom), with bowing of the partial dislocation line segments in between. Further addition of vacancies causes the jog pairs to separate but with the structure of the individual jogs remaining qualitatively similar. The annealed samples for Cu give the same structure as the non-annealed samples for up to ten absorbed vacancies. Beyond that, annealing leads to the formation of the constricted/extended jog-pair structure described above. In the annealed samples there is a slight increase in formation energy beyond approximately 11 absorbed vacancies, due to the decreasing effects of the jog-jog interaction as the jogs spread further apart. The distance between the jog-pairs is never larger than half of the supercell height in the simulations, to minimize the jog interactions with their periodic images.The jog-pair formation energies level out to a value of approximately 6.5 eV beyond approximately 35 absorbed vacancies. We note that the dissociated vacancy cluster structure found here for the non-annealed samples is similar in nature to that obtained by Sarkar et al. [66], who also identified an energetically downhill path between this cluster structure and the jog-pair structure in Cu.

For Al, the results of the structures as a function of absorbed vacancies are qualitatively similar to those for Cu, with the main differences being associated with the much narrower width of the dissociated dislocation core. Specifically, the extended vacancy cluster type

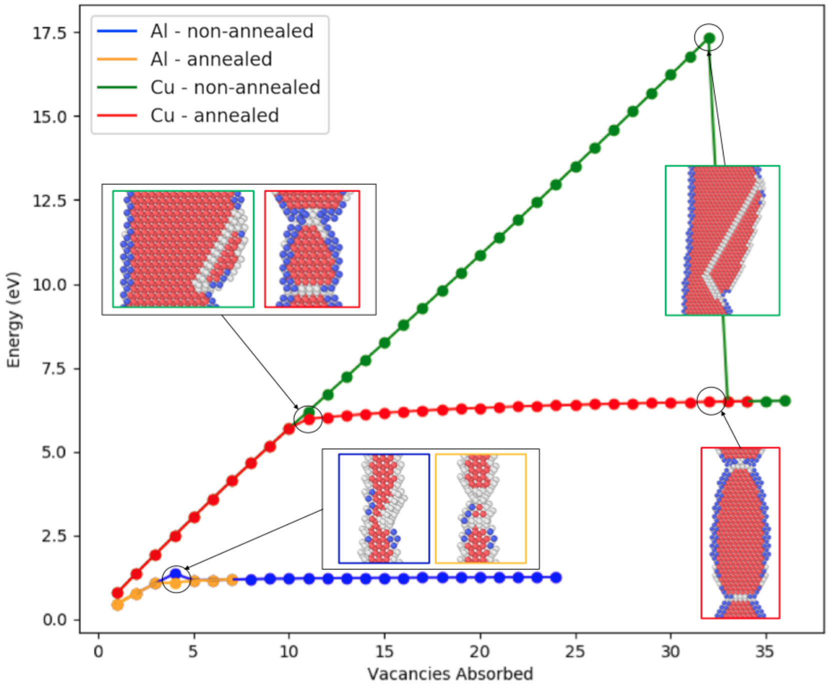

Figure 3.3: Jog-pair formation energy as a function of the number of vacancies absorbed for Al (up to 24) and Cu (up to 36). Insets show the change of the dislocation structure with and without simulated annealing, with the color of the border of the dislocation images corresponding to the color of the energy path. The dislocations were colored using the common neighbor analysis (CNA) scheme in OVITO [77, 78]. FCC type atoms were removed, red atoms represent an HCP type environment, and blue and grey represent atoms that belong to the partial dislocations or the jogs.

of structure (see blue framed inset) persists up to four (three) absorbed vacancies in the non-annealed (annealed) samples. Beyond that the jog-pair structure with a constricted and extended jog forms and addition of more absorbed vacancies leads to an increase in the distance between the jogs, with the structure of the jogs remaining qualitatively similar. The formation energies are uniformly much lower for Al than for Cu for all values of the number of absorbed vacancies. For Al, the formation energy plateaus at a value of approximately 1.3 eV.

The results for the annealed samples in Fig. 3.3 point towards the satisfaction of assumption 6 in the model of Balluffi, namely that the energy of embryonic jog pairs increases monotonically with size without the presence of an appreciable extra energy barrier to form well-formed jog pairs. However, it should be noted that for the case of the annealed sample of Cu with eleven absorbed vacancies, the constricted/extended jog-pair structure is not always found within the length of the annealing simulations using different random number seeds for the velocity distributions. This hints at the presence of an appreciable activation energy barrier from between the non-annealed and annealed structures in Cu with a decreasing number of vacancies absorbed. The energy barriers between selected pairs of annealed and non-annealed structures for Cu were thus computed from NEB calculations with results plotted in Fig. 3.4. The transition states for these configurations all show a partial constricting to meet the vacancy cluster, which is a different mechanism for jog-pair formation than that suggested by Sarkar [66] and Grilhé [82] where the vacancy cluster dissociates across the stacking fault ribbon.

The results in Fig. 3.4 show the trend of a decreasing energy barrier with increasing number of vacancies absorbed to transform from non-annealed to annealed structures in Cu. This trend is qualitatively consistent with previous calculations based on elasticity theory by Grilhé *et al.* [82]. The lower activation barriers for the larger vacancy aggregates can be understood to arise since in these structures dissociating into jog pairs does not require constricting the partials as much as in the structures with smaller vacancy aggregates. The results imply that there could be different kinetic pathways for formation of jogs in Cu depending on the temperature, where the system follows the non-annealed energetics (the green curve in Fig. 3.3) until the barrier to transform to the annealed structure (the red curve in Fig. 3.3) is low enough to be thermally activated. These different kinetic pathways could explore different directions in the displacive-diffusive space described by Sarkar *et al.* [66]. Also, it is assumed here that the vacancy cluster only spans one climb plane. With low SFE materials such as Cu, there is a possibility that jogs that span more than one climb plane could form, which would be expected to lead to more complex kinetic pathways. To properly quantify the different paths, the minimization search would need to span more than just one plane, and a large sampling size of simulated annealing attempts would be required in order to explore the lower energy structures. Afterwards, transition barriers would need to be computed between these states to find the likelihood of observing one of those states. Another strategy for finding jog structures in low SFE materials would be to adapt the procedure of Grilhé *at al.* [82] in molecular statics to find the vacancy cluster of an appropriate dimension which would lead to a spontaneous jog-pair formation. These strategies are beyond the scope of the present work, and the given results are taken as a satisfactory approximation since the simulated annealing of most of the vacancy clusters readily yield a jog-pair structure on one climb plane. A further complication to the kinetic pathway evaluation of low SFE materials is including paths where a vacancy might attach at a less energetically favorable site, such as the partial opposite of the vacancy aggregate or in the middle of the stacking fault. In the analysis of Section §3.5, the energetic pathway identified here is assumed to be the lowest energy one present for both Al and Cu.

Vacancy Hopping Barriers

As described above, one of the assumptions of the Balluffi model (assumption number 5 listed in Section §3.2) would break down if a high energy barrier exists for a lattice vacancy to be absorbed at a jog. In this sub-section, we investigate this issue employing NEB

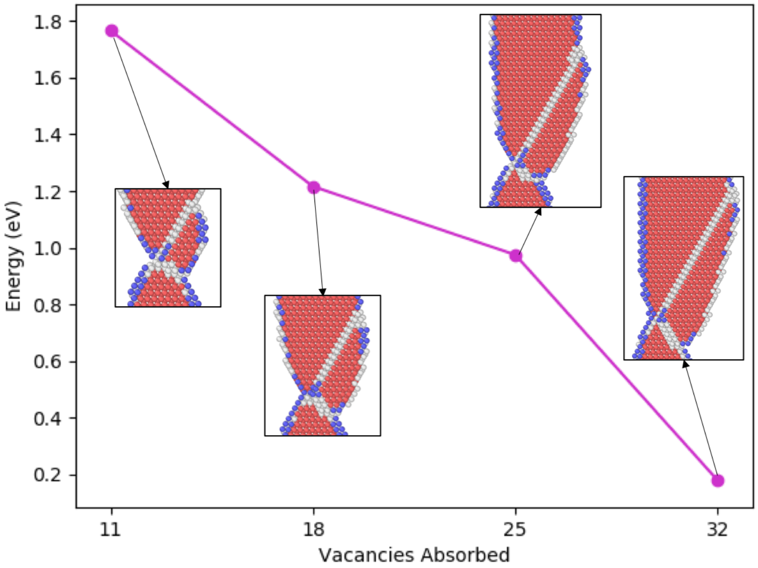

Figure 3.4: NEB barriers for Cu jog-pairs between non-annealed to annealed states. Insets show the structure of the transition state between the vacancy cluster and the jog-pair.

calculations to obtain energy barriers for vacancy hopping to the jog structures shown in Fig. 3.5 (a) and (b) for Al and Cu, respectively. For both the extended and constricted jogs in Al and Cu, a series of climbing image NEB calculations were performed of a vacancy following a tensile, compressive, or side path to the jog based on a chain of 5 closed-packed jumps in the desired direction. Figure 3.6 shows example paths for the extended jog in Cu.

The results of the NEB calculations are shown in Fig. 3.7. The zero energy value is in reference to the simulation cell without an inserted vacancy. A comparison of the compressive and tensile paths shows that the minima in the tensile paths (for jump #0: approximately 1.080 eV and 1.091 eV for the Cu extended and constricted paths, respectively, and approximately 0.708 eV and 0.712 eV for the Al extended and constricted paths, respectively) before the destruction of the vacancy is higher than those in the compressive paths (for jump #0: approximately 1.013 eV for the Cu extended and constricted paths, and approximately 0.615 eV and 0.614 eV for the Al extended and constricted paths, respectively). This is expected because vacancies are attracted to regions of compression. The final jump of the vacancy to the jog (rightmost point in the figures) for all of the paths in both materials have either the lowest migration barrier or no barrier. This indicates that high-energy constriction of partial dislocations in Cu is not necessary for a vacancy to annihilate at an extended jog. Instead, the vacancy advances the jog by dissociating into an extended jog, similar to the "1/3" vacancy mechanism discussed in [12, 83]. Note that the energy difference between

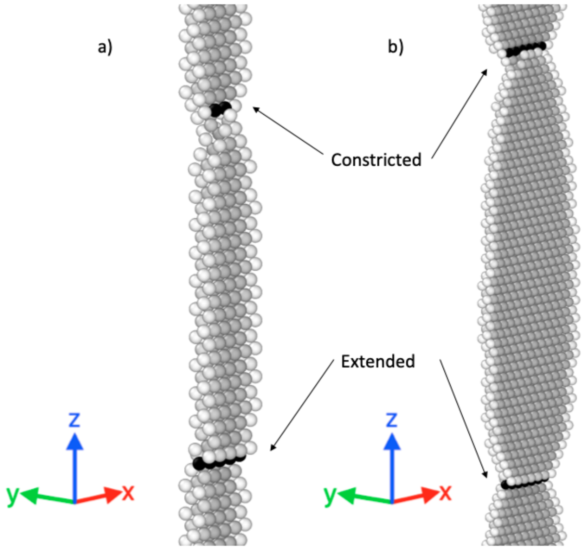

Figure 3.5: Jog structure used for NEB simulations for a) Al and b) Cu. Black atoms represent regions where absorbing a vacancy will allow a jog to migrate one atomic row.

the vacancy at position 0 and at position 5 for all the paths correspond to the value of the vacancy formation energy (where the bulk value is calculated to be 0.658 eV for Al and 1.048 eV for Cu from the respective potentials), indicating that the vacancy is annihilated from the system.

The bulk vacancy migration energy was calculated using the NEB method for a vacancy in an otherwise perfect cell with a force convergence of 0.001 eV/Å. The values were found to be 0.638 eV for Al and 0.988 eV for Cu, with the EAM potentials employed in this work. By inspection, all of the side paths seem to fit assumption 5 as they do not have barriers larger than the bulk migration energy and they are decreasing in the direction from the bulk to the jog (and thus increasing in the reverse direction). A few exceptions exist for the compressive and tensile paths (indicated by the barriers in Fig. 3.7 above the black line representing the bulk self-migration energy in the material), but the differences with the bulk migration energy are small compared to the activation barrier. The NEB calculations in [68] for a mixed dislocation in BCC Fe show that there is an angular dependence of the near core vacancy barriers for dislocation climb, which is also shown here for the FCC edge dislocation systems. Future work would be warranted to investigate this in further detail, in relation to the validity of assumption 5 of the Balluffi model. However, the results shown here suggest that the assumption is reasonable.

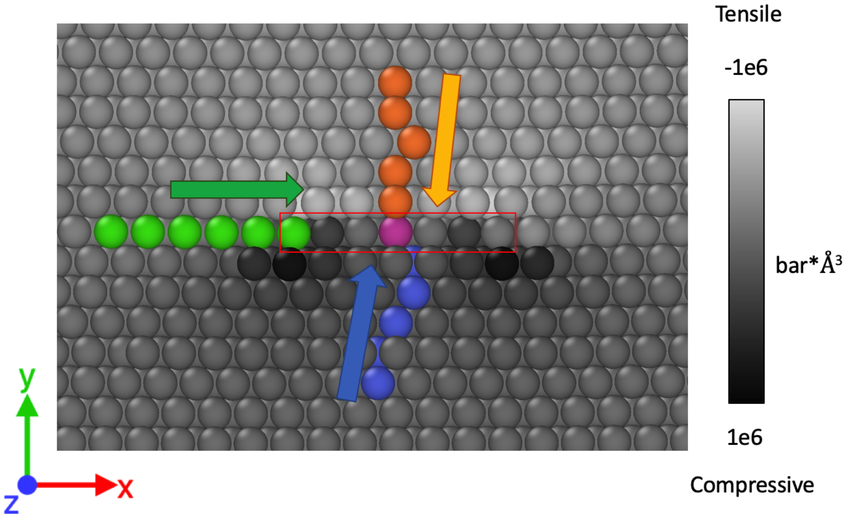

Figure 3.6: NEB vacancy paths for an extended jog in Cu looking down the z-axis. The color bar represents the hydrostatic pressure on each atom output from LAMMPS [76]. Orange atoms represent a tensile path, blue atoms represent a compressive path, and green atoms represent a side path. The red box represents the black atoms for the extended jog in Cu from Fig. 3.5.

3.5 Climb Efficiency

The results in the previous section suggest the assumptions underlying the theoretical model of Balluffi described in Section §3.2 are reasonable for describing climb velocities for straight edge dislocations in Al and Cu. In this section, the model is thus used to compute climb efficiencies for these edge dislocations using the values for the relevant parameters obtained in the calculated results presented above. Specifically, the jog-pair formation energy as a function of size can be input into Eq. (3.10) through the term $E_{jogpair}(N_{vacs})$, where we will use the values taken from the simulated annealing shown in Fig. 3.3. The maximum value of Eq. (3.10) at a fixed temperature and supersaturation will be used to find λ using Eq. (3.3). This value will need to be compared with Z, calculated through Eq. (3.2). This requires an evaluation of ΔW_{sm}, which will be taken as $0.2E_b$ as it has been shown that the self-migration energy of a vacancy in the core of an edge dislocation in FCC metals (E_c) is about $0.8E_b$ [80, 81]. The ratio of Z and λ allows for the evaluation of the dislocation climb velocity using Eq. (3.7). Once the climb velocity is evaluated, the climb efficiency is accessible through Eq. (3.8). Values for the required parameters including the calculated E_b are given in Table 3.2. Climb efficiencies are calculated up to the melting temperature as this is the limit of thermodynamic stability of the solid. Diffusivities are not included

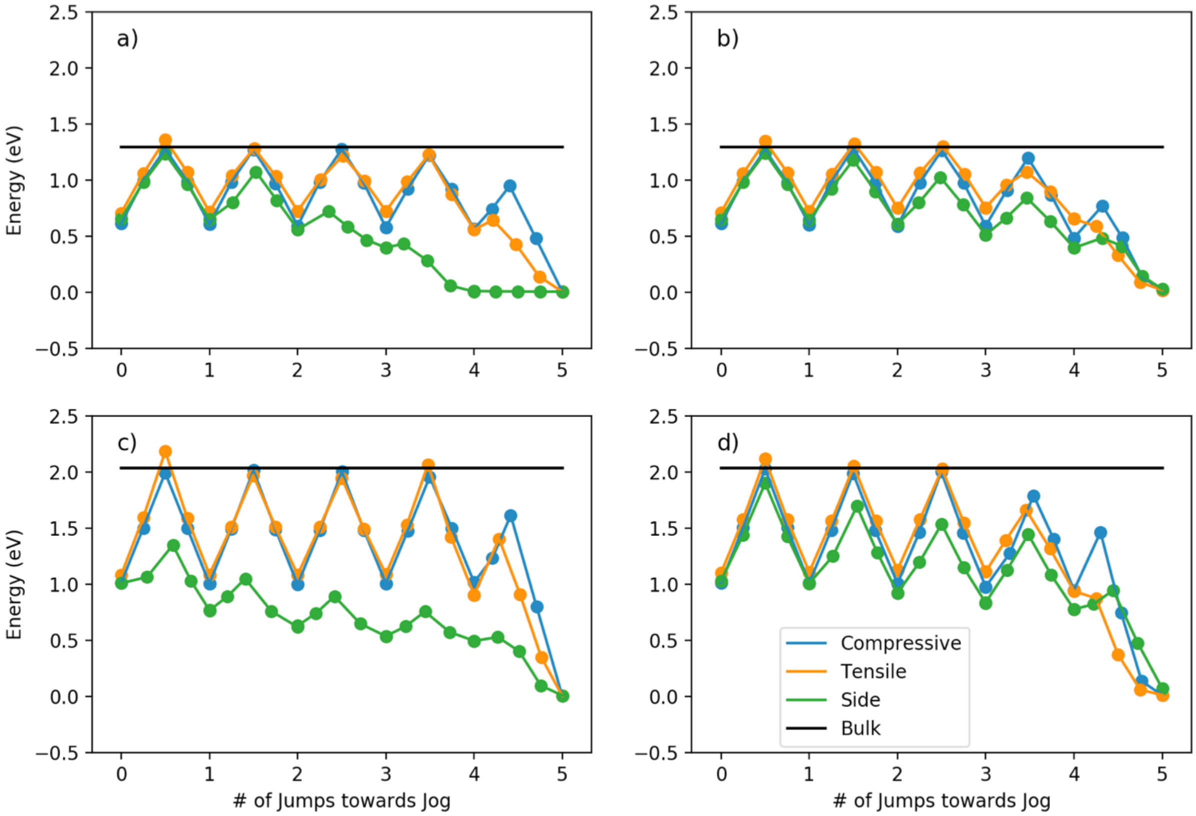

Figure 3.7: Results for vacancy energetics obtained by the nudged-elastic-band method for extended jogs in a) Al and c) Cu and constricted jogs in b) Al and d) Cu. The black line denotes the sum of the vacancy formation and migration energy in the bulk of the material. All energy values are in reference to the simulation cell without a vacancy.

because they cancel out in the expressions for climb efficiencies due to the form of Eq. (3.8). Energetics related to vacancy concentration are similarly not included because they also cancel out in Eq. (3.8) and only the ratio of the given concentration to the equilibrium concentration matters in Eq. (3.4).

The resulting values for climb efficiency are plotted as a function of homologous temperature and vacancy supersaturation in Fig. 3.8. The plots only show values where $R > \lambda$, as this is the limit of the application of the model and it is assumed that when that condition is not satisfied that climb is negligible [12]. The results for both materials feature a sharp transition from a regime of very low climb efficiencies (attachment limited kinetics) at low temperatures and supersaturations, to one of high efficiencies (diffusion limited kinetics) at

Material	$T_m(K)$	b (Å)	ρ (m^{-2})	$E_b(eV)$
Al	926	2.86	10^{12}	1.296
Cu	1353	2.57	10^{12}	2.037

Table 3.2: Values for the parameters for Al and Cu used in the Baluffi model to compute climb efficiencies as a function of temperature and vacancy supersaturation. The melting temperature is from the potential [24], and ρ is chosen as a realistic order of magnitude value in order to evaluate R in Eq. (3.5)

high temperatures and supersaturations. The sharp transition between these regimes can be interpreted to occur at values of temperature or driving force where the barriers to jog-pair formation becomes negligible relative to the thermal energy. In Fig. 3.8a), we include with the solid point a result from the multiscale simulation study of Baker and Curtin [67], where they find that an edge dislocation in Al becomes a fully efficient sink at a supersaturation around 145 at a temperature of 600 K. Even though a different potential was used, the results of Baker and Curtin are near our predictions of where the transition to a high climb efficiency at the same temperature occurs. While they did apply a large climb stress (around 1 GPa, while keeping the hydrostatic stress equal to zero), our results are consistent with theirs in the sense that we find that it takes a similar number of vacancies to form a jog-pair (4 in our study, 4 in [67]) with a similar potential energy cost (at 4 vacancies, our jog-pair formation energy is around 1.1 eV, and an estimate of the summation of the first 4 points in Fig. 4 in [67] leads to 1.2 eV). It would be of interest for future work to employ the multiscale methodology to other regimes of temperature and supersaturation to investigate whether the transition between low and high climb efficiencies matches the predictions from the present approach.

The results in Fig. 3.8 show that Al has a wider range of homologous temperatures and supersaturations where the efficiencies are considerably higher than for Cu. This qualitatively agrees with experimental observations [49, 50] indicating lower climb efficiencies in systems with lower stacking fault energies. The results are also plotted as climb efficiencies as a function of driving force in Fig. 3.9 using Eq. (3.4). These plots show that at a high enough driving force, even a low SFE material can become climb efficient, consistent with experimental conclusions [55, 51]. This suggests that for design of alloys that are resistant to creep, a material with a low-stacking fault energy is preferred, in agreement with Yu and Wang [65], in order to minimize effects due to dislocation climb. Additionally, in the design of materials where void nucleation in irradiated materials should be avoided (such as in Gu *et al.* [64]), a high-stacking fault energy is preferred to lower the jog-pair formation energy, thereby increasing the number of vacancy sinks. The results also demonstrate the limits to the assumption that dislocation climb in a material can be described by either a purely diffusion-limited or attachment-limited model, given that the appropriate behavior can change over time if the supersaturation or temperature are evolving. For such cases,

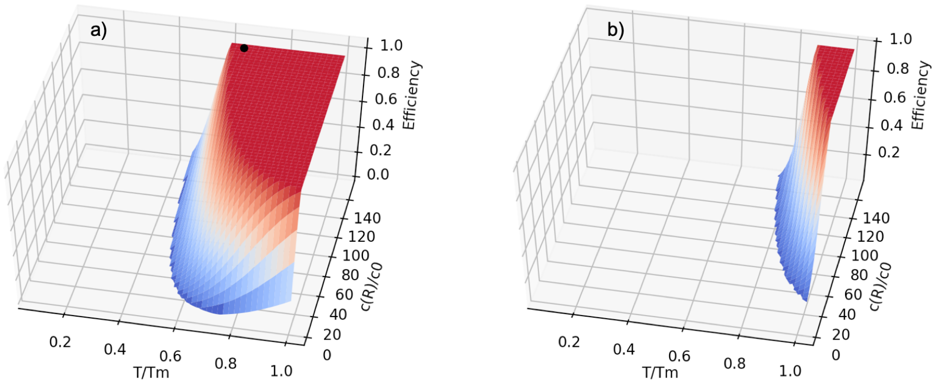

Figure 3.8: Plots of edge dislocation climb efficiencies of a) Al and b) Cu as a function of homologous temperature and ratio of increased concentration. The jog-pair formation energy values were taken from the annealed pathways. The black dot in a) represents a $\frac{c(R)}{c_0}$ ratio of 146 and a climb efficiency of 1 at a temperature of 600 K, which is meant to mimic the result in [67].

mesoscale models capable of describing mixed attachment and diffusion contributions to climb velocities are required, and for such models atomistic simulations like those employed in this study can be used to provide the necessary material parameters.

It is worth noting that the formalism presented in this section neglects the effects of applied stresses and internal stresses due to neighboring dislocations on the vacancy flux and climb rate, and thus it is appropriate only in the limits where the driving force for climb associated with vacancy supersaturation is dominant. We note that in addition to changing the driving forces for climb, these applied and internal stresses can also affect the factors governing climb efficiency. For example, compressive (tensile) stress along the dislocation glide direction is likely to decrease (increase) the jog-pair formation energy and thus affect the values of the driving force where there is a transition in the climb efficiency. These stresses could also affect diffusion towards and along the dislocation [84], considering either vacancy or interstitial mechanisms [47], and thus affect the mean-free path defined in the Ballufi model. An additional effect is associated with an Escaig stress, which would change the dissociation distance between partial dislocations in the core, with an associated effect on jog-pair formation energy as described above and in the Supplementary Material document for this chapter. Overall, further work would be needed to fully characterize the effects of applied and internal stresses on dislocation climb efficiency, and for such studies atomistic kMC models that incorporate stress-dependent values of the different vacancy hops to and from the jogs and straight dislocation segments would be required. The present results,

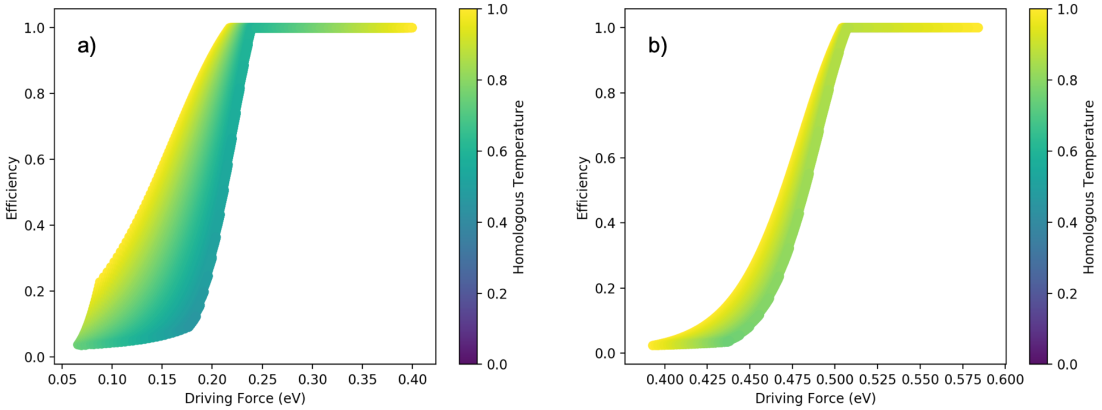

Figure 3.9: Plots of edge dislocation climb efficiencies of a) Al and b) Cu as a function of driving force. The shading represents homologous temperature.

which consider the role of vacancy supersaturation alone, provide useful benchmarks for further such future studies.

3.6 Conclusions

Atomistic calculations based on EAM potential models for FCC Al and Cu have been employed in studies of jog formation energies and vacancy migration energies near jogs, for the purpose of investigating kinetics of dislocation climb in these representative high and low stacking fault metals. The atomistic results identify low-energy jog-pair structures with varying amounts of absorbed vacancies using simulated thermal annealing. Calculations of energy barriers between different jog-pair structures revealed the existence of a complex kinetic pathway for jog-pair formation in Cu, which likely exists for other low SFE materials more generally. The calculations further demonstrate that there is a tendency for vacancy migration barriers to decrease when moving from the bulk to a jog. The atomistic calculations are used to derive parameters in the theoretical model of climb velocities due to Balluffi [12], to compute climb efficiencies of Al and Cu across varying temperature and vacancy supersaturations. The higher SFE Al system was found to display higher climb efficiencies than Cu over a wide range of temperatures and supersaturation, in agreement with experimental observations that higher SFE materials show higher efficiencies for climb [47, 49, 50, 51]. The effect of applied stress on climb efficiency was not pursued here, but can be incorporated in the presented method by calculating the relevant vacancy and jog-pair energetics under the desired stress state. The atomistic inputs derived here to calculate climb efficiency are also necessary for describing mixed kinetic regimes in mesoscale simulations of dislocation climb. The results thus demonstrate how atomistic simulations can be used to improve the generality and accuracy of mesoscale models of material response under creep, annealing, and irradiation conditions.

Chapter 4

Modeling the Effect of Short-Range Order on Cross-Slip in an FCC Solid Solution[1]

4.1 Introduction

Short range-ordering (SRO) (as well as short range-clustering) in face-centered cubic (FCC) solid solution alloys has been shown to lead to pronounced effects on deformation microstructure and associated mechanical behavior beyond the yield point [86, 87, 88, 89, 90, 91, 92, 93, 94]. The formation of a diffuse anti-phase boundary (DAPB), a planar fault with altered SRO caused by the passage of a leading dislocation, provides additional resistance to dislocation glide by an amount that scales with the magnitude of the DAPB energy per unit area (γ^{DAPB}) [95]. The presence of SRO has also been shown to increase the stacking fault energy (SFE) [96, 92], as well as increase the work-hardening rate [86, 91, 89, 90, 92, 94]. Such an effect on mechanical properties can have profound implications on the deformation behavior of single-phase concentrated solid solutions, including high and medium-entropy alloys (HEAs and MEAs). An expanded understanding of the link between SRO and deformation behavior in the latter multicomponent alloys would benefit from a better understanding of the same underlying mechanisms in more simple binary concentrated solid solutions. A phenomenon commonly observed in both classes of alloys containing SRO is planar slip, or the localization of dislocation glide in planar arrays.

Typically the origin of planar slip has been linked to a few potential sources: a decrease in the SFE and an increase in friction stress on partial dislocations with alloying [97], thus suppressing cross-slip, or an increase in SRO [87]. The former seems unlikely, as recent studies

---

[1] The results presented in this chapter and the corresponding Supplementary Material document have been published as a regular article titled "*Modeling the Effect of Short-Range Order on Cross-Slip in an FCC Solid Solution*" in Acta Materialia, **226**, 117615, (2022), doi: 10.1016/j.actamat.2021.117615 by Anas Abu-Odeh, and Mark Asta [85]. The material is presented here with the permission of co-authors and publishers.

in cross-slip in disordered FCC solid solution alloys have shown that an increase in alloy concentration increases the spread of cross-slip activation energy barriers, thus increasing the probability of low activation energy barriers [98, 99]. In a material with SRO, a lead dislocation in a planar slip array will create a DAPB, while subsequent dislocations will feel reduced resistance to glide as they do not need to perform the work to disrupt SRO, leading to a slip-plane softening effect. The role of the DAPB is evidenced by a correlation of planar behavior with the presence of SRO compared to a lack of correlation with change in SFE [87]. While SRO appears to have an effect on cross-slip behavior, we are unaware of previous work investigating the role of local ordering on the energetics underlying this process. Progress in this direction is warranted given the relevance to understanding SRO effects on work-hardening behavior. Planar slip has been linked to decreased cross-slip [87, 97], which could lead to a decrease in dynamic recovery, as well as an increase in internal stress concentration, which may increase the amount of twinning in certain alloys resulting in a dynamic Hall-Petch effect [100]. Such increases in work-hardening resulting from SRO, particularly during later stages of deformation, could lead to a delay in the Considère criterion, which allows for an increase in ductility. Even though SRO may reduce the total cross-slip rate, the existence of a DAPB implies that if a dislocation undergoes cross-slip, following dislocations are much more likely to cross-slip at that same site than otherwise. This can lead to correlated cross-slip or double cross-slip, which can create dislocation debris that further work-harden the material [13, 101].

Previous simulation-based and theoretical studies on the effect of SRO on mechanical properties have largely focused on the calculation of the DAPB energy and its effect on strengthening. Through the input of the Warren-Cowley (WC) SRO parameters [102] and effective pair interactions, estimates of the effect of the DAPB contribution to strength have been made considering first [103], second [104], and even sixth [105] nearest neighbor pairs. Inverse Monte-Carlo (MC) can be performed on diffuse scattering measurements, which quantify SRO, in order to obtain effective pair interactions that can be used to estimate a DAPB energy considering many nearest neighbor shells [106, 107]. Density-functional theory (DFT) based cluster expansion can also provide an estimate for the DAPB energy based on the equilibrium ordering state [108]. This can also be calculated directly from DFT-based MC, along with the change in the SFE with ordering [92, 96]. The effect of SRO on the resolved shear stress of a dislocation has also been calculated using embedded-atom method (EAM) potential based techniques on a model MEA [109] and HEA [110]. Overall, these previous studies have provided estimates of DAPB energies in concentrated binary FCC alloys ranging between 5 and 25 $\mathrm{mJ/m^2}$, and for medium and high-entropy alloys a larger range of between 4 and 123 $\mathrm{mJ/m^2}$ have been computed. Computational studies of the effects of SRO, lattice distortion, and nanocrystalline grain sizes on a model MEA showed that all of these factors increased glide resistance in the alloy [111]. Phase-field dislocation dynamics (PFDD) simulations have been used to investigate the effect of the variance and correlation of SFE distributions, mimicking some of the effect of SRO (albeit without the DAPB), in order to study its effect on strengthening and Frank-Read source activation [112, 113].

Despite the extensive previous work related to SRO effects summarized above, the role of local ordering on cross-slip behavior has not been investigated in detail. Nevertheless, previous work for pure FCC metals or random solid-solution alloys provide important insights that form the basis for such investigations. Such previous work has typically focused on either the Friedel-Escaig mechanism or the Fleischer mechanism of cross-slip [47]. A study based on a Ni EAM potential investigated the ability of Schmid and Escaig stresses to reduce the cross-slip energy barrier [114]. A molecular dynamics (MD) study of a screw dislocation dipole in Cu showed that cross-slip kinetics are reliably represented by an Arrhenius form [115]. A combination of MD and a concurrent-atomistic-continuum method showed that a transition between the Friedel-Escaig mechanism to a Fleischer mechanism could occur depending on the Schmid stress in the cross-slip plane and dislocation line length in Ni [116]. Further EAM-based studies explored the effect of complex stress states on the cross-slip barrier in Al [117], as well as the effect of such stress states on the barrier and transition between the Friedal-Escaig mechanism to the Fleischer mechanism in Ni [118]. A study on a Ni-Al solid solution showed that the introduction of repulsive Al-Al pairs could have a dramatic impact on the cross-slip energy [119]. A MD study of a model HEA has shown that cross-slip in highly concentrated alloys can happen at activation energies that are much lower than what might be predicted using elasticity theory [120]. This can be explained by a pair of studies on the effect of random FCC solid solutions on cross-slip, which show that high concentrations of solute can result in a high variance of cross-slip energies [98, 99]. In particular, the low energy tail of these distributions are likely to dominate cross-slip rates due to the exponential Arrhenius form of the transition rates. Based on these results, the latter of these two studies suggested that the correlations imposed by SRO would reduce the spread of cross-slip energy barriers, thus lessening access to the low-energy tail of the distribution compared to the disordered case.

In this paper, we build on this previous body of research and explicitly investigate the effect of SRO on cross-slip in a binary FCC substitutional solid solution through atomistic simulations of a Ni-10 at%Al alloy modeled with an EAM potential [80]. As will be discussed in Sections 4.3 and 4.4, the investigated SRO state of this alloy is reflective of many other FCC alloys due to comparable values of the WC SRO parameters and DAPB energy, as compared to those reported for other FCC systems. We find that SRO does not just reduce the spread of cross-slip activation barriers, but also increases the energy of the final state during the cross-slip process compared to the initial state when no DAPB is present in the cross-slip plane. This work is undertaken by limiting possible cross-slip events in a planar array to a few idealized cases: cross-slip at the head of a planar slip array, cross-slip between two glide planes possessing DAPBs (where either half or all of the cross-slip plane is a DAPB), and cross-slip out of a glide plane with a DAPB (Fig. 4.1). These are compared to each other as well as to the situation for the corresponding random solid-solution alloy at the same composition. Before investigating these situations in atomistic detail, an analysis of the effect of SRO on cross-slip is carried out using linear elasticity theory in Section 4.2. The methods used to equilibriate SRO in model simulation supercells are discussed in Section 4.3. Calculations of planar defect energies (SFE and DAPB formation energies) are reported in Section 4.4. Results of calculations of different cross-slip energies are presented in Section 4.5. A discussion of how these results point towards a framework to understand planar slip in FCC alloys, correlated cross-slip, and decreased dynamic recovery is presented in Section 4.6. We conclude in Section 4.7.

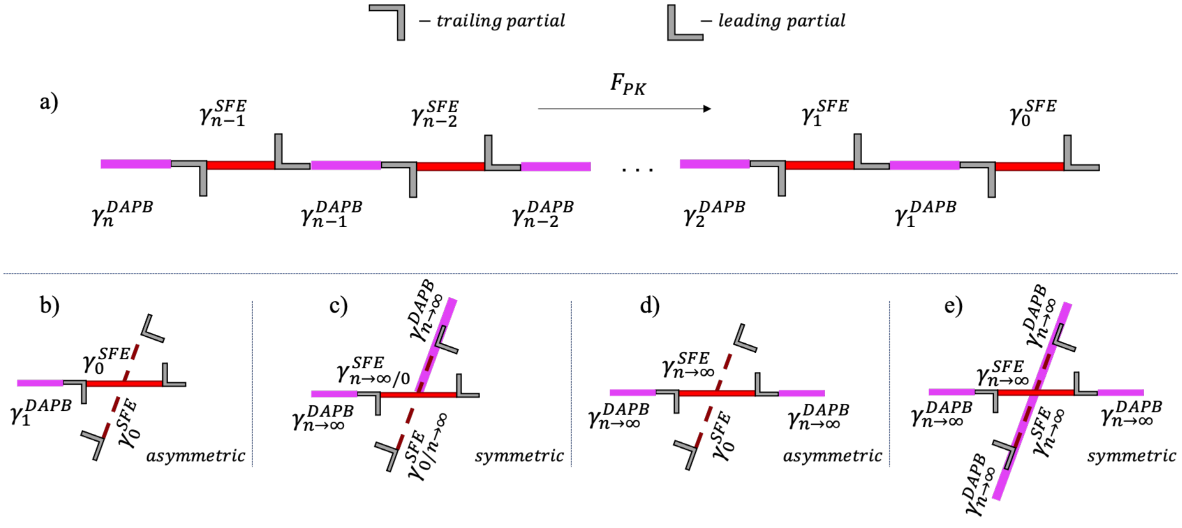

Figure 4.1: An array of screw dislocations in a planar slip configuration is shown in a). The arrow represents the direction of motion given an applied Peach-Koehler force F_{PK}. A red line (a dashed red line when in the cross-slip plane) represents a stacking fault between two partials, and a purple line represents a DAPB between two screw dislocations. The values of the planar fault energies (stacking fault energy, γ^{SFE}, and diffuse antiphase boundary energy, γ^{DAPB}) are dependent on the number of dislocations that have have already slipped on the plane, as indicated by the subscripts. Cross-slip at the head of the array is shown in b). The case where a dislocation is following the head dislocation through cross-slip is shown in c). Cross-slip out of a DAPB is shown in d). Cross-slip out of a DAPB into another DAPB is shown in e). These cases are labeled as symmetric or asymmetric depending on whether or not the energy of the system (considering just the isolated dislocation) is the same in the initial and the final state in the absence of applied stress. In the cross-slip plane, we define the leading partial dislocation to be above the original glide plane while the trailing partial dislocation is below.

4.2 The Effect of SRO on the Initial and Final States of Cross-Slip

As discussed above, the presence of SRO will result in two major changes in planar defect energies compared to the random case: the presence of a DAPB energy and an increase in the SFE. Consider a planar slip configuration of dissociated screw dislocations, as illustrated in Fig. 4.1(a), where the dislocation furthest to the right is the head dislocation. Fig. 4.1(b) shows the case where the head dislocation cross-slips into a region of unbroken SRO and illustrates the types of planar fault energies involved. Fig. 4.1(c) shows the case where a dislocation far behind the head dislocation cross-slips at a site where many of the leading dislocations have already cross-slipped. Fig. 4.1(d) shows the case where a dislocation far behind the head dislocation cross-slips into a region of unbroken SRO. Finally, Fig. 4.1(e) shows the case where a dislocation far behind the head dislocation cross-slips into a region of broken SRO. These selected cases are chosen in this work to illustrate the importance of the role of the SFE and DAPB energy as a function of number of slips as well as their presence on the cross-slip plane for the cross-slip activation barrier. In this section, we show through a standard theory of the elastic interaction of the Volterra fields of partial dislocations that a difference in energy per dislocation line length between the initial and final states is expected for the cases shown in Fig. 4.1(b) and Fig. 4.1(d). The cases in Fig. 4.1(c) and Fig. 4.1(e) are expected to be symmetric (on average) in chemical environment with respect to the initial and final states, and so will not be considered in this section. We also postulate that for a dislocation of increasing length, the higher energy in the cross-slipped state characteristic of the cases in Fig. 4.1(b) and (d) makes it increasingly difficult for a screw dislocation to access low energy cross-slip barriers that might be available due to locally varying solute environments.

To facilitate this discussion, we define a DAPB fault energy per unit area as:

$$\gamma_n^{DAPB} = \frac{E_n - E_{n-1}}{A} \tag{4.1}$$

where E_n is the energy of the system after relative shifts on the same glide plane, by the glide of n dislocations with the same Burgers vector for a full a dislocation ($\frac{a}{2}\langle 110\rangle$, a being the FCC lattice constant) of the two half-crystals above and below the slip plane, and A the area of the slip plane. Note that this notation differs from what is commonly found in the literature, where γ_n^{DAPB} typically represents a cumulative DAPB energy (which we represent as $E^{DAPB}(N)$, defined below in Eq. 4.11). Eq. 4.1 is defined for n greater than zero and is meant to represent the incremental energetic cost per unit area encountered when the nth dislocation glides across an area A At large n, γ_n^{DAPB} will tend to zero. The strengthening due to DAPB formation is given by [95]:

$$\tau_n^{DAPB} = \frac{\gamma_n^{DAPB}}{b} \tag{4.2}$$

where b is the magnitude of the Burgers vector of a full dislocation, given by $a/\sqrt{2}$. We define the SFE as:

$$\gamma_n^{SFE} = \frac{E_n^{partial} - E_n}{A} \tag{4.3}$$

where $E_n^{partial}$ is the energy of the system after glide of a partial dislocation of Burgers vector $(\frac{a}{6}\langle 112\rangle)$ slip is superimposed after n slips of a full Burgers vector on the same glide plane.

Cross-Slip at the Head of a Planar Array

Here we consider a screw dislocation at the head of a planar array (Fig. 4.1(b)) at an equilibrium dissociation width. For simplicity we neglect interactions with other dislocations in the planar slip array. Consider the force balance on each partial dislocation as illustrated in Fig. 4.2. For the leading and trailing partials (Eqs. 4.4 and 4.5, respectively), the force balance results in:

$$\frac{K_{int}}{r_g} = \gamma_0^{SFE} - \frac{\tau_{sch}^{g} b}{2} \tag{4.4}$$

$$\frac{K_{int}}{r_g} = \gamma_0^{SFE} - \gamma_1^{DAPB} + \frac{\tau_{sch}^{g} b}{2} \tag{4.5}$$

where K_{int} represents an interaction constant between two partial dislocations when only considering the elastic interaction of the Volterra fields [47, 48], τ_{sch}^{g} is the Schmid stress in the glide plane (or the resolved shear stress on the perfect screw dislocation), and r_g is the separation distance of the two partials in the glide plane. Setting Eqs. 4.4 and 4.5 equal to each other results in:

$$\frac{K_{int}}{r_g} = \gamma_0^{SFE} - \frac{\gamma_1^{DAPB}}{2} \tag{4.6}$$

In order for Eq. 4.6 to hold, τ_{sch}^{g} must equal τ_1^{DAPB}. When considering an applied Escaig stress (a stress which only acts on the edge components of the partials), an additional term of $b\tau_{esc}/(2\sqrt{3})$ would appear on the right-hand side of Eq. 4.6. If τ_{sch}^{g} is lower (higher) than this threshold, it is moving left (right), removing (extending) the DAPB.

The difference in energy between a dislocation in the cross-slip plane and the original glide plane can be estimated considering the difference in total fault energies before and after the cross-slip transition (ΔE_{fault}), the effect of bow-out in the cross-slip plane, and the effect of a difference in elastic interaction energies of the partial dislocations in the cross-slip plane and the original glide plane (these are the typical contributions considered for cross-slip in FCC metals and alloys [114, 99, 117, 118]). In order for the energy of the initial state and the final state to be equal, the sum of all of these terms must be set to zero resulting in:

$$\Delta E_{fault} + lE_{ele} + E_{bow}(\tau_{sch}^{cs}, l) + E_x = 0 \tag{4.7}$$

where E_{ele} represents the change in the partial dislocation interaction energy per unit length of a dislocation spread in the cross-slip plane versus the glide plane, E_{bow} represents the effect

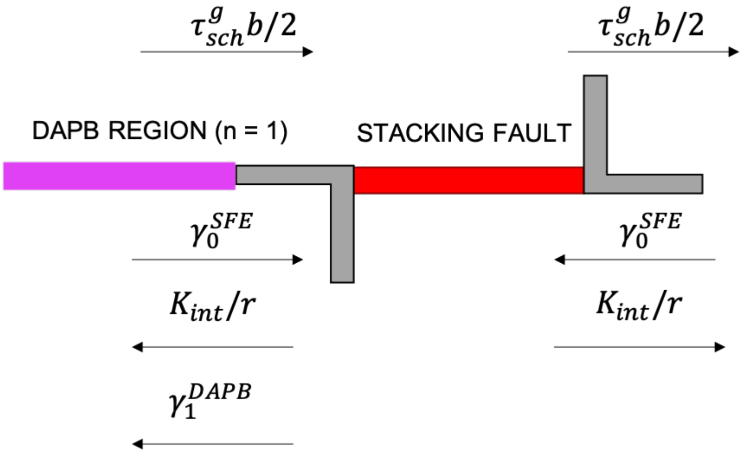

Figure 4.2: The force balance on each partial dislocation associated with the head dislocation in a planar array due to an applied Schmid stress, the stacking fault energy, the DAPB energy, and the elastic repulsion between the partial dislocations.

of a bow-out in the cross-slip plane (τ_{sch}^{cs} being the Schmid stress projected in the cross-slip plane), and E_x includes possible cross-terms that can arise. When considering the effect of bow-out, it should be made clear that in cases where the dislocation cross-slips into a region of unbroken order, the effect of forming a DAPB (Eq. 4.2) will make it more difficult for the dislocation to bow-out. So it is natural to expect that in these cases, the contribution of the bow-out effect will be reduced compared to cross-slip in a fully random structure. The effect of E_{ele} is not as trivial to consider. In order to isolate the effect of E_{ele}, for the remainder of this section we will take τ_{sch}^{cs} to be zero and ignore bow-out effects. Following Refs. [47, 99], E_{ele} can be described as:

$$E_{ele} = -K_{int} \ln \frac{\gamma_g}{\gamma_{cs}} \tag{4.8}$$

where γ_g is the effective SFE in the glide plane (for the case of cross-slip at the head of a planar array this will be equal to $\gamma_0^{SFE} - \gamma_1^{DAPB}/2$), and γ_{cs} is the effective SFE in the cross-slip plane (γ_0^{SFE}, as there is no DAPB in the cross-slip plane in this case). The effective SFE can be obtained from the right hand side of a force balance on the partial dislocations similar to Eq. 4.6, and will be dependent on the SRO environment as well as an applied Escaig stress. Eq. 4.8 represents the difference in the elastic interaction of the partial dislocations in the different slip planes. Without the aid of an Escaig stress, this will always result in an increase in energy per unit length when a head dislocation in a planar slip array cross-slips in a material with SRO. This means that after a cross-slip nucleus has formed, the energy of the system will continuously increase as the nucleus grows along the dislocation line.

The first term in Eq. 4.7 disappears as (through the use of $K_{int}/r_g = \gamma_g$ and $K_{int}/r_{cs} = \gamma_{cs}$):

$$\frac{\Delta E_{fault}}{l} = \gamma_{cs} r_{cs} - \gamma_g r_g = K_{int} - K_{int} = 0 \tag{4.9}$$

where r_{cs} is the separation distance of the two partials in the cross-slip plane. This is an important result on its own, because it states that the energy involved with the creation or destruction of a part of a planar defect during cross-slip should not have an impact on the cross-slip barrier (at least for the case where τ_{sch}^{cs} is zero). Note that while γ_g and γ_{cs} are dependent on the SRO environment and Escaig stresses, the result of Eq. 4.9 is not. So the only remaining term in Eq. 4.7 that needs to be considered is E_{ele}. In order for Eq. 4.7 to be satisfied in a material with SRO, some Escaig stress state must be applied, because otherwise E_{ele} will be positive according to Eq. 4.8. This can be interpreted as originating from a stronger interaction of the Volterra fields of the partial dislocations in the cross-slip plane than in the glide plane. This contribution to the activation barrier for cross-slip is absent in a random solid solution alloy, due to the lack of a presence of a DAPB.

Cross-Slip Out of a DAPB

We consider next the case of the cross-slip of a dislocation for a dislocation far behind the lead dislocations in the array, where many dislocations have already passed along the glide plane to give rise to a fully formed DAPB with $\gamma_{n\to\infty}^{DAPB} = 0$. In this case, illustrated in Fig. 4.1(d), even though the DAPB energy γ_n^{DAPB} is zero, the difference in SFE in the final and initial state will cause a similar effect as described in the previous subsection. As n increases, γ_n^{SFE} will plateau to a value less than that of γ_0^{SFE}. The effective SFE in the glide plane (γ_g) for this case is $\gamma_{n\to\infty}^{SFE}$. When there is no Escaig stress present, Eq. 4.8 will be positive and Eq. 4.7 will not be satisfied. This scenario is going to be representative of most of the dislocations following the head of a planar slip array as the value of $\gamma_{n\to\infty}^{SFE}$ will be reached after a small number of slips n. Similar to the previous case, the increase in energy can be interpreted as an increase in the elastic interaction of the partial dislocations in the cross-slip plane, and this effect will again be absent for the case of a random alloy.

4.3 The Model System and Methods for Equilibriating SRO

The analysis in the previous section suggests that the presence of SRO as well as the presence of a DAPB can significantly influence the cross-slip energy barriers due to differences in energy between the final and initial state. In this section and the next, we present atomistic simulations results to augment the continuum analysis. We begin by discussing in this section the atomistic simulation methods to equilibrate the SRO.

In this work we focus on Ni-10%Al FCC subsitutional alloys, modeled by an EAM interatomic potential [80]. All of the energy calculations and atomistic simulations were performed using the LAMMPS software [76]. The potential was chosen because it gives rise to good agreement bewteen WC SRO parameters calculated and reported from experimental measurements [121, 122] as described below and in Fig. 4.3. The equilibrium state of SRO was derived from an initially random Ni-10%Al solid solution through the use of a hybrid MC/MD approach using the variance constrained semi-grand-canonical ensemble [34] for MC and the NPT ensemble for MD with a Nosé-Hoover thermostat and barostat. After an initial MD equilibration period for a random alloy, used to bring the system to the target conditions of zero pressure and a temperature of 700 K, MC atom-type switches were carried out after every 100 MD steps (with a timestep of 0.003 ps) with a swap fraction of 0.1, a chemical potential difference of 0.8 eV, and a variance constraint parameter of 1. The value of the chemical potential difference was determined from an initial semi-grand-canonical MC/MD at 700 K, as the value that would give the desired concentration of approximately 10%Al. The chosen variance constraint parameter led to a fluctuation in the desired concentration of less than 0.1%. After 20,000 MD steps, the system was found to be at an equilibrium SRO state, based on the monitoring of the convergence of the average energy. The same simulations were used for initializing the SRO state for the investigation of planar defect energies as well as cross-slip energy barriers.

To probe the SRO of the system after the hybrid MC/MD equilibration process, the WC parameters are calculated according to their definition [102]:

$$\alpha^k_{Al} = 1 - \frac{Z^k_{Ni}}{c_{Ni} Z^k} \tag{4.10}$$

where Z^k represents the total number of atoms in a kth nearest neighbor shell, Z^k_{Ni} represents the average number of Ni atoms found in a kth shell around an Al atom, and c_{Ni} is the concentration of Ni atoms in the system. A negative value of α represents local ordering (preference for unlike-atom pairs), a positive value represents local clustering (preference for like-atom pairs), and a value of zero represents random disorder. A plot of the calculated equilibrium WC parameters as a function of neighbor shell for the model Ni-10%Al alloy is shown in Fig. 4.3, and compared to two sets of measured results derived from diffuse X-Ray scattering measurements [121, 122], for alloys of the same composition aged at comparable temperatures of 973 K and 673 K, respectively. The calculated WC parameters are in good quantitative agreement with measurements for the nearest-neighbor, where the value is insensitive to temperature. At the more distant shells, the present calculated results at 700K have magnitudes near those measured for the alloy aged at 973 K. The calculated values oscillate in the same way as the measured WC parameters, consistent with L1$_2$ ordering characteristic of the stable Ni$_3$Al intermetallic phase. Unlike the long-range-ordered intermetallic, however, the WC parameters for the Ni-10%Al short-range-ordered alloy decay to small values near zero at distant neighbor shells, namely beyond the fifth shell in the present calculations.

Only one annealing temperature is used as it is clear from previous studies that a lower (higher) temperature will simply increase (decrease) the values of γ^{DAPB}_1 and $\gamma^{SFE}_0 - \gamma^{SFE}_{n\rightarrow\infty}$ due to an increase (decrease) in SRO [96, 109, 110]. The qualitative results of this study will be independent of the level of SRO, but we are focusing on a case here where the SRO is representative of the magnitudes observed experimentally at reasonable annealing temperatures. The values of the WC parameter of the first two shells for this annealing temperature are also found to be typical of those obtained from experiments of many other FCC binary solid solution alloys. Values of approximately ∓0.05 to ∓0.1, where the minus sign is for the first shell and the plus sign is for the second shell, are found for Ni-Cr [123, 124, 125], Ni-Fe [126], Cu-Au [127, 128], Cu-Zn [129], Cu-Mn [130, 131], and Cu-Al [132] solid solution alloys. We use one concentration of Al as larger concentrations of Al in this potential incur the risk of entering a two-phase region where the precipitation of a second phase is possible. Even in an alloy with a wider range of solubility, the effect of concentration simply serves to change the average cross-slip barrier and its standard deviation [98], so the general theory and conclusions of this study are unaffected by this choice.

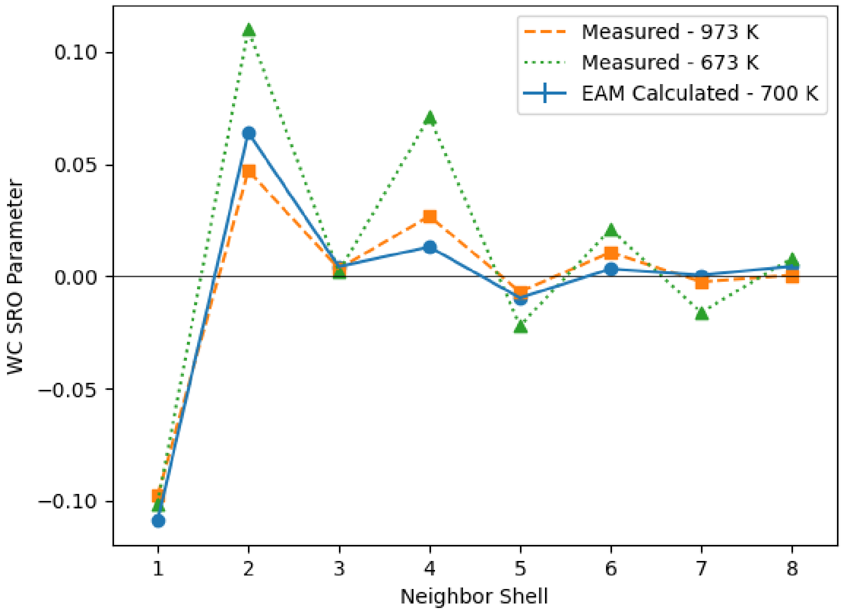

Figure 4.3: WC SRO parameters for a Ni-10%Al alloy plotted versus neighbor shell. Calculated results obtained in the present work are plotted with blue symbols and connecting lines, using the average WC SRO parameters of 10 independent supercells with 738,720 atoms. Error bars representing the standard deviation of the WC SRO parameters are smaller than the markers. Measured values at 973 K [121] and 673 K [122] are plotted in orange and green, respectively.

4.4 Planar Defect Energies

Methods

We consider in this section calculations of the effect of SRO on the DAPB energy and SFE. To minimize finite-size effects and enable effective spatial averaging over the distribution of local environments, we employ in these calculations relatively large supercells containing 4,032,000 atoms, initialized with a random arrangement of Ni and 10 at.%Al atoms over the sites of an FCC lattice. The cell was oriented with the x-axis in the [110] direction, the y-axis in the $[\bar{1}12]$ direction, and the z-axis in the $[1\bar{1}1]$ direction, with lengths of approximately 120 nm, 30 nm, and 12 nm, respectively. After initialization with a random alloy configuration, the atomic positions in the cell were first relaxed using a mix of the FIRE algorithm [75, 133] and the conjugate gradient algorithm in LAMMPS, including relaxation of the periodic lengths in order to ensure zero stress conditions. Afterwards, free surfaces were introduced normal to the z-direction, and the atomic positions were relaxed again using the FIRE algorithm, holding the periodic lengths in the x and y directions fixed. Calculations for samples with SRO made use of supercells obtained in the same manner, but with the atomic configuration equilibrated using the same type of hybrid MC/MD simulations described in Section 4.3, at 700 K.

In order to determine the SFE, 21 layers in the middle of the cell were chosen to separate two half-crystals which were displaced relative to each other by a partial Burgers vector of the $\frac{a}{6}\langle 112\rangle$ type (where a is the FCC lattice constant). The atomic positions were subsequently relaxed. A total of 63 points were averaged for each SFE calculation (21 layers with 3 different shift directions). For samples with SRO, the SFE is a function of the number of full dislocation slips that have passed through the plane. Therefore, 63 points are averaged for each SFE calculation as a function of the number of slips (0-10) of a full dislocation with a Burgers vector of the $\frac{a}{2}\langle 110\rangle$ type. The DAPB energy is also calculated for these supercells with SRO as a function of slip, the difference being that the relative displacement of the two half-crystals is of a full Burgers vector.

The supercells and methods described above are used to compute the planar defect energies. For the case of SFE, further calculations are carried out to determine the distribution of fault energies for narrow ribbon-like geometries characteristic of those in the cores of the dissociated screw dislocations under investigation in the next section. In these additional calculations, 10 supercells of 738,720 atoms were used with the same orientation as above but with lengths in the x-, y-, and z-direction of approximately 15 nm, 23 nm, and 23 nm, respectively for both random and SRO cases. Using the center plane of each cell, each area is divided into 18 groups along the y-direction each with an area of 19.2 nm^2, so a total of 180 separate SFE measurements are made for the random case, the SRO case with a full slip of 0 dislocations, and the SRO case with a full slip of 3 dislocations (which was found to be enough to fully disorder the plane, i.e., produce a near zero correlation for atoms across the slip plane). For each group of atoms, the total energy of that group is measured before and after the shift and divided by 1/18 of the area of the xy-plane of the supercell.

Results

A cumulative DAPB formation energy per unit area is calculated as:

$$E^{DAPB}(N) = \sum_{n=1}^{N} \gamma_n^{DAPB} = \frac{E_n - E_0}{A} \tag{4.11}$$

where γ_n^{DAPB} is given by Eq. 4.1 and N is total number of slips undergone in the slip plane. Similar to Eq. 4.1, E_n is the total energy of the system after the glide of n dislocations in the same glide plane (E_0 being the reference total energy). The values of $E^{DAPB}(N)$ and τ_n^{DAPB} are plotted as a function of number of slips n in Fig. 4.4. Most of the strengthening is associated with passage of the first dislocation, with a value of $\tau_1^{DAPB} = 85.6$ MPa. This strengthening is associated with a DAPB energy of $\gamma_1^{DAPB} = 21.3$ mJ/m^2. The values of τ_n^{DAPB} decrease monotonically with $n = 2$ and 3 as the values of γ_n^{DAPB} decrease with subsequent slips. After the third slip, the magnitude of τ_n^{DAPB} becomes negligible, and the slip plane can be considered completely disordered. Therefore, for later sections that involve the presence of a DAPB, we take the case of a DAPB formed by 3 slips to mimic a completely disordered plane unless stated otherwise.

The value of the DAPB energy reported here is characteristic of the range of values reported in previous simulations of other concentrated FCC solid solutions [92, 110, 109]. This is also characteristic of experimental measurements of a γ phase of a Ni-based superalloy (largely containing Ni and Cr) homogenized at 1123 K [134]. Through the consideration of friction forces and elastic interactions of dislocations in a pileup from an in-situ deformation experiment at room temperature, values of γ_1^{DAPB} in this alloy were found to be in the range of 20-35 mJ/m^2. Therefore, the calculated DAPB energies in this study are representative of realistic values that would be found in technologically relevant FCC solid solution alloys.

The SFE was also measured as a function of number of slips according to Eq. 4.3. The SFE is plotted as a function of slip number for the sample with SRO in Fig. 4.5(a), along with the corresponding average value of the SFE for a random solid solution with the same composition. In the sample with SRO the SFE changes its value as a function of the number of slips (n), starting from a value of 108.6 mJ/m^2 and dropping to a value near that of the random case (95.1 mJ/m^2) after 3 slips. A similar decrease in SFE is shown in Ref. [109]. There is a slight offset between the random and large-n values of the SFE for the sample with SRO. This is likely due to correlations in the occupancies of the atoms in the adjacent planes rather than a sampling error.

A distribution of SFE is calculated sampling ”ribbon-shaped” areas on the order of the dislocation spread as described in the previous section. The histograms and Gaussian distributions fit to these histograms are shown in Fig. 4.5(b) for three cases: (i) a plane in a material with SRO with no previous slip, (ii) for a plane that has already slipped 3 times, and (iii) for a material with random substitutional disorder. Similar to Refs. [96, 109], the SFE has a higher average and a narrower distribution in the SRO state with no previous slips compared to the disordered state. However, when the ordering is destroyed on the slip

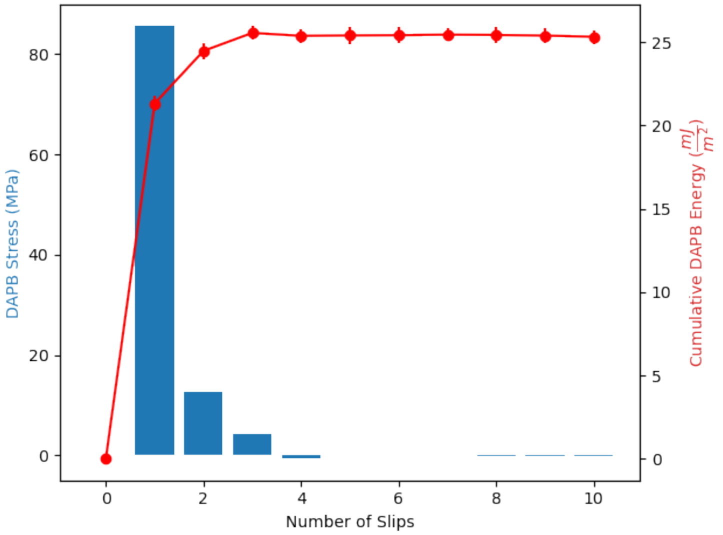

Figure 4.4: The cumulative DAPB energy $E^{DAPB}(N)$ (red circles connected by solid lines) and strengthening τ_n^{DAPB} (blue bars) as a function of the number of slips (n) on a glide plane. The values of $E^{DAPB}(N)$ are given by the right vertical axis, while those for τ_n^{DAPB} are given on the left. The error bars on the symbols for $E^{DAPB}(N)$ correspond to the standard deviation of the distribution in calculated values.

plane by three dislocation slips, both the average and the standard deviation nears that of the random alloy. The features of these distributions, along with the values of SFE and DAPB formation energy will be important in interpreting features of the cross-slip energy barriers discussed in the next section, as these provide insights into the relative differences in final and initial state energies during the cross-slip process.

4.5 Cross-Slip Activation Barriers

Methods

In order to investigate the effect of SRO on energy barriers for cross-slip, a procedure is used similar to that employed by Nöhring and Curtin [98, 99]. A distribution of energy barriers are calculated through the use of the climbing-image nudged-elastic band (CI-NEB) method [31, 33] with a total of 32 images. In order to set up the initial and final states (a dislocation dissociated in the glide plane or in the cross-slip plane, respectively) for the CI-NEB method, an average atom potential is constructed for Ni-10%Al following Ref. [27]. A 738,720 atom FCC cell, with the orientation and lengths similar to that mentioned above, is constructed at the equilibrium lattice constant of the average atom potential. A screw

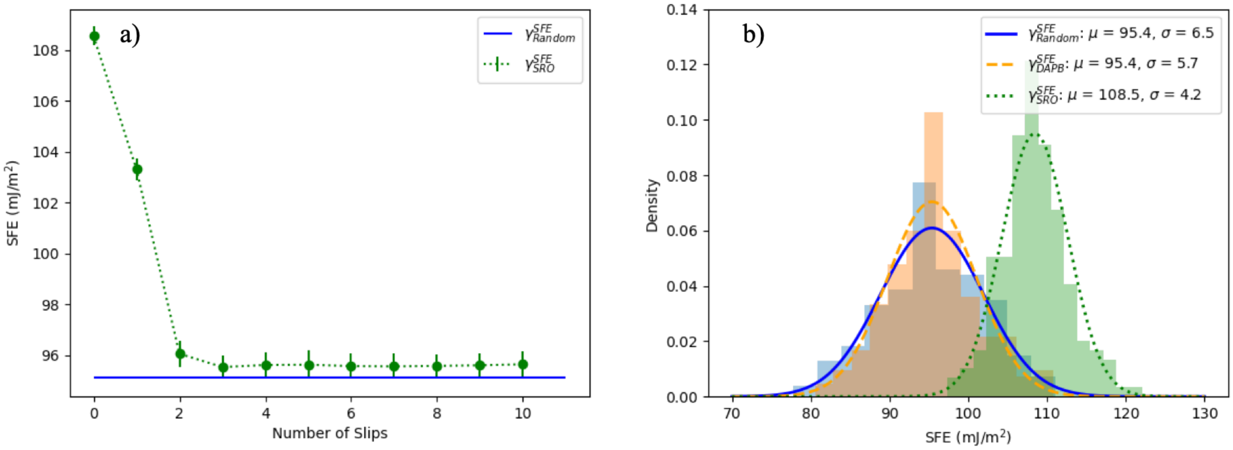

Figure 4.5: a) The SFE as a function of slip for a sample with SRO (green symbols connected by dotted lines) and for a sample with random substitutional disorder (solid blue line, with values that are independent of slip number). The error bars on the solid symbols represent one standard deviation for the distribution of calculated values. b) The distribution of SFE values for the SRO and disordered case, calculated from thin ribbon cross sectional areas, as described in the text. Bars represent histograms of calculations and solid lines represent a Gaussian distribution fit to the corresponding histogram data.

dislocation is inserted along the x-direction centered in the yz-plane of the cell using the displacements from anisotropic elasticity as given by the ATOMSK software [135]. Atoms within a cylinder of radius $40b$ from the center of the yz plane were allowed to relax, while those in the rest of the cell (which had a thickness of at least twice the EAM potential cutoff from the surface as well as a dislocation line length of $60b$) was fixed to the elasticity solution. The dislocation would dissociate on the glide or cross-slip plane depending on whether or not the center of the initial elasticity solution was varied by a few fractions of an angstrom [98].

Subsequently, 400 FCC supercells (without the dislocation) were initialized with either a random distribution of Al or a SRO distribution from hybrid MC/MD at 700 K. The template from the relaxed average-atom dislocation containing supercell described in the previous paragraph was then populated with each of these distributions and the atomic cylinder is relaxed (sometimes with an introduction of a specific DAPB configuration through a rigid displacement of sections of the supercell, mentioned in the following section and illustrated in the Supplementary Material document for this chapter) with a force convergence of 0.001 eV/$\mathring{A}$ after scaling to the correct lattice constant. This can be done as the difference between elastic constants of the average atom potential, true random case, and SRO case is small (see Table 4.1). If the dislocation core's position (which is tracked using common neighbor analysis [78]) after relaxation varied more than the distance between (112) planes (or $\sqrt{3}b/2$),

State	C_{11} (GPa)	C_{12} (GPa)	C_{44} (GPa)	a (Å)
AA	225.5	151.0	125.1	3.529
TR	219.6	152.0	125.1	3.5273
SRO	224.4	153.2	126.2	3.5235

Table 4.1: Calculated zero-temperature elastic constants and lattice constants for Ni-10%Al for the average atom potential (AA) [27], the true random (TR) alloy configuration, and an alloy sample with SRO equilibrated at 700K. Results are derived from the EAM potential of Ref. [80].

then the initial state is discarded. If the dislocation is not centered during relaxation, which can occur due to a competition of dislocation line tension and local energetic minima from solutes, its position will be inconsistent with the fixed boundary conditions derived by assuming the dislocation is centered within the cylinder. This off-centering of the dislocation will also lead to extra contributions to the energy barrier during CI-NEB. For all cases, at least 85 states satisfied the condition of remaining centered. Note that in these CI-NEB calculations, there is no consideration of the effect of the local lattice expansion due to the formation of a DAPB. This effect was found to be negligible, as shown in the Supplementary Material document for this chapter.

After setting up the initial dislocation configurations, CI-NEB calculations are run with those initial states (dissociation in the glide plane) and their respective final states (dissociation in the cross-slip plane) to obtain a distribution of cross-slip energy barriers. Fig. 4.6 shows representative configurations in the initial, transition, and final states. In the CI-NEB calculations, we made use of a force tolerance of 0.001 eV/$\AA$. A convergence study was done with respect to the cylindrical radius as well as the dislocation length for the cross-slip barrier of the average atom potential (as described in ref. [27]), and the given supercell size was found to be a good representation of the barriers with respect to larger sizes (within 20 meV of the largest radius and within 15 meV of the largest length investigated in the Supplementary Material document for this chapter). For the average atom potential case, the cross-slip barrier was found to be 1.803 eV, and the difference between the final and initial state energy is less than 0.003 eV. In certain cases (with more detail given in the following sections), ATOMSK is used to modify the elasticity boundary conditions to add in the effect of an applied external stress.

Cross-Slip in a Random Alloy

100 samples were used to calculate the energy barriers for cross-slip for a random alloy. For this case, on average there is no DAPB, so all of the situations in Fig. 4.1 are, on average, identical. The data, shown in blue in Fig. 4.7, represents the distribution of the calculated energy barriers for cross-slip, which was fit to a gamma distribution [136], where the form

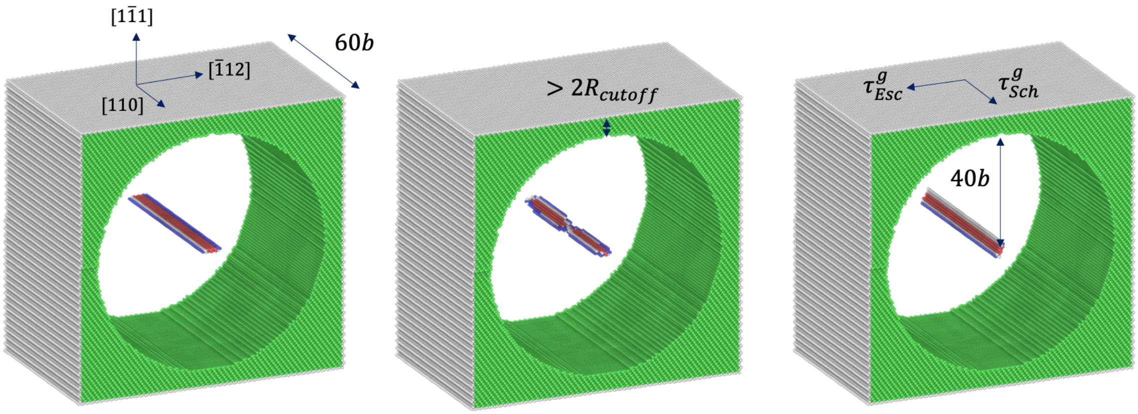

Initial State Transition State Final State

Figure 4.6: The above shows the simulation supercell set-up for CI-NEB calculations of cross-slip in an average-atom Ni-10%Al alloy. Displayed are the atoms in the boundary regions fixed to the solutions of anisotropic elasticity for a screw dislocation located in the center of the cylinder, as well as those atoms within the dislocation core. Atoms are colored according to the common neighbor analysis scheme [78] as implemented in OVITO [77].

of the probability distribution function (PDF) is given by:

$$f(E_A, k, \theta) = \frac{1}{\Gamma(k)\theta^k} E_A^{k-1} \exp\left(\frac{-E_A}{\theta}\right) \tag{4.12}$$

where k and θ are parameters, and $\Gamma(k)$ is the gamma function. The parameters of k and θ were determined through the Maximum Likelihood Estimate (MLE). A gamma distribution is chosen as opposed to a Gaussian distribution to avoid a non-zero probability for a negative energy barrier for cross-slip, which would not be physical. This distribution form was shown to fit the data well, as shown in the probability-probability plots in the Supplementary Material document for this chapter. The average and standard deviation for the data were 1.895 eV and 0.645 eV, respectively. The measured average cross-slip energy barrier for the random case is slightly larger than that from the average atom potential due to the consideration of explicit solutes.

Cross-Slip Between DAPBs

The cross-slip energy barriers were calculated for two cases in which the slip planes included DAPBs formed by 3 consecutive slips, so γ_n^{DAPB} is negligible. The first, which we will refer to as between "full DAPBs" involves cross slip between two slip planes with fully formed DAPBs in front and behind the dislocation (see Fig. 4.1(e)). The second, which we will refer to as between two "half DAPBs" involves a DAPB behind the dislocation in

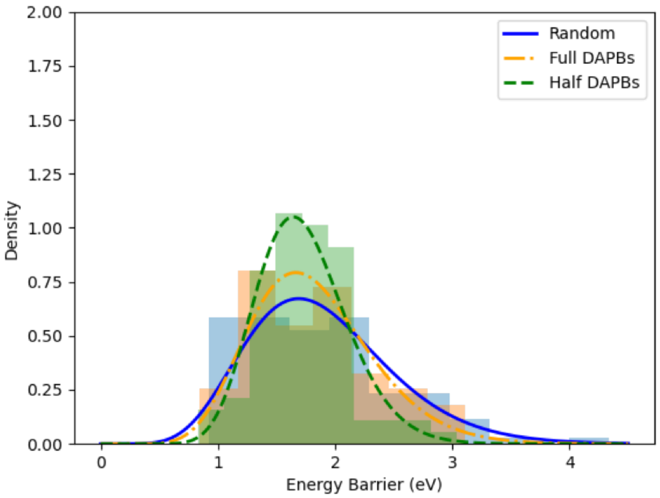

Figure 4.7: The distribution of cross-slip energy barriers for the random (blue) case with a mean of 1.895 eV, for the case of cross-slip between two planes with full DAPBs (orange) like that in Fig. 4.1(e) with a mean of 1.815 eV, and the case of cross-slip between two half DAPBs (green) like that in Fig. 4.1(c) with a mean of 1.730 eV. Histograms from the simulation data are plotted with bars and the solid lines represent fits of these histograms to gamma distributions.

the slip plane, and in front of the dislocation in the cross-slip plane (Fig. 4.1(c)); such a configuration in an alloy would be generated through multiple cross-slip events at the same site. 85 energy barriers were computed for each of these two scenarios. For the case of two half DAPBs, a Schmid stress had to be applied in the glide plane in order to counteract the force arising from a dislocation being partially dissociated into a region of SRO (the dislocation will have a lower energy per unit length if it is dissociated in a DAPB). The trailing partial will be located in a DAPB region and the leading partial will be located in a SRO region, so the force due to the SFE acting on each partial will be different (Fig. 4.5(a)). The force balance on each partial (Fig. 4.8) leads to Eq. 4.4 for the leading partial, and the following for the trailing partial:

$$\frac{K_{int}}{r_g} = \gamma_3^{SFE} + \frac{\tau_{sch}^g b}{2} \tag{4.13}$$

In order to have Eqs. 4.4 and 4.13 equal each other, the Schmid stress in the glide plane ($\tau_{sch}^g = \tau_{xz}$ for our system) must equal:

$$\tau_{xz} = \frac{\gamma_0^{SFE} - \gamma_3^{SFE}}{b} \tag{4.14}$$

$$\tau_{xy} = \frac{\tau_{xz}}{2\sqrt{2}} \tag{4.15}$$

where the second stress (Eq. 4.15) is applied in order to remove Schmid stress projected onto the cross-slip plane due to the first stress (Eq. 4.14). From the previous section, we use 108.6 mJ/m^{2}for γ_0^{SFE} and 95.5 mJ/m^2 for γ_3^{SFE}.

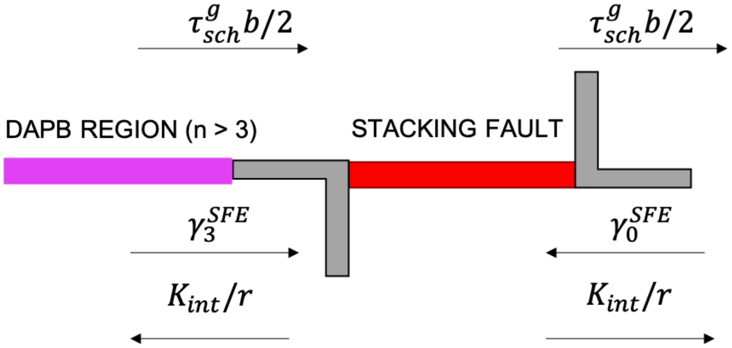

Figure 4.8: The forces present on each partial dislocation for the case of a dislocation in the glide plane cross-slipping between two half DAPBs.

The resulting energy barrier distributions for cross-slip between full DAPBs and between half DAPBs are shown in the orange and green curves in Fig. 4.7. The between full DAPBs environment has an average activation energy of 1.815 eV and a standard deviation of 0.525 eV, while the between two half DAPBs environment has an average activation energy of 1.730 eV and a standard deviation of 0.387 eV (with the applied Schmid stress to keep the initial state centered). The lower average activation energy for the case of between two half DAPBs can be rationalized by the fact that the dislocation in the cross-slip state can reduce its energy relative to the initial state by fully dissociating in the DAPB instead of partially dissociating in the DAPB and a region of unbroken order. The lower SFE in the DAPB means that their is a slightly lower elastic interaction between the partial dislocations. So while this case is likely not truly as symmetric (on average) in energy as implied by Fig. 4.1(c), the asymmetry here is not a hindrance for cross-slip. As we will see in the following sections, the absence of a DAPB in the cross-slip plane makes cross-slip substantially more difficult.

Cross-Slip at the Head of a Planar Array

The three cross-slip scenarios described in the previous two subsections dealt with transitions where the dislocations in the initial and final states were dissociated in a similar environment when in the glide plane or in the cross-slip plane. This will not be the case for the cross-slip of a screw dislocation at the head of a planar array in a material with SRO. We thus turn next to this case, illustrated in Fig. 4.1(b) and discussed in Section 4.2. In the initial state, the dislocation cut behind the screw dislocation will leave behind a DAPB of 1 slip, which creates a driving force on the screw dislocation to move in a direction to restore the SRO. In order to counter this effect, a Schmid stress state is applied similar to that defined in Eqs. 4.14 and 4.15 above, with the difference being in setting τ_{xz} equal to τ_1^{DAPB} through the use of Eqs. 4.4-4.6.

The distribution of cross-slip energy barriers for the forward and backward (or reverse) transitions in this case, each derived from 85 samples, is shown in Fig. 4.9(a). If the initial and final states were equivalent in energy, then the distributions should fall on top of each other. Instead, there is an average difference in energy where the initial state is 0.602 eV (0.010 eV/b) lower than the final state. This value expressed per Burgers vector is important, as it takes into account the fact that these simulations are only considering a periodic dislocation segment with a length of 60b. For an infinitely long dislocation in this situation, cross-slip will be an uphill in energy process due to increasing the system energy by 0.010 eV/b through dissociating the dislocation in the cross-slip plane. So unless a sufficient value of the stress is applied to compensate for this energy difference, cross-slip will not be activated. We choose to focus on the effect of an Escaig stress in the original glide plane which brings the partials closer together, thereby increasing the elastic interaction energy in the initial state. In this case, γ_g from Eq. 4.8 becomes $\gamma_0^{SFE} - \gamma_1^{DAPB}/2 + b\tau_{esc}/(2\sqrt{3})$, as the Escaig stress acts to increase the effective SFE. To find the minimum Escaig stress in the glide plane needed to compensate for the energy difference in the final and initial states, Eq. 4.8 is inserted into Eq. 4.7 (neglecting other stresses), and is rearranged to give:

$$\tau_{esc}^{crit} = \frac{\sqrt{3}\gamma_1^{DAPB}}{b} \tag{4.16}$$

which, when solved for τ_{esc}^{crit}, gives the minimum Escaig stress needed in the glide plane for cross-slip to cease being an uphill in energy process for the head of a planar slip array.

Given γ_1^{DAPB} as 21.3 mJ/m^2, the resulting τ_{esc}^{crit} is 148.1 MPa. This means that the simulation cell will need to have the following stresses applied [117]:

$$\tau_{yz} = -\tau_{esc}^{crit} \tag{4.17}$$

$$\tau_{yy} = -\tau_{zz} = \frac{7}{4\sqrt{2}}\tau_{esc}^{crit} \tag{4.18}$$

where the sign of τ_{yz} is chosen to bring the partial dislocations closer together, and τ_{yy} and τ_{zz} are chosen to make sure that there is a net zero Escaig stress in the cross-slip plane.

The stresses in Eqs. 4.17 and 4.18 are added to the Schmid stress state to ensure the dislocation is centered in its initial state. The cross-slip energy barrier distributions calculated using 85 samples, with these applied stresses, are shown in Fig. 4.9(b). In comparison to Fig. 4.9(a), it is evident that the application of the Escaig stress in the glide plane not only brings the peaks closer together, but it also creates a greater overlap between the two distributions than without the Escaig stress. With the Escaig stress, the initial state is now on average 0.275 eV (0.005 eV/b) higher in energy than the final state. This represents some

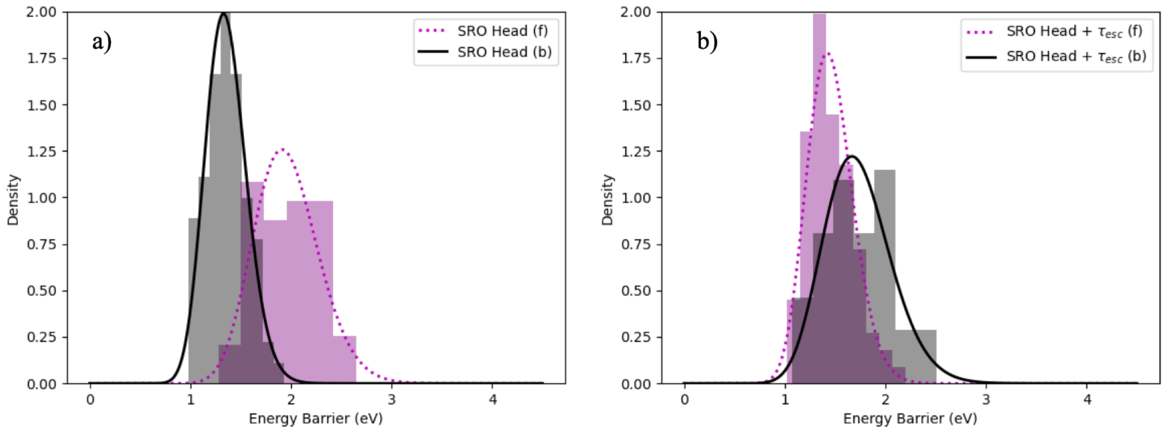

Figure 4.9: The distribution of cross-slip barriers for the head of a planar slip array (Fig. 4.1(b)) during the forward (purple) and backward (black) transition. a) represents the distributions without an applied Escaig stress in the glide plane (with means of 1.96 eV and 1.36 eV for the forward and backward transitions, respectively), while b) represents the distributions with an applied Escaig stress of 148.1 MPa in the glide plane (with means of 1.46 eV and 1.73 eV for the forward and backward transitions, respectively).

overshoot in the estimate of the additional stresses calculated above, to make the initial and final states equal in energy. This overshoot likely results in part from the use of the Volterra fields of the partials which could be corrected by considering more complex interactions that are important at small partial dislocation separation distances [137]. The strength of this contribution is evidenced in the Supplementary Material document for this chapter, where predicted dissociation distances from the consideration of the Volterra fields are found to be lower than the measured dissociation distances in the simulation cells. There is also no consideration of solute pinning on partial dislocation motion, but this effect would increase the stress required. However, the simple estimate given by Eq. 4.16 still achieves the goal of making cross-slip a downhill-in-energy process. We also note that by using Eq. 4.8 without any applied stress results in an estimated energy difference between final and initial state of 0.679 eV (0.011 eV/b), in good agreement with the observed differences from the CI-NEB calculations.

Cross-Slip Out of a DAPB

A last scenario was investigated (corresponding to Fig. 4.1 (d)) in which a DAPB (due to 3 full slips) was created only in the glide plane, and cross-slip occurs to a plane with undisturbed SRO. 85 cross-slip barriers were calculated for cross-slip out of the DAPB, and the reverse process into the DAPB. The resulting distributions are given in Fig. 4.10, along with the distributions from Fig. 4.9 (a). For the case considered in this section of cross-slip out of a DAPB, the average difference in energy between the final state and the initial state is 0.780 eV (0.013 eV/b). As mentioned in Section 4.2, this difference in energy comes from the difference in elastic interaction energy of partial dislocations in the final and initial state. This effect originates from an average difference in SFE in the DAPB versus in the region of the materials with SRO, which is previously calculated to be 95.5 mJ/m^2 and 108.6 mJ/m^2, respectively. Inserting these values as γ_g and γ_{cs} in Eq. 4.8, as well as evaluating K_{int} with calculated elastic constants following [48, 99] and multiplying times the dislocation length, results in a difference in energy of 0.845 eV (0.014 eV/b), in very reasonable agreement with the observed average difference from the CI-NEB calculations. Similar to the case discussed in the previous subsection we can estimate an Escaig stress required to make the initial and final states equal in energy. We take γ_g to be equal to $\gamma^{SFE}_{n\to\infty} + b\tau_{esc}/2\sqrt{3}$. Following a similar analysis as that presented in the previous subsection, the minimum Escaig stress needed in the glide plane to suppress this effect is:

$$\tau^{crit}_{esc} = \frac{2\sqrt{3}(\gamma^{SFE}_0 - \gamma^{SFE}_{n\to\infty})}{b} \tag{4.19}$$

In order to activate this event, a larger stress (182.1 MPa, obtained from Eq. 4.19) would be required compared to that needed at the head of the planar array.

Summary of Distribution Parameters

Table 4.2 below summarizes the gamma distribution parameters (k and θ, as defined in Eq. 4.12), mean (μ defined from the average of the histograms), and standard deviation (σ, defined also from the histograms) for all of the cross-slip activation energy barriers discussed in the previous section. The values in parentheses represent standard errors for these parameters estimated through bootstrapping 100,000 independent samples for each data set (k and θ errors were estimated from the distribution of these parameters through separate MLE fits to Eq. 4.12 for each bootstrapped sample) [138]. These standard errors are given as a measure of statistical significance associated with results in this study associated with the means and standard deviations of the cross-slip energy barrier distributions. Note that the order in which the standard deviation of cross-slip barriers decrease (for cases where the dislocation is fully dissociated across one environment: Random, Full DAPBs, Out of DAPB, SRO Head), follows the order in which the standard deviation of local SFE decreases (Random, DAPB, SRO). While the distribution of local SFE plays a significant role in the distribution of cross-slip barriers as it is connected to the distribution of difference in end-state energies, this quantity only samples local changes in solute-solute interaction [139]. A full understanding of the spread in the distribution of the cross-slip energy barriers would require understanding how both the solute-solute interactions change as well as how the solute-dislocation interaction changes during cross-slip [98, 99]. This latter term was found to be significant for the random case of the system being studied here [98]. This term should

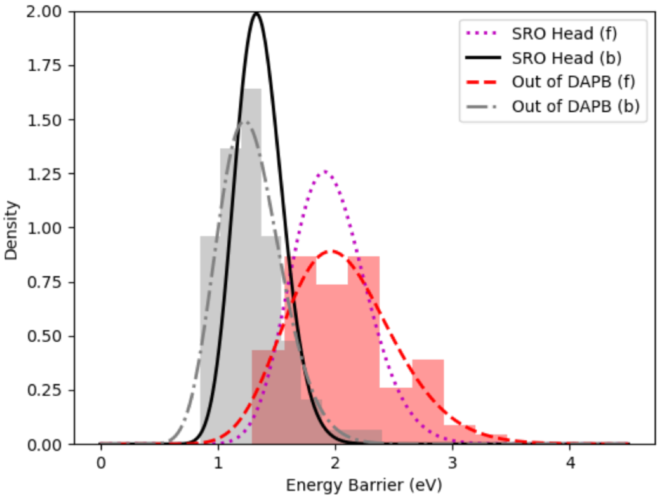

Figure 4.10: The forward (red) and backward (gray) cross-slip energy barrier distributions for a dislocation cross-slipping out of a DAPB (Fig. 4.1(d)) with means of 2.07 eV and 1.29 eV, respectively. Black and purple curves correspond to the analogous energy barriers for the SRO head case, and are reproduced from Fig. 4.9(a) for comparison. The values of τ_{esc}^{crit} needed to make the SRO Head and Out of DAPB cross-slip a downhill-in-energy process are 148.1 MPa and 182.1 MPa, respectively.

be expected to decrease with an increase in SRO [140, 110], following the same trend as the decrease in standard deviation of SFE with an increase in SRO.

4.6 Discussion

Internal Stress at the Head of a Planar Slip Array

In analyzing the effects of stress on cross-slip thus far, we have neglected the effect of a projected Schmid stress onto the cross-slip plane. This is due to the fact that the boundary conditions of our simulations would not be able to properly account for bow-out in the cross-slip plane in the transition state, requiring us purposefully cancel out any projected Schmid stress contribution onto the cross-slip plane. As such, the configurations we sampled for the results presented in the previous sections (reproduced for the case of cross-slip at the head of a planar slip array in Fig. 4.11(a)) will not be representative of every general cross-slip configuration (an alternative example given in Fig. 4.11(b)). Note that this does not diminish the main result of this study, which is that the effect of chemical redistribution due to SRO fundamentally changes the energetics involved during cross-slip compared to the

Cross-Slip Environment	k	θ	μ (eV)	σ (eV)
Random	9(1)	0.20(3)	1.90(6)	0.65(5)
Full DAPBs [Fig. 4.1(e)]	12(2)	0.15(2)	1.82(6)	0.53(4)
Half DAPBs [Fig. 4.1(c)]	20(4)	0.09(2)	1.73(4)	0.39(4)
Out of DAPB (f) [Fig. 4.1(d)]	20(3)	0.10(1)	2.07(5)	0.47(3)
Out of DAPB (b) [Fig. 4.1(d)]	22(4)	0.06(1)	1.29(3)	0.29(3)
SRO Head (f) [Fig. 4.1(b)]	37(5)	0.052(6)	1.96(3)	0.32(2)
SRO Head (b) [Fig. 4.1(b)]	45(6)	0.030(4)	1.36(2)	0.20(1)
SRO Head + τ_{esc} (f) [Fig. 4.1(b)]	41(6)	0.035(5)	1.46(3)	0.23(2)
SRO Head + τ_{esc} (b) [Fig. 4.1(b)]	27(4)	0.064(8)	1.73(4)	0.33(2)

Table 4.2: Distribution parameters for cross-slip energy barriers in different solute environments. (f) is for the barriers in the forward direction, while (b) is for the barriers in the backward direction. Values in parentheses represent estimates of the standard error on the last reported significant figure of the various parameters obtained through bootstrapping.

random case, regardless of the consideration of a projected Schmid stress in the cross-slip plane. However, we can still make an estimate of its effects.

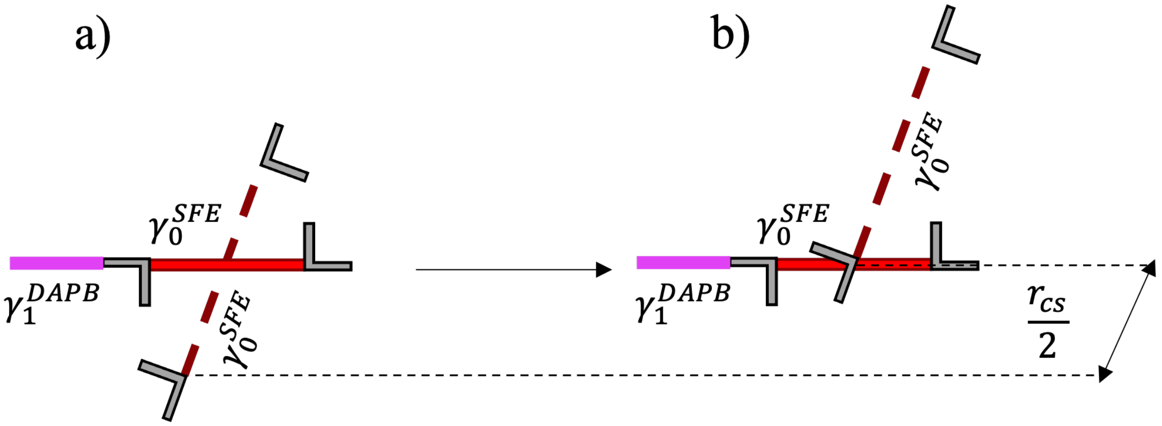

Figure 4.11: a) Cross-slip for the case in Fig. 4.1(b) neglecting the effect of a projected Schmid stress on the cross-slip plane. b) Cross-slip for the case in Fig. 4.1(b) including the effect of a projected Schmid stress (less than τ_1^{DAPB}) on the cross-slip plane.

Firstly, we consider the case where the maximally resolved shear stress is in the glide plane and ask what magnitude of a Schmid stress in this plane would be needed in order for a screw dislocation in the cross-slip plane to be able to form a DAPB. In order for the Schmid stress in the cross-slip plane to be larger than τ_1^{DAPB} (or 85.6 MPa for the system considered in this study), the Schmid stress in the glide plane has to be three times as large[2], which comes out to be 256.8 MPa. Before this stress threshold is reached, the screw dislocation will not continuously glide in the cross-slip plane, and there will not be significant bow-out in this plane. This is a lower bound for the stress needed to cause a significant bow-out effect, as the contribution of the dislocation line tension will act against the bow-out configuration.

Secondly, the projected Schmid stress, even if it does not cause the screw dislocation to glide in the cross-slip plane, can still contribute to decreasing the energy difference between the final and initial cross-slip states. As long as the Schmid stress in the cross-slip plane is lower than the stress required to move a screw dislocation in that plane, the screw dislocation can move a total distance of $r_{cs}/2$ (or half the dissociation distance) in the cross-slip plane in response to the stress before forming a DAPB (Fig. 4.11(b)). The difference between the final and initial state energies per unit length in this scenario would then be equal to:

$$-K_{int}\left(\ln\frac{\gamma_g}{\gamma_{cs}}+\frac{\tau^g_{sch}b}{6\gamma_{cs}}\right) \tag{4.20}$$

The first term in Eq. 4.20 comes from Eq. 4.8, and the second term is the work done on the system due to the Schmid stress on the glide plane projected onto the cross-slip plane. Setting Eq. 4.20 to zero (with no Escaig stress applied) results in τ^g_{sch} equal to 270.2 MPa, which is larger than the stress needed for continuous glide in the cross-slip plane.

Thirdly, when considering a situation of a pile-up where the head of an array is stuck at an obstacle, the required stress to set Eq. 4.20 to zero can be even lower. In this scenario, a Schmid stress in the glide plane effectively acts as an Escaig stress [118], where:

$$\tau_{esc}=\sqrt{3}\tau^g_{sch} \tag{4.21}$$

where τ^g_{sch} represents the Schmid stress in the glide plane. This is due to the leading partial being stuck at an obstacle, so the Schmid stress in the glide plane acts on the trailing partial to reduce the dissociation distance. In order to reach the critical Escaig stress for Fig. 4.11(a) (neglecting the effect of a Schmid stress in the cross-slip plane), this would require a Schmid stress of $\tau^{crit}_{esc}/\sqrt{3}$ (in addition to the Schmid stress of τ^{DAPB}_1 to counteract the DAPB effect on the glide plane) when the head of a planar array is stuck at an obstacle. In total, this would require a Schmid stress of 171 MPa in order for an "Escaig" type effect to make cross-slip a downhill-in-energy process at the head of a planar slip array, which is less than that needed for a pure Schmid effect in the cross-slip plane. When considering the combination of this "Escaig" type effect as well as the projected Schmid stress in the cross-slip plane (and neglecting cross effects), γ_g in Eq. 4.20 can be replaced with $(\gamma^{SFE}_0-\gamma^{DAPB}_1/2+(b\tau^g_{sch}-\gamma^{DAPB}_1)/2)$, and the value of τ^g_{sch} needed for Eq. 4.20 to be equal to zero is 129 MPa.

---

[2] This comes from the fact that the two planes are tilted by 70.53° with respect to each other, so the projection of the Peach-Koehler force ($F_{PK}=\tau_{sch}b$) from the glide plane on to the cross-slip plane would be $F_{PK}\cos(70.53^\circ)=F_{PK}/3$.

We neglect the effect of projected Schmid stresses for other dislocations besides the head in a pile-up, as in this situation the majority of the Schmid stress is localized at the head of the array [86, 141]. We note that in this analysis we are considering isolated dislocations under a homogonous stress distribution, and in a real planar slip-array, especially in a pile-up, the stress distribution is likely to be heterogenous. A pile-up may also result in an "Escaig" type effect for dislocations behind the head dislocation. Nevertheless, the point of this analysis is to demonstrate that regardless of the source or type of stress, some stress is necessary to compensate for the difference in energy per unit length of the final and initial state during cross-slip in an SRO material, an effect that is absent in an alloy with completely random configurational disorder. To be consistent with atomistic results presented earlier, the remainder of the discussion will not consider the effect of a projected Schmid stress in the cross-slip plane.

The Effect of Fluctuations

While the analysis of Section 4.2 predicts the change in the average difference in energy in the cross-slip plane and the glide plane, an alloy with some distribution of solutes, random or SRO, will have a distribution of cross-slip barriers with fluctuations deviating from the mean. In particular, Ref. [120] found that cross-slip in a concentrated FCC solid solution alloy occurred at an activation barrier much smaller than that predicted by elasticity theory, and Refs. [98, 99] found that random FCC solid solution alloys have a distribution of cross-slip energy barriers with significant deviations from the mean. The probability of a successful cross-slip attempt can be represented as:

$$P_{CS} = \int_0^\infty \exp\left(\frac{-E_A}{k_B T}\right) f(E_A, l, \tau)\, dE_A \tag{4.22}$$

where $f(E_A, l, \tau)$ is the PDF of cross-slip energies (E_A) dependent on the dislocation length (l) and applied stress (τ), k_B is the Boltzmann constant, and T is the absolute temperature. It is clear from Eq. 4.22 that the dominating contribution to the cross-slip probability will be from the energy barriers lower than the mean as this will cause the exponential term in the integral to have a much higher weight than larger energy barriers. This will still be true for an alloy with SRO, even though it is natural to expect that the standard deviation in this case will be lower than the random case [99], which will certainly contribute to a decreased cross-slip probability compared to the random case.

However, in a material with SRO, the effect of an increase in system energy per dislocation line length (especially for the cases of cross-slip at the head of a planar slip array and cross-slip out of a DAPB) will be dominant. This can be shown through the following analysis. The standard deviation of a cross-slip activation energy distribution in a random FCC alloy has been shown to scale with the square-root of the dislocation line length [98, 99]. While the standard deviation for an SRO material would likely not follow the exact same scaling as the random alloy, it can be used as an upper bound estimate.

An estimation for the change in the mean ± one standard deviation for the forward barriers (E_A^f) as a function of dislocation length can be made with:

$$E_A^f = E_A^b + lE_{diff} \pm \sigma_{cs}\sqrt{l} \tag{4.23}$$

where E_A^b is the average value of the backwards energy barrier (this is a length independent quantity as this requires the creation of a cross-slip nucleus which will reduce the energy of the system when expanding along the dislocation line) , E_{diff} is the average difference in energy per unit length (b) between the final and initial state, and σ_{cs} is the standard deviation of the forward cross-slip energy barrier per $\sqrt{b}$ (obtained from dividing the standard deviation from the NEB calculations by $\sqrt{60}$). For the case of cross-slip at the head of a planar slip array, E_A^b is 1.36 eV, E_{diff} is 0.010 eV/b, and σ_{cs} is 0.041 eV/$\sqrt{b}$. For the case of cross-slip out of a DAPB, E_A^b is 1.29 eV, E_{diff} is 0.011 eV/b, and σ_{cs} is 0.061 eV/$\sqrt{b}$. These values are then used with Eq. 4.23 to plot the estimated mean ± one standard deviation for these cases as a function of dislocation length in Fig. 4.12. A dislocation length may be related to a characteristic dislocation density through $l = 1/\sqrt{\rho}$, where ρ is the dislocation line density per unit volume. As is clear in Fig. 4.12, especially with dislocation lengths representing realistic dislocation densities of 10^{11}-10^{15} m^2, the spread of barriers across ± one standard deviation covers at most around 10-20 eV, while the average barrier quickly increases to values much larger than the spread. The values of these energy barriers are quite large, so much so that cross-slip is not expected occur in these cases without the aid of stress, even considering the effect of fluctuations. This is once again due to the effect of an increased elastic interaction of partial dislocations in the cross-slip plane, something that will not be present in a random solid solution alloy. In the previous subsection, we made estimates for the role of an applied Schmid stress suppressing E_{diff}. Until stresses greater than or equal to these are reached, the cross-slip barrier will continue to be a monotonic function of dislocation length. We believe that these considerations may be an important factor in understanding why recent discrete dislocation dynamics simulations of concentrated alloys were not able to reproduce general deformation behavior of these alloys, such as planar slip, when considering a purely random distribution of cross-slip energies [19].

The previous analysis focuses on consideration of the cross-slip of an entire dislocation, when in reality there could be limited regions of the dislocation that cross-slip. However, even in this picture it is expected that cross-slip is hindered in an alloy with SRO when compared to the random case. Additionally, in the random case a weakest-link regime for cross-slip can be achieved when large enough stresses suppress the majority of high activation energy barriers present in the cross-slip barrier distribution [99]. We expect that this regime will tend to be shifted to higher stresses for the SRO case, as the high energy barriers from the random alloy are reflected by the standard deviation in the distribution (which scales with $\sqrt{l}$) while the high energy barriers for the SRO case are largely due to the average difference in end state energies (which scales with l).

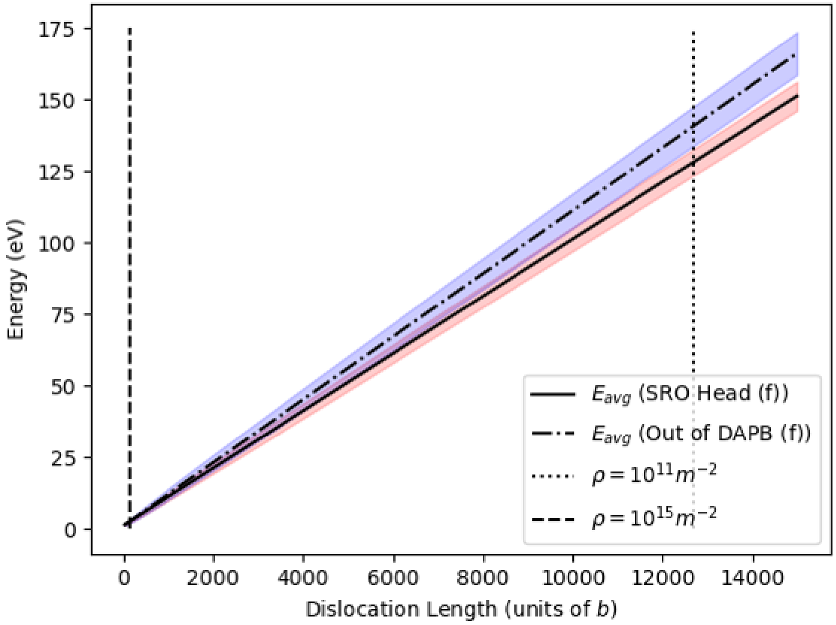

Figure 4.12: Change in the forward cross-slip energy barrier with increasing length. The shaded areas represent ± one standard deviation from the mean.

Correlated Cross-Slip

An analysis of the results given in Fig. 4.10 and Fig. 4.12 shows that the stress required to make cross-slip a downhill-in-energy process for dislocations behind the head of a planar array (i.e. the case of cross-slip out of a DAPB) is larger in the system considered here with SRO than the stress needed for cross-slip at the head of an array to become a downhill-in-energy process. While it is difficult to tell if this will hold for any system exhibiting SRO, it seems reasonable to assume that the two cases will require comparable stresses. Given that the stress of a planar slip pile-up is largely concentrated at the head of an array [86, 141, 48], it is unlikely that cross-slip will occur behind the head of a planar slip array without the aid of a DAPB formed by a lead dislocation that has already cross-slipped (Fig. 4.1(c)), or dislocation glide on the cross-slip plane belonging to another dislocation array (Fig. 4.1(e)), or without the aid of an externally applied Escaig stress. This should be especially true for dislocations of longer length, where there will be limited availability of lower-energy barriers based on the analysis of fluctuations in the previous section. Thus, it is expected that the more pronounced the SRO in an FCC alloy, the more correlated cross-slip should appear, as dislocations following the head will be able to access low energy barriers for cross-slip only if there is the presence of a DAPB in the cross-slip plane. As such, it would also be more likely that if the head of an array undergoes a double cross-slip event, the rest of the array would be more likely to follow the same path in a material with SRO, relative to a material with random configurational disorder. Such an occurrence could lead to the formation of a large amount of dislocation debris [13, 101], which can lead to further work-hardening of the material. In this context, we note that Jackson [13] cites that debris in the form of dislocation structures are observed to be more regular in Cu-Al, brass, stainless steel, Cu_3Au, and Ni_3Fe (the last two in their solid-solution state) than in pure FCC metals. All of these alloys have been found to exhibit SRO [132, 129, 142, 127, 87], which qualitatively supports the connection between SRO and correlated cross-slip. This connection as well as the results of our study justifies further investigation of SRO and the presence of a DAPB on double cross-slip processes [143] and debris formation [144] in FCC alloys.

Of course, the discussion in this section is based on atomistic results and an idealized scenario where an obstacle is present at the head of a planar slip array. In a real material with complex dislocation configurations, different scenarios could occur which may induce dislocation debris and dipolar structures as mentioned in Ref. [13]. Mesoscale models such as discrete dislocation dynamics would be better suited to investigate effects of SRO on dislocation morphology, however these models would need to be paramaterized by atomistic simulation results such as those presented here.

Impact on Dynamic Recovery

In this section we consider how the effect of SRO on cross-slip may affect dynamic recovery in FCC concentrated solid solutions. The presence of SRO on its own should increase the friction stress for glide for a pure screw dislocation. Considering that a higher friction should result in a lower characteristic dislocation annihilation distance [145], this alone may have an important impact on reducing dynamic recovery in materials with SRO. However, we also expect the change in cross-slip energy barrier distribution to have an effect.

To analyze this effect, we extend an analysis presented by Hamdi and Asgari [146]. In their work, they consider the effect of SRO on the probability of cross-slip to be limited to the head of a planar slip array. As we have shown that dislocation cross-slip barriers behind the head dislocation will be dependent on the presence of a DAPB in the cross-slip plane, we extend their approach by incorporating this information in the form of conditional probabilities. This consideration as well as the change in the distribution of cross-slip barriers with SRO will be shown to have a dramatic impact on the rate of cross-slip in a planar array, thus likely impacting dynamic recovery.

Dislocation density (ρ) evolution during strain (ϵ) can be described as [147, 146]:

$$\frac{d\rho}{d\epsilon} = \frac{d\rho^{+}}{d\epsilon} - \frac{d\rho^{-}}{d\epsilon} \tag{4.24}$$

where the first term describes dislocation generation and the second term describes dislocation annihilation or dynamic recovery. At low homologous temperatures, the second term on the right-hand side in Eq. 4.24 is proportional to the cross-slip probability [146]. When considering a planar slip array of n dislocations, the average cross-slip probability per dislocation

(P_{SRO}) in a material with SRO at a given cross-slip site may be approximated as:

$$P_{SRO} = \frac{P_H}{n} + \frac{(n-1)P_F}{n} \tag{4.25}$$

where P_H is the probability that the dislocation at the head of a planar slip array undergoes cross-slip, and P_F is the probability that a following dislocation in the pile-up undergoes cross-slip. Given that the Escaig stress at the head of an array must be greater than or equal to a certain value (τ_{esc}^H, obtained from Eq. 4.16) before cross-slip can realistically occur, P_H can be expressed as:

$$P_H = P(H|\tau_{esc} \geq \tau_{esc}^H)P(\tau_{esc} \geq \tau_{esc}^H) \tag{4.26}$$

where the probability that the head of a planar slip array undergoes cross-slip ($P(H|\tau_{esc} \geq \tau_{esc}^H)$) is now conditional on the probability that the Escaig stress is at least equal to τ_{esc}^H ($P(\tau_{esc} \geq \tau_{esc}^H)$). For subsequent dislocations, we assume that there are two contributions to the total probability of cross-slip, which are cross-slip events in the presence of a half DAPB formed by a head dislocation, and cross-slip events from a DAPB into a region of unbroken order. This can be expressed as:

$$P_F = P(F|H)P_H + P(F|\tau_{esc}^F, noH)P(\tau_{esc} \geq \tau_{esc}^F)(1 - P_H) \tag{4.27}$$

where $P(F|H)$ is the probability of a following dislocation to cross-slip conditional on the head dislocation undergoing cross-slip (P_H), and $P(F|\tau_{esc}^F, noH)$ is the probability of a following dislocation to cross-slip conditional on the presence of an Escaig stress greater than or equal to τ_{esc}^F (or the probability that the stress required to set Eq. 4.8 equal to zero is present, $P(\tau_{esc} \geq \tau_{esc}^F)$) as well as the probability that the head dislocation did not undergo cross-slip ($1 - P_H$).

To simplify, we consider a case where stress is only localized at the head of an array [86, 141, 48] such that $P(\tau_{esc} \geq \tau_{esc}^H) = 1$ and $P(\tau_{esc} \geq \tau_{esc}^F) = 0$. We also assume $P(F|H) = 1$, leading to $P_{SRO} \approx P(H|\tau_{esc} \geq \tau_{esc}^H)$. The impact of these assumptions will be discussed later. For the disordered case without SRO, all dislocations should have the same cross-slip probability $P(R)$, as there is no dependence on a DAPB. This means that the ratio of dynamic recovery in the completely disordered (i.e., random) state to that in the SRO state can be approximated by:

$$\left(\frac{d\rho^-}{d\epsilon}\right)_{rand} \Big/ \left(\frac{d\rho^-}{d\epsilon}\right)_{SRO} \approx P(R)/P(H|\tau_{esc} \geq \tau_{esc}^H) \tag{4.28}$$

The probability of a cross-slip event given a distribution of activation energy barriers can be represented by Eq. 4.22.

The starting distributions for this analysis will be those for cross-slip energy barriers calculated above for a dislocation line length of $60b$, for the random case with zero applied stress, as well as the forward barriers for the head of a SRO array with an applied Schmid stress of τ_1^{DAPB} and an applied Escaig stress of 148.1 MPa. This consideration ensures that the reference distributions are both with respect to an initially stationary dislocation as well as with respect to a cross-slip process that is on average not an uphill-in-energy process. Following the procedure outlined in Ref. [99], the effect of an applied Escaig stress in the glide plane on the average cross-slip energy barrier can be determined through elasticity theory based estimates on the change in energy due to the partial dislocation interactions as well as the change in the constriction energy. The theory requires as input only the elastic constants, stacking fault energy, and Burgers vector magnitude. As we are starting from an applied Escaig stress of 148.1 MPa for the head of an SRO array, we make the following adjustments for the work done on the partial dislocations:

$$\Delta E_{partial}(\tau_{esc} - \tau_{esc}^{crit}) = E_{ele}(\tau_{esc}) - E_{ele}(\tau_{esc}^{crit}) \tag{4.29}$$

where τ_{esc} is the effective Escaig stress due to an obstacle in front of the lead partial (Eq. 4.21), τ_{esc}^{crit} is the value from Eq. 4.16, and $E_{ele}(\tau_{esc})$ is the value from Eq. 4.8. The scaling of constriction energy (given in Eq. 13 in Ref. [99]) is adjusted for the SRO case as:

$$f_c(\gamma_g^{crit}, \gamma_g) = \frac{\gamma_g^{crit}}{\gamma_g} \frac{\ln\left((K_s - K_e/3)b/(4\pi\gamma_g)\right)}{\ln\left((K_s - K_e/3)b/(4\pi\gamma_g^{crit})\right)} \tag{4.30}$$

where the reference SFE for the glide plane has changed to γ_g^{crit} (or $\gamma_0^{SFE} - \gamma_1^{DAPB}/2 + b\tau_{esc}^{crit}/(2\sqrt{3})$), and K_s and K_e are energy prefactors of the edge and screw dislocation [48].

Using Eqs. 4.29 and 4.30, the average activation energy of the distributions considered, and assuming that the critical cross-slip nucleus size is $10b$, the effect of an effective Escaig stress on the average cross-slip energy can be found through the maximum of Eq. 16 in Ref. [99]. The resulting effect on the average cross-slip energy for these distributions are shown in Fig. 4.13(a). The values monotonically decrease with stress, and a naive interpretation would lead one to believe that the SRO case would have a higher cross-slip frequency compared to the random case. To approximate the effect of stress on the cumulative distribution function (CDF), the previously fitted gamma distribution is shifted according to Eq. 19 in Ref. [99]. Note that this can cause some negative energy barriers to have a non-zero probability, so with each stress-induced shift, a gamma CDF is refitted (the effect of this is detailed in the Supplementary Material document for this chapter). The resulting CDFs are then scaled up according to the weakest-link scaling procedure in Ref. [99] from $60b$ to $1000b$, and a PDF is extracted by numerically taking the derivative of the CDF. The resulting PDF, for the random and SRO case, are each inserted into Eq. 4.22, and (assuming that both scenarios have the same number of cross-slip attempts), inserted into Eq. 4.28. The result as a function of stress (between 200-1000 MPa) is plotted for the temperatures of 300 K, 600 K and 900 K in Fig. 4.13(b).

As can be seen in Fig. 4.13(b), even though the average activation energy for the SRO case is lower than the random case, the probability of cross-slip for the random case is orders of magnitude higher, which is due to the larger standard deviation of the random-state energy-barrier distribution. It is worth pointing out that for low temperatures and

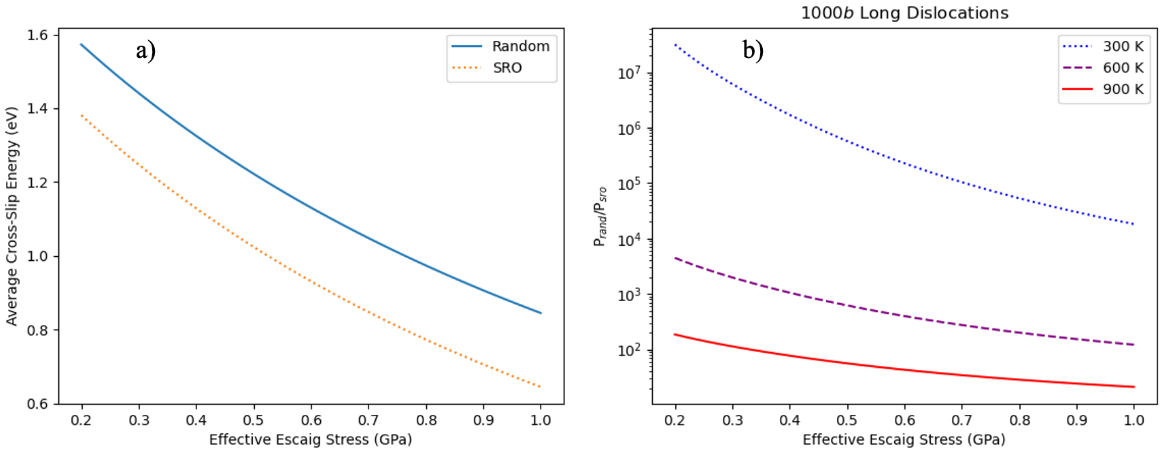

Figure 4.13: a) the effect of an effective Escaig stress due to an obstacle in front of the head of a planar array on the average cross-slip energy barrier for the random and SRO case. b) the ratio of cross-slip probability for the random and SRO case as a function of stress for the temperatures of 300 K, 600 K, and 900 K.

applied stresses, cross-slip events are unlikely to occur even in the random case (at room temperature, the probability of a successful cross-slip attempt with an activation barrier of 1 eV is on the order of 10^{-17}). The ratio of P_{rand}/P_{SRO} plotted in Fig. 4.13(b) shows that dynamic recovery decreases dramatically with the onset of SRO, but approaches the same value as that of the random case at high temperatures and high stresses. Such a suppression of dynamic recovery is consistent with the experimental results of work-hardening of Cu-Mn alloys (which exhibit planar slip [89, 90]), where a higher amount of Mn content (which is reported to have a marginal effect on the SFE but increase in the degree of SRO) results in an increased value of $\frac{d\rho}{d\epsilon}$ likely due to reduced dynamic recovery [90]. At later stages of deformation, planar slip transitions into wavy slip due to increased cross-slip, and the dislocation density starts to decrease as the dynamic recovery starts to increase. This is in agreement with the trends of Fig. 4.13(b), as higher stress decreases the ratio of the random and SRO cross-slip probability, which could be supplied by the nearby stress fields of other dislocations, especially at high dislocation densities. The fact that the results of our model Ni-Al alloy helps explain observations in a Cu-Mn alloy suggests that the effect of SRO on cross-slip, and its role in developing planar slip, can be applied more generally to FCC solid solution substitutional alloys which exhibit SRO (and perhaps short-range clustering), including both binary and multi-component chemically complex alloys. The current conclusion that SRO results in a significant reduction of dynamic recovery is in contrast with the conclusions drawn by Ref. [146]. The origin of this difference is that the current study considers the cross-slip probability of dislocations behind the head of a planar array to be conditional on the presence of a DAPB in the cross-slip plane.

The earlier assumptions of $P(\tau_{esc} \geq \tau_{esc}^{H}) = 1$ and $P(\tau_{esc} \geq \tau_{esc}^{F}) = 0$ used in the above analysis can be justified due to the localized internal stresses at the head of a dislocation pileup [86, 141, 48]. Note that in the case investigated, the Escaig stress is treated as an effective Escaig stress due to an obstacle as in Eq. 4.21. With a homogeneous applied Escaig stress in the bulk, this assumption would not be valid above 182.1 MPa. The assumption of $P(F|H) = 1$ would only decrease the actual ratio in Eq. 4.28 compared to the case where the conditional probability would be less than one, which does not change the main conclusion reached in this analysis. From the earlier discussion on correlated cross-slip, this assumption is more accurate for long dislocations in environments with stronger SRO. Also note that with increased temperature, the effects of entropy and diffusion start to become important. As temperature increases, entropic effects would presumably lower the free energy barrier for cross-slip, which may reduce the cross-slip probability ratio compared to that found here, especially at high homologous temperatures. Also, the effect of diffusion at higher temperatures could lead to a rearrangement of SRO towards a more disordered state. The current analysis should nevertheless be applicable at relatively low homologous temperatures.

Intersecting Planar Slip Arrays

The previous sections considered the effect of SRO on an isolated planar slip array. SRO could certainly influence the frequency and strength of certain dislocation interactions. For example, a planar slip array could intersect a DAPB formed on a conjugate slip plane. If the DAPB on the conjugate slip plane was formed by an array of dislocations with an opposite Burgers vector than that the array in the primary plane, cross-slip may be enhanced due to both the presence of a DAPB as well as the elastic attraction of the dislocations, potentially causing a rapid annihilation of dislocations. On the other hand, if the dislocation array in both slip planes had the same Burgers vector, there would be an elastic repulsion between them which would suppress slip in the primary plane. At later stages of deformation it is expected that more intersections of planar slip arrays occur. While earlier arguments certainly suggest that dynamic recovery should be suppressed overall, it is unclear whether or not work-hardening would increase or decrease compared to the random case as it would depend on the details of collective dislocation behavior. Investigating these aspects would require mesoscale modeling of dislocations incorporating the effects of SRO.

4.7 Conclusions

In this study, the effect of SRO and the presence of a DAPB on cross-slip energetics is investigated in a model Ni-10%Al alloy through the use of CI-NEB calculations. It was found that at the head of a planar slip array in a material with SRO, cross-slip is inhibited due to a stress condition that must be fulfilled in order to compensate for the creation of a DAPB during cross-slip. Without this stress condition being satisfied, it is unlikely for cross-slip to be aided by fluctuations from the mean cross-slip barrier, especially for longer dislocations and stronger amounts of SRO. A similar condition must be fulfilled for cross-slip out of a plane with a DAPB, an event which can occur behind the head of the planar slip array. Satisfying this second condition is unlikely due to the concentration of internal stress at the head of a planar slip array, which could lead to correlated cross-slip. We also present an analysis estimating the effect of SRO on dynamic recovery that is based on the differences in the calculated cross-slip energy distributions in a material with SRO compared to one with random configurational disorder. The results suggest a reduction in dynamic recovery due to SRO. This is in agreement with experimental observations of decreased dynamic recovery and increased work-hardening in Cu-Mn alloys, however a full understanding of the effect of SRO on work-hardening would require mesoscale models paramaterized by the results of atomistic studies such as those in the present study. The effect of SRO on cross-slip is likely a major factor underlying mechanical behavior beyond the yield point for concentrated binary and chemical complex FCC alloys, and suggests important directions for further study of the effect of correlated cross-slip as well as the effect of an increased internal stress on deformation behavior such as twin nucleation.

Chapter 5

Structure and Glide of Lomer and Lomer-Cottrell Dislocations in Model Concentrated Alloy Solid Solutions[1]

5.1 Introduction

Understanding the stability of Lomer (L) and Lomer-Cottrell (LC) dislocations is crucial for insight into a variety of deformation and microstructural behaviors in face-centered cubic (FCC) metals and alloys. L and LC dislocations have historically been proposed as major contributors to work-hardening in these systems [14, 15, 149], which is a property that has been shown to depend on stress orientation in single crystal tensile tests [150, 151]. Recent transmission electron microscope (TEM) observations of deformed FCC high-entropy alloys have reported the presence of LC dislocations [152, 153, 154, 155, 156], suggesting that these dislocations may play a role in the properties of these alloys. LC dislocations have also been considered as possible twin nucleation sites [157, 158, 159], which can increase ductility and strength (e.g., through a dynamic Hall-Petch effect). Additionally, glide of L dislocations in the (100) plane could aid in deformation at higher temperatures through direct motion of L dislocations [160] or through L dislocations acting as kink-pairs for a screw dislocation dissociated on a compact plane migrating in a (100) plane [161]. A reaction involving a L dislocation has previously been used to explain the motion of a low-angle $\langle 110 \rangle$ tilt boundary in FCC aluminum [162]. The results summarized here are representative of previous literature that clearly demonstrate the important role of L and LC dislocations in the deformation behavior and microstructures of FCC metals and alloys.

---

[1] The results presented in this chapter and the corresponding Supplementary Material document have been published as a regular article titled "*Structure and glide of Lomer and Lomer-Cottrell dislocations: Atomistic simulations for model concentrated alloy solid solutions*" in Physical Review Materials, **6**, 103603, (2022), doi: 10.1103/PhysRevMaterials.6.103603 by Anas Abu-Odeh, Tarun Allaparti, and Mark Asta [148]. The material is presented here with the permission of co-authors and publishers.

Lomer and Lomer-Cottrell dislocations are formed by the reaction of a 60° mixed dislocation with a Burgers vector of $\frac{a}{2}[\bar{1}10]$ on the (111) plane with another 60° mixed dislocation with a Burgers vector of $\frac{a}{2}[101]$ on the $(\bar{1}11)$ plane (Fig. 5.1a), where a is the FCC lattice constant [10]. The L dislocation is formed through the reaction of the 60° mixed dislocations at the intersection of the (111) and $(\bar{1}11)$ planes to form a dislocation with a $\frac{a}{2}[011]$ Burgers vector and line direction along $[0\bar{1}1]$ (Fig. 5.1b):

$$\frac{a}{2}[\bar{1}10] + \frac{a}{2}[101] \rightarrow \frac{a}{2}[011]. \tag{5.1}$$

The (100) glide plane of the L product dislocation is not a closed-packed plane, and will thus have a higher barrier for glide than dislocations gliding on the {111} planes. The L dislocation thus acts as an obstacle for subsequent dislocations gliding on the intersecting (111) and $(\bar{1}11)$ planes.

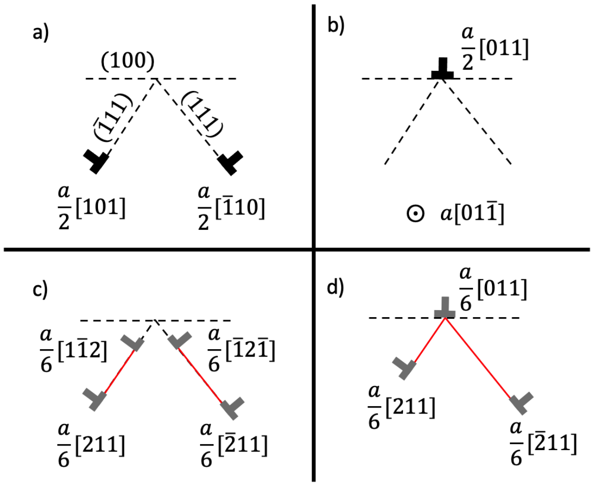

Figure 5.1: a) Two perfect 60° mixed dislocations lying on intersecting {111} planes. b) A Lomer dislocation on a (100) plane. c) Two dissociated 60° mixed dislocations lying on intersecting {111} planes. d) A Lomer-Cottrell dislocation. Black symbols represent perfect dislocations, grey symbols represent partial dislocations, and red lines represent intrinsic stacking faults. The circled dot in b) represents the direction out of the page.

In the FCC crystal structure, the 60° mixed dislocations will dissociate into two Shockley partial dislocations bounding a stacking fault (Fig. 5.1c) through the following reactions:

$$\frac{a}{2}[\bar{1}10] \rightarrow \frac{a}{6}[\bar{1}2\bar{1}] + \frac{a}{6}[\bar{2}11] \tag{5.2}$$

$$\frac{a}{2}[101] \rightarrow \frac{a}{6}[1\bar{1}2] + \frac{a}{6}[211]. \tag{5.3}$$

An alternative reaction to Eq. 5.1, with the same net Burgers vector, can be written as:

$$\begin{aligned} &\frac{a}{6}[\bar{1}2\bar{1}] + \frac{a}{6}[1\bar{1}2] + \frac{a}{6}[\bar{2}11] + \frac{a}{6}[211] \rightarrow \\ &\qquad \frac{a}{6}[011] + \frac{a}{6}[\bar{2}11] + \frac{a}{6}[211]. \end{aligned} \tag{5.4}$$

The product configuration of Eq. 5.4 is the LC dislocation (Fig. 5.1d) with the reactants being partial dislocations from the two 60° mixed dislocations. The leading partial dislocations of the two 60° mixed dislocations form a sessile stair-rod partial dislocation with a Burgers vector of $\frac{a}{6}[011]$. This dislocation is connected to the other two partial dislocations through stacking faults on the intersecting closed-packed planes. The LC configuration is conventionally considered to be a stronger barrier than the compact L dislocation against subsequent dislocation motion due to the sessile nature of the stair-rod partial dislocation.

While dislocations tend to be dissociated in FCC crystal structures, the LC dislocation is not guaranteed to form from two dissociated 60° mixed dislocations. It is possible to form the L dislocation instead. Predicting the product configuration from linear elasticity theory is difficult without the knowledge of dislocation core energies [163, 164]. Alternatively, the core configuration can be directly modeled through atomistic simulations.

Previous linear elasticity-based analyses on these dislocations, while lacking consideration of the dislocation core, have resulted in useful insights. Linear elasticity theory, with either anisotropic [165] or isotropic [166] elastic constants, has been used to predict an asymmetrical dissociation of LC dislocations across the closed-packed planes, a conclusion that was later verified with atomistic simulations [164]. Stroh [167] has proposed that under an applied stress it may be possible for a LC dislocation to have its partial dislocations recombine into a L dislocation to glide in a (100) plane or that it may decompose into the reactant dislocations from which it was formed. An anisotropic linear elasticity based dislocation dynamics model of a LC junction in FCC metals and its response to stress through an "unzipping" mechanism [20], which causes the L/LC configuration to decompose into its parent dislocations, was able to replicate many of the details of a quasicontinuum method that treated atoms near the junction with an interatomic potential [168]. This led the authors of the former study to conclude that knowledge of elastic interactions and stacking fault energy is all that is needed to determine the junction structure. Challenges are associated with extending such analyses, as described above. Specifically, it is difficult to predict if the L or LC configuration is lower in energy without knowledge of core energies [163, 164], contrary to suggestions of previous authors [20]. The importance of the core structure is also emphasized by Stroh [167] in the context of possible transformations of a LC dislocation. Further understanding of L and LC dislocations, and by extension their role in the mechanical properties of FCC metals and alloys, thus requires an accurate description of the dislocation core structure.

Specifically, it is important to understand how a variation in composition affects the resistance of a L or LC dislocation against glide, which gives a measure of their capacity to harden the material by blocking the glide of other dislocations. Further, it is important to understand how composition affects the different possible core transformations, such as the nucleation of a nanotwin, that can occur. These core transformations can result in further hardening of the material especially if they produce faults that intersect glide planes. In addition, understanding the stress orientation dependence of glide resistance and core transformations may reveal insights into the orientation dependence of work-hardening in FCC alloys. While the previously mentioned "unzipping" mechanism has been studied as a stress-induced response of these dislocations [168, 20], additional responses are expected to occur. Evidence for this is present in the form of TEM studies of glide dislocations on (100) planes in high- [169] and low- [170] stacking fault energy FCC alloys. In the latter case, a constriction of a LC dislocation to a L dislocation is expected to occur to facilitate glide. The competition between these (and potentially other) responses is likely due to a combination of pinning, line tension, stress field, and core structure effects.

Motivated by these questions, we undertake in this work the modeling of L and LC dislocations through atomistic simulations using elastic- and lattice-Green's-function flexible boundary conditions in a Cu-Ni average-atom system described by an embedded-atom method (EAM) potential [27, 26]. The equilibrium structure of these dislocations are surveyed under different compositions, shear stress orientations, and magnitudes in order to probe their resistance to glide and different possible core transformations. We find that depending on the shear stress orientation, the relative resistance against glide on a (100) plane is not solely due to the relative value of the unstable stacking-fault energy on that plane. Additionally, core transformations involving faults can occur for materials with both low (Cu-rich compositions) and high (Ni-rich compositions) fault energies depending on the orientation and magnitude of the stress field. The work presented here thus represents a systematic study of L and LC dislocations as a function of composition and stress orientation that extends previous atomistic and continuum studies of this topic.

5.2 Model and Methods

Applied Pure Shear Stress States

As we will be considering an array of variables including solute composition, stress orientation, and stress magnitude, we will simplify the analysis by focusing on a few shear stress orientations. We consider a LC configuration such as that shown in Fig. 5.2a. In this configuration, three partial dislocations are present: the stair-rod partial dislocation (SRP) which lies on a (100) plane with a Burgers vector of $\frac{a}{6}[011]$, a Shockley partial dislocation (SP1) which lies on one of the $\{111\}$ planes intersecting the (100) plane and is connected to SRP through a short intrinsic stacking fault, and another Shockley partial dislocation (SP2) which lies on the other $\{111\}$ plane intersecting the (100) plane and is connected to SRP through a long intrinsic stacking fault. SP1 and SP2 have Burgers vectors of either $\frac{a}{6}[211]$ or $\frac{a}{6}[\bar{2}11]$, depending on if the dislocation is to the left or right of SRP, respectively.

We consider a pure shear state, represented by the following stress tensor in the supercell basis (the x-direction, which is represented by [011] in the crystal basis, is represented by

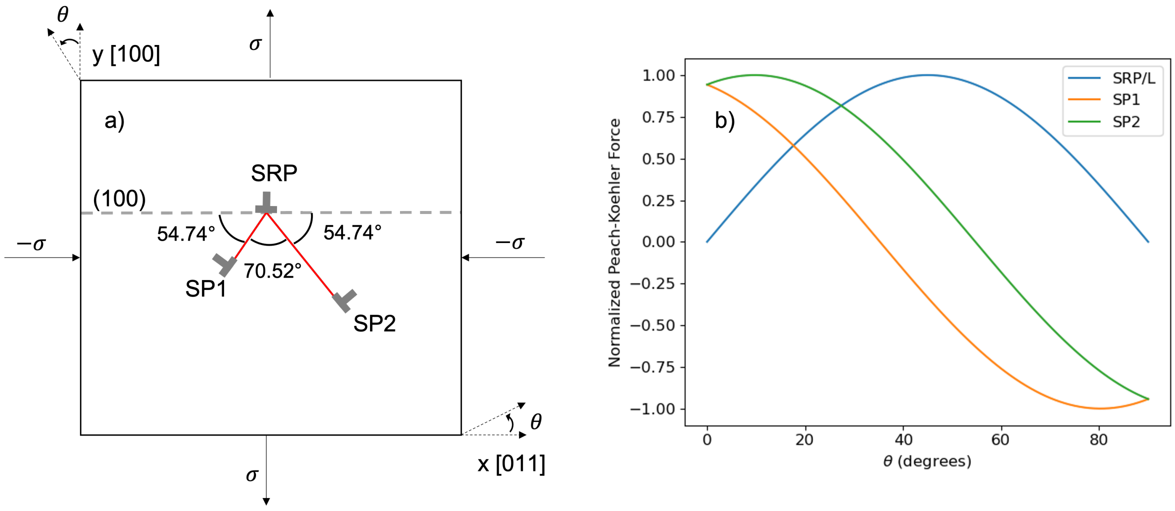

Figure 5.2: a) Schematic of a LC configuration under pure shear. Partial dislocations are represented by grey half-crosses and intrinsic stacking faults are represented by red lines. The directions are given in the crystal basis. b) Normalized Peach-Koehler (P-K) forces for partial dislocations in a) as a function of θ. The meaning of the sign of the P-K forces is given in the text.

[100] in the supercell basis):

$$\Sigma = \begin{bmatrix} -\sigma & 0 & 0 \\ 0 & \sigma & 0 \\ 0 & 0 & 0 \end{bmatrix}. \tag{5.5}$$

As the crystal is rotated counterclockwise (or alternatively, the stress field is rotated clockwise) about the z-axis by an angle θ, the resulting stress field with respect to the crystal coordinates becomes:

$$\Sigma' = Q\Sigma Q^T \tag{5.6}$$

where Q is the rotation matrix:

$$Q = \begin{bmatrix} \cos\theta & \sin\theta & 0 \\ -\sin\theta & \cos\theta & 0 \\ 0 & 0 & 1 \end{bmatrix}. \tag{5.7}$$

The different partial dislocations will have a different Peach-Koehler (P-K) force as a function of θ. The P-K force per unit length ($\vec{F}^{PK}$) is defined as [48]:

$$\vec{F}^{PK} = (\Sigma' \cdot \vec{b}) \times \vec{l} \tag{5.8}$$

where $\vec{b}$ is the Burgers vector and $\vec{l}$ is the unit line direction of the dislocation. The normalized P-K forces (with σ, $|\vec{b}|$, and $|\vec{l}|$ set to one for each dislocation) are calculated and plotted in Fig. 5.2b for values of θ between 0-90° assuming SP1 to be to the left of SRP. In the supercell basis, the unit Burgers vectors for SRP, SP1, and SP2 are [100], $Q^T(\theta = 54.74°) \cdot [100]$, and $Q^T(\theta = -54.74°) \cdot [100]$, respectively, and the unit line direction is [001]. The value of θ is taken as the angle between the Burgers vector of SRP with SP1 or SP2. Positive values for SP1 and SP2 represent motion towards SRP, while positive values for SRP represent motion to the right. The normalized P-K force on SRP is also equivalent to the normalized P-K force on the compact L dislocation (the absolute P-K force will be three times larger for the L dislocation than SRP as the magnitude of its Burgers vector is three times larger). The varying P-K forces will result in different responses of L and LC dislocations under applied stresses with different values of θ. To simplify for further analysis, we consider five values of θ: 0.5°, where SRP has a P-K force near zero and SP2 has a slightly higher P-K force than SP1, 9.74°, where SP2 has its maximum normalized P-K force, 35.26°, where SP1 has a P-K force of zero, 45°, where SRP has its maximum normalized P-K force, and 90°, where both SP1 and SP2 want to move away from SRP, which has a P-K force of zero. We will explore the effect of stresses given by Eq. 5.6 at these orientations through the methodology presented in the next section.

Computational Details

We employ atomistic simulations using flexible boundary conditions, as described in Ref. [42], to model L and LC dislocations. The set-up of the simulations is shown in Fig. 5.3. The supercell is partitioned into three regions: an inner atomistic region, an outer continuum region, and a buffer Green's function (GF) region. The atomistic region has a radius of 60 $\mathring{A}$ for pure Cu, and is scaled based on the lattice constant for other compositions. The GF region has a thickness of 13 $\mathring{A}$, which is larger than twice the cutoff of the EAM potential (R^{EAM}_{cutoff}), and the distance between the boundary of the GF region to the surface of the continuum region is larger than $2R^{EAM}_{cutoff}$. The thickness of the cell in the z-direction (the dislocation line direction) is $a/\sqrt{2}$. Periodic boundary conditions are applied along the z-direction, simulating an infinitely straight dislocation. All atoms are initially displaced according to the anisotropic linear elasticity theory solution for displacements around a L dislocation centered in the atomistic region using the Babel package [71]. The atomistic region is then relaxed using the FIRE algorithm [75, 133] as implemented in LAMMPS [76] with a force tolerance of 10^{-7} eV/$\mathring{A}$ or until 100,000 minimization steps are reached (the maximum two-norm of the global force vector in the atomistic region from these cases is 1.34×10^{-5} eV/$\mathring{A}$). Following this step, forces on atoms in the GF region are output for GF relaxation. With these forces, the positions of all atoms in the cell are updated through the addition of displacements obtained from the following relation [42]:

$$u_i^m = \sum_n G_{ij}(\mathbf{r}^{mn}) f_j^n \tag{5.9}$$

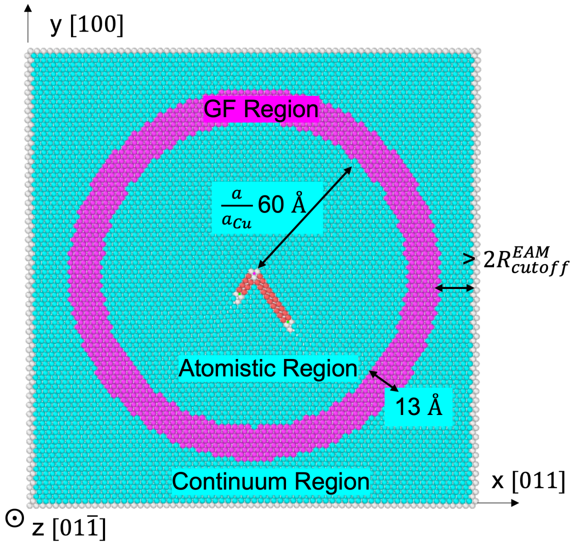

Figure 5.3: The simulation cells used for relaxing L and LC dislocations are represented by this example for a fully relaxed LC dislocation in pure Cu in the same orientation as Fig. 5.2. The directions are given in the crystal basis. The region highlighted in magenta represents the GF region. Atoms colored in cyan, red, and grey represent FCC, HCP, and "other" environments according to the common neighbor analysis scheme [78] as implemented in OVITO [77].

where f_j^n is the force in the j direction on atom n in the GF region, u_i^m is the resulting displacement in the i direction for atom m, and G_{ij} is the GF which maps f_j^n to a displacement as a function of $\mathbf{r}^{mn}$, the vector between the positions of atoms m and n. The relaxation process starting from the atomistic relaxation step is repeated until the magnitude of forces on each atom in the GF region are less than 10^{-5} eV/$\AA$ or after 15 total iterations have been exceeded. The maximum force magnitude on an atom in the GF region in the latter case has a wide range of values and is discussed further in the Results section. Reaching the maximum number of iterations occurs due to dislocations approaching, or in some cases gliding into, the GF region, which is an inevitable consequence of using a finite sized supercell. Cases where this occurs will be discussed below in relation to trends at lower stresses and other compositions.

The use of this approach requires $G_{ij}(\mathbf{r}^{mn})$ to be evaluated. As the set-up of the simulation results in a two-dimensional problem, forces in the GF region are treated as line forces. For a sufficiently large $|\mathbf{r}^{mn}|$, $G_{ij}(\mathbf{r}^{mn})$ for a line force can be evaluated through the use of anisotropic linear elasticity theory [74]. However, as $|\mathbf{r}^{mn}|$ tends to 0, $G_{ij}(\mathbf{r}^{mn})$ must be evaluated using an interatomic potential. Therefore, we express $G_{ij}(\mathbf{r}^{mn})$ as:

$$G_{ij}(\mathbf{r}^{mn}) = \begin{cases} G^{el}_{ij}(\mathbf{r}^{mn}), & |\mathbf{r}^{mn}| \geq R^{GF}_{cutoff} \\ \\ G^{lat}_{ij}(\mathbf{r}^{mn}), & |\mathbf{r}^{mn}| < R^{GF}_{cutoff} \end{cases} \tag{5.10}$$

where $G^{el}_{ij}(\mathbf{r}^{mn})$ is the elastic GF, $G^{lat}_{ij}(\mathbf{r}^{mn})$ is the lattice GF, and R^{GF}_{cutoff} is an imposed cutoff representing the minimum value of $|\mathbf{r}^{mn}|$ before the elastic GF can be used. The elastic GF is calculated following Ref. [74], which only requires the anisotropic elastic constants (rotated to the desired orientation of the crystal) and the lattice constant as input. While there are various ways to calculate the lattice GF [171, 172, 173], we choose to follow a similar procedure as that found in Ref. [42] due to its simplicity. A perfect lattice in the same orientation as Fig. 5.3 is created with a length of approximately 40 $\mathring{A}$ in the x- and y-direction, and a thickness in the z-direction of $a/\sqrt{2}$. A fixed line force of $5{\times}10^{-6}$ eV/$\mathring{A}^2$ in either the x-, y-, or z-direction is applied on the center atom. Resulting displacements on all other atoms are applied using the elastic GF. Maintaining a fixed force on the center atom, a region within a 20 $\mathring{A}$ radius of the center atom is relaxed using LAMMPS below a 10^{-7} eV/$\mathring{A}$ force tolerance. Using the resulting displacements and the force on the center atom, the lattice GF as a function of $\mathbf{r}^{mn}$ is tabulated using Eq. 5.9 with R^{GF}_{cutoff} set to $5a/a_{Cu}$ $\mathring{A}$, where a_{Cu} is the lattice constant for pure Cu. We chose this value as it is similar in magnitude to that used in previous work [42], although it should be mentioned that the error of the elastic GF compared to the lattice GF scales with $(1/R^{GF}_{cutoff})^2$ [171]. In the dislocation geometry, we assume that the lattice GF can be approximated by that obtained from the perfect lattice, and use a lattice GF value corresponding to the best matching $\mathbf{r}^{mn}$ vector between two atoms. We found that the predicted LC dislocation core structure for pure Cu using GFs obtained in this way agreed with the converged core structure obtained from a fixed boundary condition method with increasing system size (Fig. S1 in the Supplementary Material document for this chapter).

In order to apply a desired stress state Σ', displacement gradients are applied according to the following linear elasticity relation:

$$(u_{i,j} + u_{j,i})/2 = \epsilon_{ij} = S_{ijkl}\Sigma'_{kl} \tag{5.11}$$

where $u_{i,j}$ is a component of a displacement gradient tensor (where $u_{i,j} = u_{j,i} = \epsilon_{ij}$ for pure shear, as all components of the infinitesimal rotation tensor are zero [174]), ϵ_{ij} is a component of the strain tensor, and S_{ijkl} is a component of the compliance tensor, which is obtained from an inversion of the elastic constant tensor. Displacements (u^m_i) corresponding to the displacement gradient ($u^m_i = u_{i,j}r^m_j + C_i$, where r^m_j is the reference position of atom m in the j direction, and C_i is a constant set to keep the atoms within the simulation box) with σ equal to 100 MPa and a given value of θ are added to the reference unstressed, relaxed configuration. The resulting structure is then relaxed through the approach described above, and if the GF region force criterion is met displacements corresponding to the same displacement gradient are added by treating the new relaxed structure as the reference state. Assuming linear elasticity holds, the addition of these new displacements increases the applied value of σ by 100 MPa. This procedure is iterated until a given configuration reaches the maximum number of GF relaxation iterations. We assume that the GF does not change significantly under the applied stresses in this study. In order to avoid the possibility of atoms coming in and out of the region defined by R^{GF}_{cutoff}, we change the criteria for the application of the lattice GF in Eq. 5.10 to be:

$$\frac{(r_x^{mn})^2}{((1+\epsilon_{11})R^{GF}_{cutoff})^2} + \frac{(r_y^{mn})^2}{((1+\epsilon_{22})R^{GF}_{cutoff})^2} < 1. \tag{5.12}$$

Instead of a circular cutoff as represented by Eq. 5.10, the above equation represents the resulting ellipse when the system is strained in the x- and y-direction (ϵ_{11} and ϵ_{22}, respectively).

We choose to investigate Cu-Ni solid solutions between 0-100 at.% Ni in increments of 10%. This system is chosen because it allows for the monotonic change of a low stacking fault energy system (Cu) to a high stacking fault energy system (Ni) with an increase in Ni. In an actual alloy, the GF will be a function of atom type, and any response to stress will become dependent on the dislocation length. Since the intent of the current study is to understand general trends, we circumvent these complications by making use of an average-atom representation of the Cu-Ni alloy, through appropriate averaging of the EAM potential [26], as described in Ref. [27]. Using the average-atom description, we calculate lattice and elastic constants for each composition in order to carry out the above procedures for relaxation. We also calculate stable and unstable stacking fault energies to gain insight into the behavior of these dislocations. These, along with results of the dislocation relaxations, are reported in the next section.

5.3 Results

Material Properties

Fig. 5.4 displays the calculated stacking fault energies for the Cu-Ni average-atom alloys. The results show that the addition of Ni causes the stacking fault energies to increase. We have calculated five different stacking fault energies: the unstable and stable intrinsic stacking fault energies ($\gamma^{UISF}_{(111)}$ and $\gamma^{ISF}_{(111)}$) on the (111) plane, the unstable and stable extrinsic stacking fault energies ($\gamma^{UESF}_{(111)}$ and $\gamma^{ESF}_{(111)}$) on the (111) plane, and the unstable stacking fault energy ($\gamma^{USF}_{(100)}$) on the (100) plane. Lower values of $\gamma^{ISF}_{(111)}$ are expected to favor the dissociated LC structure relative to the compact L structure. The lower the value of $\gamma^{UESF}_{(111)}$, the more we would expect an extrinsic fault (or nanotwin) to be able to nucleate from the dislocation under the appropriate applied stress. The lower the value of $\gamma^{USF}_{(100)}$, the easier it would be for a compact L dislocation to glide. Of course, the actual details of such scenarios depend on the core structure as shown in the following subsections.

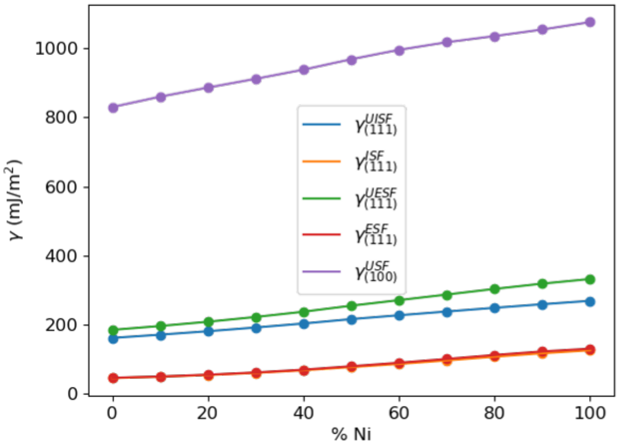

Figure 5.4: Calculated stacking fault energies for the Cu-Ni average-atom alloy systems. The symbols in the legend are defined in the main text above.

The lattice and elastic constants of the average alloys are displayed in Fig. S2 in the Supplementary Material document for this chapter. The results show that with the addition of Ni the lattice constant decreases, while the elastic constants increase.

Equilibrium Core Structures

The equilibrium core structures at their unstressed state for all compositions relaxed to the force convergence criterion. Fig. 5.5 shows the structure of the dislocation cores found in pure Cu, Cu-30% Ni, Cu-40% Ni, and pure Ni. As can be clearly seen, intrinsic stacking faults (colored in red in Fig. 5.5) are not present at compositions above 30% Ni. This suggests a transition between LC to L dislocations in a region between 30-40% Ni. Note that whether or not SP2 is to the right or the left of the SRP for a LC dislocation depends on slight differences of where the center of the linear elasticity solution is placed with respect to the lattice. The LC dislocation being the stable configuration in pure Cu and the L dislocation being the stable configuration in pure Ni is in agreement with results from Ref. [175] using different potentials for the pure elements.

The LC configurations present in 0-30% Ni are all asymmetric, in agreement with elasticity predictions [165, 166]. However, the ratio of the distance between SP2 and SRP (d2) to the distance between SP1 and SRP (d1) using elasticity theory is predicted to be 3.82, independent of the material system. Using the DXA algorithm [176], we find the d2/d1 ratio to be 2.36, 2.34, 2.11, and 1.92 for the pure Cu, Cu-10% Ni, Cu-20% Ni, and Cu-30% Ni systems, respectively. This seems to be due to a decrease in d2 with increasing $\gamma^{ISF}_{(111)}$ (45 to 60 mJ/m^2), as d1 maintains a value of approximately 9.8 $\mathring{A}$ across these systems. Ref. [164] found the d2/d1 ratio to be 3.4 and 3.6 when modeling LC dislocations in pure

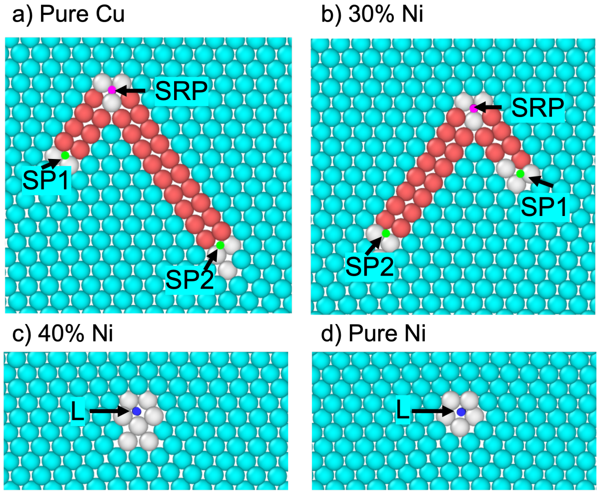

Figure 5.5: Relaxed equilibrium core structures for a) pure Cu, b) Cu-30% Ni, c) Cu-40% Ni, and d) pure Ni. Atoms are colored similar to Fig. 5.3. Colored dots near grey atoms represent the end of dislocation lines found by the DXA algorithm [176] as implemented in OVITO [77]. The green, magenta, and blue dots represent SP1/SP2, SRP, and L dislocations, respectively.

Cu and Ag, respectively. The value of $\gamma^{ISF}_{(111)}$ from the interatomic potentials used in Ref. [164] was calculated to be 36 mJ/m^2 for Cu and 23 mJ/m^2 for Ag. The potential used in the present study results in a $\gamma^{ISF}_{(111)}$ value of 45 mJ/m^2 for Cu. Thus it is expected that the linear elasticity description for the LC structure is only applicable in the limit of low values of $\gamma^{ISF}_{(111)}$. Otherwise, the calculation of an accurate dislocation core structure requires atomistic modeling to capture near-core effects.

We further analyze the core structures by looking at differential displacement (DD) maps [177] for pure Cu and pure Ni as shown in Fig. S3 in the Supplementary Material document for this chapter. For Cu, three different projections are shown corresponding to the Burgers vectors of the different partial dislocations in the LC configuration. For Ni, the three different projections include the two Shockley partial dislocation Burgers vectors of the LC configuration, and the Burgers vector of the L dislocation. While the L configuration in pure Ni does not show any intrinsic stacking faults in Fig. 5.5d (the value of $\gamma^{ISF}_{(111)}$ for pure Ni is 125 mJ/m^2), the DD maps show the presence of displacements associated with the projection of Shockley partial dislocation Burgers vectors in a $(\bar{1}11)$ or (111) plane just under the L dislocation. The small amount of core spreading in these planes appears to impact the response of the core under certain stress states, as will be discussed further below.

Effect of an Applied Shear Stress

Here we present the results of applying different stresses on L/LC dislocations in the order of orientations that show the simplest responses. Simulations are terminated when the GF iterations exceeds 15 total iterations. As discussed above, we find that this occurs when a partial or full dislocation moves close to the GF region, as shown in Fig. S4 , which can occur both at relatively low or high stresses depending on the available core states. The range of the maximum magnitude of the force in the GF region is given for each value of θ below. The resulting core structures are classified using the DXA algorithm [176]. Note that before applying any stress, SP2 is to the right of SRP for 0-20% Ni, while for 30% Ni SP2 is to the left of SRP. Accounting for this, a value of $-\theta$ was used for 30% Ni for the cases where θ equals 9.74°, 45°, and 35.26° in order to be consistent with the P-K force values in Fig. 5.2b. However, we tested +/- values of θ for the mentioned angles for 0-30% Ni and did not find significant differences in the results.

Pure Shear with $\theta = 90°$

The results for a pure shear stress state with θ equal to 90° are shown in Fig. 5.6. Each column in the plot represents a composition, and each row represents a value of σ. The different symbols represent different states of the dislocation as described in the legend. In this scenario, dislocations that start as LC configurations at zero stress remain in the LC configuration, while dislocations that start as L configurations transition to the LC configuration at a high enough stress. This occurs because the P-K force on SP1 and SP2 favors motion away from SRP, which has a P-K force of zero at this value of θ. The stress at which this transition occurs increases with increasing Ni content, which makes intuitive sense as the values of $\gamma^{ISF}_{(111)}$ and $\gamma^{USF}_{(111)}$ increase with Ni content.

The maximum magnitude of a force vector on an atom in the GF region at the terminated state ranged from 1.1×10^{-5} eV/$\AA$ to 3.3×10^{-3} eV/$\AA$. These forces are relatively small and are not expected to have a significant effect on the final core structure. Additionally, the final core structure of the terminated states being LC dislocations is consistent with the trend of the converged calculations in Fig. 5.6.

Pure Shear with $\theta = 9.74°$

The results for a pure shear stress state with θ equal to 9.74° are shown in Fig. 5.7. In this scenario, dislocations that start as L configurations at zero stress remain in the L configuration until a high enough stress is reached where the dislocation begins to glide away from its initial position on the (100) plane. Dislocations that start as LC configurations at zero stress eventually transition into a L configuration with increasing stress, and eventually glide on the (100) plane. This occurs because the P-K force on both SP1 and SP2 drives them to combine with SRP to form a L configuration, which has a non-zero P-K force for glide. The stress at which glide on the (100) plane occurs increases with increasing Ni content, which makes intuitive sense as the value of $\gamma^{USF}_{(100)}$ increases with Ni content.

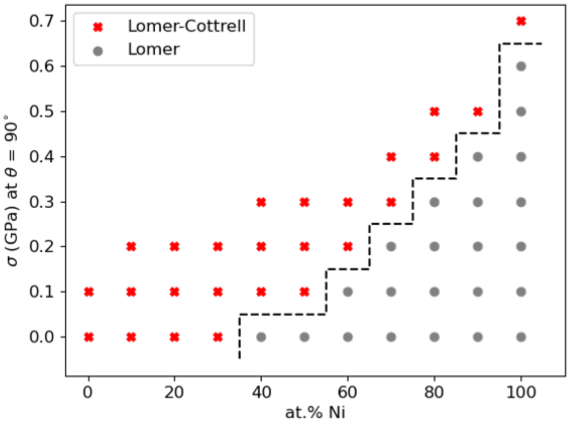

Figure 5.6: Dislocation states at a given value of σ and Ni content for a pure shear stress state with θ equal to 90°. The top data point at each composition reached the maximum number of GF iterations. The black dashed line represents a boundary between different dislocation states.

The maximum magnitude of a force vector on an atom in the GF region at the terminated state ranged from 2.8×10^{-3} eV/$\mathring{A}$ to 5.2×10^{-2} eV/$\mathring{A}$. As all of the terminated states at this value of θ result in a L dislocation gliding towards the GF region (which begins early on in the GF relaxation cycle), the forces at the GF region do not change the conclusion that the dislocation is expected to glide in an infinite medium.

Pure Shear with $\theta = 45°$

The results for a pure shear stress state with θ equal to 45° are shown in Fig. 5.8a. In this scenario, dislocations that start as LC configurations at zero stress remain in the LC configuration. For Ni concentrations in the range of 40-80%, there is a transformation from an initial L configuration to a LC configuration, and the stress at which this transition occurs increases with increasing Ni content. The resulting LC configurations are strongly asymmetrical, as there are opposite driving forces at $\theta = 45°$ for SP1 and SP2 as shown in Fig. 5.2b. However, above 80% Ni, the L dislocations glide on the (100) plane instead of transforming into a LC configuration. Surprisingly, the stress at which this occurs for 100% Ni is lower than that for 90% Ni, which is also lower than the stress for the L to LC transition at 80% Ni.

To investigate the reason for this, we analyze the L core structure in more detail. Specifically, we consider three atoms (colored in black in the inset of Fig. 5.8b). The first atom (A), is the atom near the bottom of the core. The other two atoms (B and C) are to the left and right of A, respectively. These atoms are chosen because they are close to the core and because the A-B atom pair and A-C atom pair each bound one of the two {111} planes

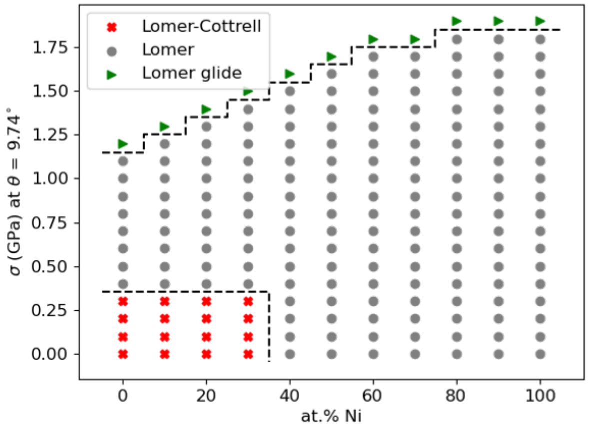

Figure 5.7: Dislocation states at a given value of σ and Ni content for a pure shear stress state with θ equal to 9.74°. The top data point at each composition reached the maximum number of GF iterations. The black dashed lines represent boundaries between different dislocation states.

that the dislocation can spread in. We define a core asymmetry parameter as a function of stress ($\lambda(\sigma)$) as:

$$\lambda(\sigma) = \frac{|d_{AB}(\sigma)| - |d_{AC}(\sigma)|}{a} \tag{5.13}$$

where $d_{AB}(\sigma)$ and $d_{AC}(\sigma)$ represent the distance of atoms B and C, respectively, to atom A at a given value of σ. This parameter describes how much the dislocation core is spread in the plane between atoms A and B compared to the plane between atoms A and C. We track this parameter while the dislocation core remains in the static L configuration at compositions of 80%, 90%, and 100% Ni (shown in Fig. 5.8b). For 80% Ni, we find that $\lambda(\sigma)$ monotonically increases with σ. This is consistent with the fact that this structure will eventually transform into a strongly asymmetric LC structure with the largest stacking fault present in the plane between atoms A and B. For 90% and 100% Ni, $\lambda(\sigma)$ initially increases with σ until a maximum is reached, after which the value begins to decrease. The maximum for 100% Ni is smaller than that for 90% Ni and seems to appear at a lower value of σ than the maximum for 90% Ni. This can be rationalized through the fact that a higher amount of Ni content results in higher values of $\gamma_{(111)}^{UISF}$ and $\gamma_{(111)}^{ISF}$, so it is increasingly difficult to have core spreading in the $\{111\}$ planes, which is why a LC configuration is not observed at the 90% and 100% Ni compositions. When there is more core spreading in $\{111\}$ planes, it becomes difficult for the dislocation to glide on the (100) plane, even though this orientation represents the maximum normalized P-K force for glide on the (100) plane. This is why the L dislocation at 100% Ni glides at a lower stress than at 90% Ni. This situation represents a competition in normalized P-K forces and fault energies for different planes.

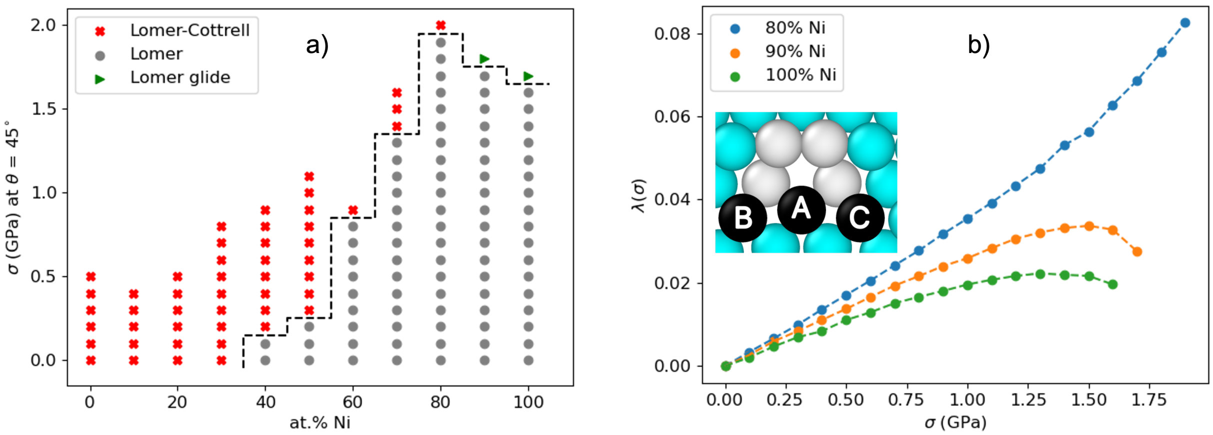

Figure 5.8: a) Dislocation states at a given value of σ and Ni content for a pure shear stress state with θ equal to 45°. The top data point at each composition reached the maximum number of GF iterations. The black dashed line represents a boundary between dislocation states. b) Values of the core asymmetry parameter defined in Eq. 5.13 as a function of stress for 80%, 90%, and 100% Ni. Inset: view of a L dislocation core where the black atoms are the atoms considered for the core asymmetry parameter.

The maximum magnitude of a force vector on an atom in the GF region at the terminated state below 80% Ni ranged from 1.0×10^{-5} eV/$\AA$ to 1.7×10^{-3} eV/$\AA$. These relatively low values, as well as the trend in Fig. 5.8a, suggest that the LC core structure should still be the expected configuration at the given values of σ of the terminated states. At 80% Ni and above, these values ranged from 1.8×10^{-2} eV/$\AA$ to 5.2×10^{-2} eV/$\AA$. For 80% Ni, this is due to one of the partial dislocations belonging to the LC core approaching very close to the GF region. A LC core structure at this composition is still expected as it is consistent with the trend in $\lambda(\sigma)$ with increasing σ. Glide above 80% Ni is also expected based on the trend in $\lambda(\sigma)$.

Pure Shear with $\theta = 35.26°$

The results for a pure shear stress state with θ equal to 35.26° are shown in Fig. 5.9a. All cores that initially start in the L configuration at zero stress (as well as the 30% Ni configuration) glide on the (100) plane when σ equals 1.5 GPa. We expect that the reason for this lack of dependence on Ni content is due to a similar effect as in the previous case, which is that for lower Ni content, there is more core spreading in {111} planes, making it difficult for the core to stay compact enough to glide on the (100) plane except at higher stresses. For higher Ni content, there is less core spreading, but the barrier to glide on the (100) plane is higher. These effects cancel out at this value of θ leading to a constant glide stress in the range of 30-100% Ni.

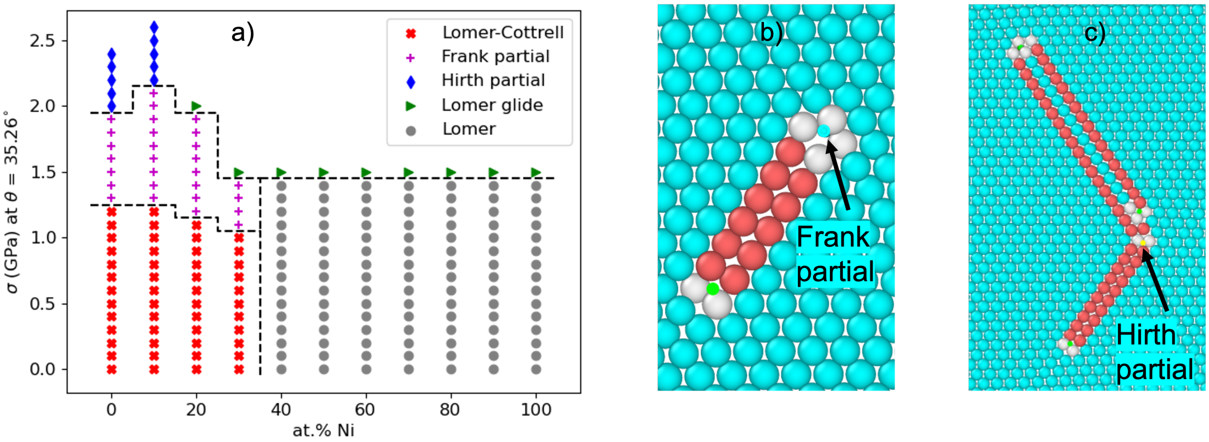

Figure 5.9: a) Dislocation states at a given value of σ and Ni content for a pure shear stress state with θ equal to 35.26°. The top data point at each composition reached the maximum number of GF iterations. The black dashed lines represent boundaries between dislocation states. b) Core structure at 0% Ni and σ equal to 1.9 GPa, and c) 2.0 GPa.

All cores that start in a LC configuration transition into a configuration similar to that shown in Fig. 5.9b, where the partial dislocation colored in light blue represents a Frank partial dislocation (with a Burgers vector of $\frac{a}{3}\langle 111\rangle$) as identified by the DXA algorithm [176]. With further applied stress, cores at 0% and 10% Ni transform into an obtuse configuration, similar to that configuration shown in Fig. 5.9c, where the yellow partial represents a Hirth partial dislocation (with a Burgers vector of $\frac{a}{3}\langle 100\rangle$) as identified by the DXA algorithm. The upper fault in Fig. 5.9c contains an extrinsic stacking fault, or a nanotwin. The transition from an acute lock to an obtuse lock with an extrinsic stacking fault shares similarities with the findings in a study by Baskes et al. [178], where the authors strain an initially obtuse lock and find an intermediate state of an acute lock with an extrinsic stacking fault. The Burgers vector of the partial dislocation at the apex of their acute lock is $\frac{a}{6}[011]$ (a stair-rod partial dislocation), and that of the partial dislocation at the apex of their obtuse lock is $\frac{a}{3}[100]$ (a Hirth partial dislocation). This suggests that these locks are related to each other by the removal or addition of an extrinsic stacking fault. For 20% and 30% Ni, the state with a Frank partial dislocation does not transition into an obtuse lock with further applied stress, but instead eventually glides on the (100) plane. We expect that this is due to a competition between $\gamma^{ESF}_{(111)}$ to form the obtuse configuration and $\gamma^{USF}_{(100)}$ for glide on the (100) plane.

The maximum magnitude of a force vector on an atom in the GF region at the terminated state for 0% and 10% Ni was 2.8×10^{-2} eV/$\AA$ and 5.4×10^{-3} eV/$\AA$, respectively. The obtuse configuration of these terminated states are just extended structures of the similar states found at smaller values of σ, so the obtuse configuration is still expected at the terminated state. Above 10% Ni, the maximum magnitude of the force vectors range from 1.8×10^{-3} eV/$\mathring{A}$ to 1.3×10^{-1} eV/$\mathring{A}$. As these states represent the glide of a L dislocation, the expected state would still be a continuous glide.

Pure Shear with $\theta = 0.5°$

The results for a pure shear stress state with θ equal to 0.5° are shown in Fig. 5.10a. All cores that initially start in the LC configuration at zero stress transition into the L configuration, and eventually emit two dissociated mixed dislocations. At 40% Ni the final state is an emission of two mixed dislocations as well. For dislocations that start in the L configuration at 50% Ni or more, a transformation occurs that results in an extrinsic stacking fault/nanotwin with a Frank partial dislocation as shown in Fig. 5.10d. This is confirmation of the proposed twin nucleation mechanism from a L dislocation as mentioned in Refs. [158, 159]. There is a large jump in stress required for the emission of mixed dislocations at 40% Ni and the creation of a nanotwin at 50% Ni. This is because before creating a nanotwin, the L core at 50% Ni and above begins to glide on the (100) plane but becomes stuck in an intermediate state (Fig. 5.10c). This intermediate state (labeled as "pre-twin" in Fig. 5.10a) prevents the emission of mixed dislocations, and eventually a nanotwin is nucleated. The small non-zero value of θ gives a small driving force for glide in the (100) plane in order to access the intermediate state, as well as a stronger driving force for nanotwin nucleation to the left of the core than to the right.

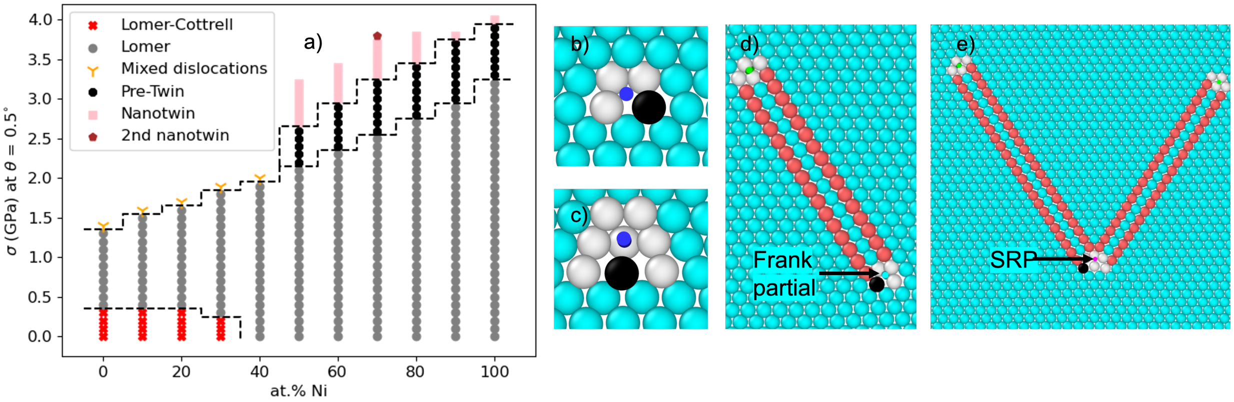

Figure 5.10: a) Dislocation states at a given value of σ and Ni content for a pure shear stress state with θ equal to 0.5°. The top data point at each composition reached the maximum number of GF iterations. The black dashed lines represent boundaries between dislocation states. b) Core structure at 70% Ni and σ equal to 2.5 GPa, c) 2.6 GPa, d) 3.3 GPa, and e) 3.8 GPa. The black atom is highlighted to show the transition of the L core in b) to the intermediate state in c).

For 70% Ni, there is a further transformation observed where a second nanotwin is nucleated to the right of the core as shown in Fig. 5.10e, with the Frank partial dislocation transitioning into a stair-rod partial. Presumably, if the cell sizes were larger, this second nanotwin would nucleate for other compositions in the range of 50%-100% Ni, as there is a driving force to do so. The reason this does not occur for these compositions is due to the partial dislocation associated with the first nanotwin approaching the GF region, which results in the simulation terminating after a maximum number of iterations.

The maximum magnitude of a force vector on an atom in the GF region at the terminated state below 50% Ni ranged from 0.30 eV/$\AA$ to 1.7 eV/$\AA$. This is due to the mixed dislocations in these states entering the GF region. In an infinite environment, it is expected that the mixed dislocations will continue to glide, especially since this starts early on in the GF relaxation cycle. For 50% Ni, the maximum force magnitude is 0.18 eV/$\AA$. While this is high, the state remains a nanotwin similar to the states found at lower values of σ. For compositions above 50% the maximum force magnitude ranged from 1.3×10^{-5} eV/$\AA$ to 1.2×10^{-3} eV/$\AA$, which are relatively low values. Additionally, the terminated states represent the formation of a nanotwin, which is consistent with the trend of the converged calculations in Fig. 5.10a.

5.4 Discussion

From the presented simulation results, it is clear that L and LC dislocations can attain a number of different configurations depending on the composition and applied shear stress state. We find that L dislocations can readily transform into LC configurations and vice versa. The ability for a LC dislocation to transform to a L configuration is in agreement with the analysis by Stroh [167] as well as TEM observations of glide on the (100) plane in a Cu-Al alloy, which has lower fault energies than pure Cu [170]. Additionally, the stresses at which glide on the (100) plane can occur at θ equal to 9.74° is lower for compositions that start with a LC configuration than for compositions that start with a L configuration. This suggests that the presence of a sessile SRP does not guarantee a stronger barrier against glide compared to the glissle L dislocation and that the role of fault energies are important. However, this depends on the value of θ, as for the cases where θ equals 45° or 35.26°, dislocations in environments with a higher Ni content began to glide while dislocations with lower Ni concentrations did not. The orientation dependence of the glide of these dislocations may play a role in the orientation dependence of work-hardening in single-crystal FCC alloys [150, 151].

The orientation dependence of work-hardening in FCC alloys may also be influenced by the orientation dependence of twin formation. We find the L and LC dislocations can nucleate an extrinsic stacking fault, or a nanotwin, when θ is equal to 0.5° or 35.26°. The values of σ to form a nanotwin at these orientations are quite high, beyond the values likely to be measured in tensile stress-strain curves of FCC alloys (an exception to this is the 1.9 GPa tensile strength observed in a compositionally complex steel which exhibited twinning in the FCC matrix [179]). However, high internal stresses can be achieved through mechanisms such as planar slip of dislocations, which is also orientation dependent [151]. Short-range ordering or clustering of solutes can also promote planar slip through slip-plane softening [87] and through the suppression of cross-slip [85]. While it is plausible that a local stress concentration can provide a source for twin nucleation from L and LC dislocations, there are a variety of possible twinning mechanisms in FCC metals and alloys that could be activated [159].

A number of assumptions were required to carry out the present study. We assumed that the stress state of the system could be described by linear elasticity, while in reality we are controlling the strain state. In pure Cu and Ni, we find that for high values of compressive and tensile strain in the x-direction, the bulk system (without a dislocation) starts to deviate from linear elasticity (Fig. S5 in the Supplementary Material document for this chapter). Accounting for this would require calculations of higher-order elastic constants. However, after measuring the stress state from the GF-region of converged dislocation structures in LAMMPS we found that other stress components did not have as strong of a deviation from the linear elasticity prediction (Fig. S6 in the Supplementary Material document for this chapter).

We have also assumed that the behavior of the dislocations under stress can be captured using a two-dimensional simulation. Thus, any change in core structure occurs homogeneously along the dislocation line. Studying the same dislocation behavior in a three-dimensional system may allow for changes to occur through the formation of a critical nucleus of a bow-out configuration of a fault [167] or of a kink-pair facilitating L dislocation glide [160]. Additionally, since the difference in energy between a L and LC dislocation is expected to be small [164], at temperature the cores may exhibit a polymorphic structure along the dislocation line, analogous to that recently observed in simulations of ⟨a⟩-type screw dislocations in hexagonal Ti [180]. A local variation of composition may also lead to a polymorphic structure. Exploring the formation of a critical nucleus requires knowledge of the initial and final states, a polymorphic structure at temperature is more likely to be found in regions of stress-composition space near core transitions, and the effect of local composition variation could be linked to different core structures available at different compositions. All of these considerations will be greatly facilitated by and motivated by the different core structures mapped out as a function of applied stress and composition in the current study.

5.5 Conclusions

We have presented results of atomistic simulations of L and LC dislocations in model FCC Cu-Ni alloys modeled with an average-atom potential, under various compositional and stress environments using a flexible boundary condition approach. We observe a variety of transformations, including L to LC, L to (100) glide, LC to L to (100) glide, L to nanotwin (and double nanotwin) nucleation, and LC to an obtuse configuration with a nanotwin. The variety of transformations under different values and orientations of pure shear stress are expected to play a role in the orientation dependence of work-hardening in FCC alloys.

Chapter 6

Summary and Future Work

6.1 Summary

The results presented in Chapters 3-5 provide guidelines for future mesoscale modeling of dislocation behavior associated with core reconfiguration.

In Chapter 3, we have shown that assuming a diffusion limited climb regime is only valid for relatively high homologous temperatures and point defect supersaturations. In FCC metals, this regime is narrowed down to even higher temperatures and point defect supersaturations when the stacking fault energy is low, as the jog-pair formation energy tends to be much higher than when the stacking fault energy is high. Thus, the common assumption of diffusion-limited climb in mesoscale models [16, 17, 18] is only applicable in strongly driven regimes, and it is otherwise necessary to account for the expected jog density along a dislocation in order to avoid overestimating the contribution of dislocation climb to creep. Doing so requires the calculation of jog-pair free energies from atomistic simulations.

In Chapter 4, we have shown that the presence of SRO modifies planar defect formation energies in such a way that significantly increases the cross-slip energy barrier compared to a random solid solution. Such an impact is expected to reduce the dynamic recovery rate in FCC alloys exhibiting SRO compared to random alloys. Mesoscale models typically do not incorporate the effect of solutes on cross-slip, with the exception of one study that assumed cross-slip energy barriers followed a distribution that mimics a random alloy [19]. As this study was not able to capture the features of planar slip expected to occur in alloys with SRO, we suspect that the contribution of SRO to cross-slip behavior in mesoscale models will result in more realistic dislocation microstructures.

In Chapter 5, we have shown that Lomer/Lomer-Cottrell dislocation cores can exhibit a variety of core structure configurations depending on the local composition and applied shear stress. As these dislocations act as barriers for the motion of other dislocations, the variety of core configurations available are expected to contribute to orientation dependent work-hardening behavior. Mesoscale models that include Lomer dislocations assume that the only reconfiguration available is through an “unzipping” mechanism [20, 21, 22]. The incorporation of the Lomer/Lomer-Cottrell core reconfiguration behavior found in Chapter 5 in mesoscale models is expected to influence the local dislocation morphology evolution near these dislocations.

6.2 Future Work

An important aspect to consider with the results presented in this dissertation is that they are largely obtained from simulations at zero temperature, thereby sampling the potential energy landscape of the various dislocation core reconfigurations. At finite temperature, it is desirable to sample the free energy landscape with contributions from vibrational entropy. This may lead to an increased jog density in Chapter 3, increased cross-slip rates in Chapter 4, and different regimes of dislocation core configurations in Chapter 5. Free energy barriers can be calculated using many MD trajectories [181], although such an approach is expected to be computationally expensive. Harmonic approaches offer a computationally efficient avenue to probe such effects, but are not reliable at high temperatures [182]. Regardless of the approach, extending the insights given in this dissertation to include vibrational effects would be crucial for understanding dislocation behavior at finite temperature. Additionally, finite temperature effects can cause low energy dislocation core structures to fluctuate to other core structures slightly higher in energy [180], which is expected to be relevant for cross-slip behavior and Lomer/Lomer-Cottrell dislocation core reconfigurations along a long dislocation line.

To truly explore the effects of this work on the evolution of ensembles of dislocations, it requires the incorporation of the presented results by relaxing previously mentioned assumptions in mesoscale models. This may not be entirely trivial to do as some of these assumptions allow for the expedient evaluation of these models, but will be necessary in order to bring meaningful connections between modeling and reality. Additionally, there are likely far more assumptions and missing physics in mesoscale modeling that have to be accounted for than discussed here. For example, a recent comparison between single crystal Cu compression tests in experiments and DDD simulations has shown that an orientation dependent mobility factor must be parameterized in order to obtain reasonable agreement between the two methods [183]. The parameterization of the mobility factor, which resulted in a value for both studied orientations that was lower than typically used in DDD simulations, suggests there is missing physics in current DDD formulations that would otherwise reduce dislocation mobility, such as dislocation intersections causing the formation of jogs or vacancies. In order to access meaningful connections between simulations and experiments, concerted, focused, and careful collaborations between experimentalists, mesoscale modelers, and atomistic modelers must be carried out to unravel the physics of plasticity. Such efforts may pave the way forward for physics-based modeling-enabled design of materials with optimal mechanical properties.

Bibliography

[1] D. Rodney, L. Ventelon, E. Clouet, L. Pizzagalli, and F. Willaime. “Ab initio modeling of dislocation core properties in metals and semiconductors”. In: *Acta Mater.* 124 (2017), pp. 633–659.

[2] L. A. Zepeda-Ruiz, A. Stukowski, T. Oppelstrup, N. Bertin, N. R. Barton, R. Freitas, and V. V. Bulatov. “Atomistic insights into metal hardening”. In: *Nature Materials* 20.3 (2021), pp. 315–320.

[3] V. Bulatov and W. Cai. *Computer simulations of dislocations.* Vol. 3. OUP Oxford, 2006.

[4] J. A. El-Awady. “Unravelling the physics of size-dependent dislocation-mediated plasticity”. In: *Nature Communications* 6.1 (2015), p. 5926.

[5] S. Rao, C. Woodward, B. Akdim, E. Antillon, T. Parthasarathy, J. El-Awady, and D. Dimiduk. “Large-scale dislocation dynamics simulations of strain hardening of Ni microcrystals under tensile loading”. In: *Acta Materialia* 164 (2019), pp. 171–183.

[6] A. Hunter, I. J. Beyerlein, T. C. Germann, and M. Koslowski. “Influence of the stacking fault energy surface on partial dislocations in fcc metals with a three-dimensional phase field dislocations dynamics model”. In: *Physical Review B* 84.14 (2011), p. 144108.

[7] Y. U. Wang, Y. M. Jin, A. M. Cuitiño, and A. G. Khachaturyan. “Phase field microelasticity theory and modeling of multiple dislocation dynamics”. In: *Applied Physics Letters* 78.16 (2001), pp. 2324–2326.

[8] S. Xu, J. Y. Cheng, Z. Li, N. A. Mara, and I. J. Beyerlein. “Phase-field modeling of the interactions between an edge dislocation and an array of obstacles”. In: *Computer Methods in Applied Mechanics and Engineering* 389 (2022), p. 114426.

[9] L. Cao, A. Hunter, I. J. Beyerlein, and M. Koslowski. “The role of partial mediated slip during quasi-static deformation of 3D nanocrystalline metals”. In: *Journal of the Mechanics and Physics of Solids* 78 (2015), pp. 415–426.

[10] D. Hull and D. J. Bacon. *Introduction to dislocations.* Elsevier, 2011.

[11] C. Varvenne, A. Luque, and W. A. Curtin. “Theory of strengthening in fcc high entropy alloys”. In: *Acta Materialia* 118 (2016), pp. 164–176.

[12] R. W. Balluffi. “Mechanisms of Dislocation Climb”. In: *physica status solidi (b)* 31.2 (1969), pp. 443–463.

[13] P. J. Jackson. “The role of cross-slip in the plastic deformation of crystals”. In: *Materials Science and Engineering* 57.1 (1983), pp. 39–47.

[14] W. Lomer. “A dislocation reaction in the face-centred cubic lattice”. In: *London, Edinburgh, Dublin Philos. Mag. J. Sci.* 42.334 (1951), pp. 1327–1331.

[15] A. Cottrell. “LX. The formation of immobile dislocations during slip”. In: *London, Edinburgh, Dublin Philos. Mag. J. Sci.* 43.341 (1952), pp. 645–647.

[16] D. Mordehai, E. Clouet, M. Fivel, and M. Verdier. “Introducing dislocation climb by bulk diffusion in discrete dislocation dynamics”. In: *Philosophical Magazine* 88.6 (2008), pp. 899–925.

[17] B. Bakó, E. Clouet, L. M. Dupuy, and M. Blétry. “Dislocation dynamics simulations with climb: kinetics of dislocation loop coarsening controlled by bulk diffusion”. In: *Philosophical Magazine* 91.23 (2011), pp. 3173–3191.

[18] S. M. Keralavarma, T. Cagin, A. Arsenlis, and A. A. Benzerga. “Power-law creep from discrete dislocation dynamics”. In: *Physical Review Letters* 109.26 (2012), p. 265504.

[19] M. Sudmanns and J. A. El-Awady. “The effect of local chemical ordering on dislocation activity in multi-principle element alloys: A three-dimensional discrete dislocation dynamics study”. In: *Acta Materialia* 220 (2021), p. 117307.

[20] V. B. Shenoy, R. V. Kukta, and R. Phillips. “Mesoscopic Analysis of Structure and Strength of Dislocation Junctions in fcc Metals”. In: *Phys. Rev. Lett.* 84.7 (2000), pp. 1491–1494.

[21] V. Bulatov, F. F. Abraham, L. Kubin, B. Devincre, and S. Yip. “Connecting atomistic and mesoscale simulations of crystal plasticity”. In: *Nature* 391.6668 (1998), pp. 669–672.

[22] R. Madec, B. Devincre, L. Kubin, T. Hoc, and D. Rodney. “The Role of Collinear Interaction in Dislocation-Induced Hardening”. In: *Science* 301.5641 (2003), pp. 1879–1882.

[23] M. S. Daw, S. M. Foiles, and M. I. Baskes. “The embedded-atom method: a review of theory and applications”. In: *Materials Science Reports* 9.7-8 (1993), pp. 251–310.

[24] M. I. Mendelev, M. J. Kramer, C. A. Becker, and M. Asta. “Analysis of semi-empirical interatomic potentials appropriate for simulation of crystalline and liquid Al and Cu”. In: *Philosophical Magazine* 88.12 (2008), pp. 1723–1750.

[25] G. P. Purja Pun and Y. Mishin. “Development of an interatomic potential for the Ni-Al system”. In: *Philosophical Magazine* 89.34-36 (2009), pp. 3245–3267.

[26] B. Onat and S. Durukanoğlu. “An optimized interatomic potential for Cu-Ni alloys with the embedded-atom method”. In: *J. Phys.: Condens. Matter* 26.3 (2014).

[27] C. Varvenne, A. Luque, W. G. Nöhring, and W. A. Curtin. “Average-atom interatomic potential for random alloys”. In: *Phys. Rev. B* 93.10 (2016), p. 104201.

[28] R. Najafabadi, H. Y. Wang, D. J. Srolovitz, and R. LeSar. “A new method for the simulation of alloys: Application to interfacial segregation”. In: *Acta Metallurgica Et Materialia* 39.12 (1991), pp. 3071–3082.

[29] M. Asta and S. M. Foiles. “Embedded-atom-method effective-pair-interaction study of the structural and thermodynamic properties of Cu-Ni, Cu-Ag, and Au-Ni solid solutions”. In: *Physical Review B - Condensed Matter and Materials Physics* 53.5 (1996), pp. 2389–2404.

[30] G. H. Vineyard. “Frequency factors and isotope effects in solid state rate processes”. In: *Journal of Physics and Chemistry of Solids* 3.1-2 (1957), pp. 121–127.

[31] G. Henkelman and H. Jónsson. “Improved tangent estimate in the nudged elastic band method for finding minimum energy paths and saddle points”. In: *Journal of Chemical Physics* 113.22 (2000), pp. 9978–9985.

[32] E. Maras, O. Trushin, A. Stukowski, T. Ala-Nissila, and H. Jónsson. “Global transition path search for dislocation formation in Ge on Si(001)”. In: *Computer Physics Communications* 205 (2016), pp. 13–21.

[33] G. Henkelman, B. P. Uberuaga, and H. Jónsson. “Climbing image nudged elastic band method for finding saddle points and minimum energy paths”. In: *Journal of Chemical Physics* 113.22 (2000), pp. 9901–9904.

[34] B. Sadigh, P. Erhart, A. Stukowski, A. Caro, E. Martinez, and L. Zepeda-Ruiz. “Scalable parallel Monte Carlo algorithm for atomistic simulations of precipitation in alloys”. In: *Physical Review B - Condensed Matter and Materials Physics* 85.18 (2012), p. 184203.

[35] D. Frenkel and B. Smit. *Understanding molecular simulation: from algorithms to applications.* Vol. 1. Elsevier, 2001.

[36] D. J. Tildesley and M. P. Allen. *Computer simulation of liquids.* Clarendon Oxford, 1987.

[37] W. Cai, V. V. Bulatob, J. Chang, J. Li, and S. Yip. “Periodic image effects in dislocation modelling”. In: *Philosophical Magazine* 83.5 (2003), pp. 539–567.

[38] M. S. Daw. “Elasticity effects in electronic structure calculations with periodic boundary conditions”. In: *Computational Materials Science* 38.2 (2006), pp. 293–297.

[39] E. Clouet, L. Ventelon, and F. Willaime. “Dislocation core energies and core fields from first principles”. In: *Physical Review Letters* 102.5 (2009), p. 055502.

[40] Y. Hu, B. A. Szajewski, D. Rodney, and W. A. Curtin. “Atomistic dislocation core energies and calibration of non-singular discrete dislocation dynamics”. In: *Modelling and Simulation in Materials Science and Engineering* 28.1 (2020), p. 015005.

[41] D. L. Olmsted, K. Y. Hardikar, and R. Phillips. “Lattice resistance and Peierls stress in finite size atomistic dislocation simulations”. In: *Modelling and Simulation in Materials Science and Engineering* 9.3 (2001), pp. 215–247.

[42] S. Rao, C. Hernandez, J. P. Simmons, T. A. Parthasarathy, and C. Woodward. “Green’s function boundary conditions in two-dimensional and three-dimensional atomistic simulations of dislocations”. In: *Philos. Mag. A* 77.1 (1998), pp. 231–256.

[43] D. L. Olmsted, L. G. Hector, W. A. Curtin, and R. J. Clifton. “Atomistic simulations of dislocation mobility in Al, Ni and Al/Mg alloys”. In: *Modelling and Simulation in Materials Science and Engineering* 13.3 (2005), pp. 371–388.

[44] S. Yin, Y. Zuo, A. Abu-Odeh, H. Zheng, X.-G. Li, J. Ding, S. P. Ong, M. Asta, and R. O. Ritchie. “Atomistic simulations of dislocation mobility in refractory high-entropy alloys and the effect of chemical short-range order”. In: *Nature Communications* 12.1 (2021), p. 4873.

[45] A. Abu-Odeh, D. L. Olmsted, and M. Asta. “Screw dislocation mobility in a face-centered cubic solid solution with short-range order”. In: *Scripta Materialia* 210 (2022), p. 114465.

[46] A. Abu-Odeh, M. Cottura, and M. Asta. “Insights into dislocation climb efficiency in FCC metals from atomistic simulations”. In: *Acta Materialia* 193 (2020), pp. 172–181.

[47] D. Caillard and J.-L. Martin. *Thermally activated mechanisms in crystal plasticity.* Vol. 8. Elsevier, 2003.

[48] P. M. Anderson, J. P. Hirth, and J. Lothe. *Theory of dislocations.* Cambridge University Press, 2017.

[49] P. S. Dobson, P. J. Goodhew, and R. E. Smallman. “Climb kinetics of dislocation loops in aluminium”. In: *Philosophical Magazine* 16.139 (1967), pp. 9–22.

[50] I. A. Johnston, P. S. Dobson, and R. E. Smallman. “The role of jog nucleation and propagation in the annealing of faulting loops in low stacking fault energy metals”. In: *Crystal Lattice Defects* 2 (1971), pp. 133–139.

[51] D. N. Seidman and R. W. Balluffi. “Dislocations as Source and Sinks for Point Defects in Metals”. In: *Lattice defects and their interactions.* Gordon and Breach Science Publishers, 1967, pp. 911–960.

[52] J. Silcox and M. J. Whelan. “Direct observations of the annealing of prismatic dislocation loops and of climb of dislocations in quenched aluminium”. In: *Philosophical Magazine* 5.49 (1960), pp. 1–23.

[53] C. A. Johnson. “The growth of prismatic dislocation loops during annealing”. In: *Philosophical Magazine* 5.60 (1960), pp. 1255–1265.

[54] T. D. Swinburne, K. Arakawa, H. Mori, H. Yasuda, M. Isshiki, K. Mimura, M. Uchikoshi, and S. L. Dudarev. “Fast, vacancy-free climb of prismatic dislocation loops in bcc metals”. In: *Scientific Reports* 6 (2016), p. 30596.

[55] D. N. Seidman and R. W. Balluffi. “On the Efficiency of Dislocation Climb in Gold”. In: *Physica Status Solidi (B)* 17.2 (1966), pp. 531–541.

[56] E. Martínez and B. P. Uberuaga. “Mobility and coalescence of stacking fault tetrahedra in Cu”. In: *Scientific Reports* 5.V (2015), pp. 1–5.

[57] Y. Gao, Z. Zhuang, Z. L. Liu, X. C. You, X. C. Zhao, and Z. H. Zhang. “Investigations of pipe-diffusion-based dislocation climb by discrete dislocation dynamics”. In: *International Journal of Plasticity* 27.7 (2011), pp. 1055–1071.

[58] X. Niu, T. Luo, J. Lu, and Y. Xiang. “Dislocation climb models from atomistic scheme to dislocation dynamics”. In: *Journal of the Mechanics and Physics of Solids* 99 (2017), pp. 242–258.

[59] C. Ayas, J. A. W. Van Dommelen, and V. S. Deshpande. “Climb-enabled discrete dislocation plasticity”. In: *Journal of the Mechanics and Physics of Solids* 62 (2014), pp. 113–136.

[60] J. H. Ke, A. Boyne, Y. Wang, and C. R. Kao. “Phase field microelasticity model of dislocation climb: Methodology and applications”. In: *Acta Materialia* 79 (2014), pp. 396–410.

[61] P. A. Geslin, B. Appolaire, and A. Finel. “A phase field model for dislocation climb”. In: *Applied Physics Letters* 104.1 (2014), p. 011903.

[62] P. A. Geslin, B. Appolaire, and A. Finel. “Multiscale Theory of Dislocation Climb”. In: *Physical Review Letters* 115.26 (2015), p. 265501.

[63] P. Liu, S. Zheng, K. Chen, X. Wang, B. Yan, P. Zhang, and S.-Q. Shi. “Point defect sink strength of low-angle tilt grain boundaries: A phase field dislocation climb model”. In: *International Journal of Plasticity* 119 (2019), pp. 188–199.

[64] Y. Gu, Y. Xiang, D. J. Srolovitz, and J. A. El-Awady. “Self-healing of low angle grain boundaries by vacancy diffusion and dislocation climb”. In: *Scripta Materialia* 155 (2018), pp. 155–159.

[65] X. X. Yu and C. Y. Wang. “The effect of alloying elements on the dislocation climbing velocity in Ni: A first-principles study”. In: *Acta Materialia* 57.19 (2009), pp. 5914–5920.

[66] S. Sarkar, J. Li, W. T. Cox, E. Bitzek, T. J. Lenosky, and Y. Wang. “Finding activation pathway of coupled displacive-diffusional defect processes in atomistics: Dislocation climb in fcc copper”. In: *Physical Review B* 86 (2012), p. 014115.

[67] K. L. Baker and W. A. Curtin. “Multiscale diffusion method for simulations of long-time defect evolution with application to dislocation climb”. In: *Journal of the Mechanics and Physics of Solids* 92 (2016), pp. 297–312.

[68] T. T. Lau, X. Lin, S. Yip, and K. J. Van Vliet. “Atomistic examination of the unit processes and vacancy-dislocation interaction in dislocation climb”. In: *Scripta Materialia* 60.6 (2009), pp. 399–402.

[69] M. Kabir, T. T. Lau, D. Rodney, S. Yip, and K. J. Van Vliet. "Predicting dislocation climb and creep from explicit atomistic details". In: *Physical Review Letters* 105.9 (2010), p. 095501.

[70] E. Clouet. "Predicting dislocation climb: Classical modeling versus atomistic simulations". In: *Physical Review B - Condensed Matter and Materials Physics* 84.9 (2011), p. 092106.

[71] E. Clouet. *Babel package.* (Visited on 07/30/2018).

[72] E. Clouet. *Étude par Simulations Numériques de la Plasticité dans les Métaux.* 2013.

[73] A. N. Stroh. "Dislocations and Cracks in Anisotropic Elasticity". In: *Journal of Theoretical Experimental and Applied Physics* 330 (1958), pp. 625–646.

[74] A. N. Stroh. "Steady State Problems in Anisotropic Elasticity". In: *Journal of Mathematics and Physics* 41.1-4 (1962), pp. 77–103.

[75] E. Bitzek, P. Koskinen, F. Gähler, M. Moseler, and P. Gumbsch. "Structural Relaxation Made Simple". In: *Physical Review Letters* 97.17 (2006), p. 170201.

[76] S. Plimpton. "Fast parallel algorithms for short-range molecular dynamics". In: *Journal of Computational Physics* 117.1 (1995), pp. 1–19.

[77] A. Stukowski. "Visualization and analysis of atomistic simulation data with OVITO-the Open Visualization Tool". In: *Modelling and Simulation in Materials Science and Engineering* 18.1 (2010), p. 015012.

[78] A. Stukowski. "Structure identification methods for atomistic simulations of crystalline materials". In: *Modelling and Simulation in Materials Science and Engineering* 20.4 (2012), p. 045021.

[79] M. Landeiro Dos Reis, L. Proville, and M. Sauzay. "Modeling the climb-assisted glide of edge dislocations through a random distribution of nanosized vacancy clusters". In: *Physical Review Materials* 2 (2018), p. 93604.

[80] G. P. Purja Pun and Y. Mishin. "A molecular dynamics study of self-diffusion in the cores of screw and edge dislocations in aluminum". In: *Acta Materialia* 57.18 (2009), pp. 5531–5542.

[81] J. Huang, M. Meyer, and V. Pontikis. "Migration of point defects along a dissociated edge dislocation in copper: a molecular dynamics study of pipe diffusion". In: *Philosophical Magazine A* 63.6 (1991), pp. 1149–1165.

[82] J. Grilhé, M. Boisson, K. Seshan, and R. J. Gaboriaud. "Climb model of extended dislocations in f.c.c. metals". In: *Philosophical Magazine* 36.4 (1977), pp. 923–930.

[83] P. B. Hirsch. "Extended Jogs in Dislocations in Face-centred Cubic Metals". In: *Philosophical Magazine* 7.73 (1962), pp. 67–93.

[84] D. Carpentier, T. Jourdan, Y. Le Bouar, and M.-C. Marinica. "Effect of saddle point anisotropy of point defects on their absorption by dislocations and cavities". In: *Acta Materialia* 136 (2017), pp. 323–334.

[85] A. Abu-Odeh and M. Asta. “Modeling the effect of short-range order on cross-slip in an FCC solid solution”. In: *Acta Mater.* 226 (2022), p. 117615.

[86] N. Clément, D. Caillard, and J. L. Martin. “Heterogeneous deformation of concentrated NiCr F.C.C. alloys: Macroscopic and microscopic behaviour”. In: *Acta Metallurgica* 32.6 (1984), pp. 961–975.

[87] V. Gerold and H. P. Karnthaler. “On the origin of planar slip in f.c.c. alloys”. In: *Acta Metallurgica* 37.8 (1989), pp. 2177–2183.

[88] J. Plessing, C. Achmus, H. Neuhäuser, B. Schönfeld, and G. Kostorz. “Short-Range Order and the Mode of Slip in Concentrated Cu-based Alloys”. In: *Zeitschrift für Metallkunde* 88.8 (1997), pp. 630–635.

[89] D. Han, Z. Y. Wang, Y. Yan, F. Shi, and X. W. Li. “A good strength-ductility match in Cu-Mn alloys with high stacking fault energies: Determinant effect of short range ordering”. In: *Scripta Materialia* 133 (2017), pp. 59–64.

[90] D. Han, X. J. Guan, Y. Yan, F. Shi, and X. W. Li. “Anomalous recovery of work hardening rate in Cu-Mn alloys with high stacking fault energies under uniaxial compression”. In: *Materials Science and Engineering A* 743.August 2018 (2019), pp. 745–754.

[91] Y. J. Zhang, D. Han, and X. W. Li. “A unique two-stage strength-ductility match in low solid-solution hardening Ni-Cr alloys: Decisive role of short range ordering”. In: *Scripta Materialia* 178 (2020), pp. 269–273.

[92] R. Zhang, S. Zhao, J. Ding, Y. Chong, T. Jia, C. Ophus, M. Asta, R. O. Ritchie, and A. M. Minor. “Verification of Short-Range Order and Its Impact on the Properties of the CrCoNi Medium Entropy Alloy”. In: *Nature* 581.7808 (2020), pp. 283–287.

[93] D. Han, Y. Zhang, and X. Li. “A crucial impact of short-range ordering on the cyclic deformation and damage behavior of face-centered cubic alloys: A case study on Cu-Mn alloys”. In: *Acta Materialia* 205 (2021), p. 116559.

[94] F. He, S. Wei, J. L. Cann, Z. Wang, J. Wang, and C. C. Tasan. “Composition-dependent slip planarity in mechanically-stable face centered cubic complex concentrated alloys and its mechanical effects”. In: *Acta Materialia* 220 (2021), p. 117314.

[95] J. C. Fisher. “On the strength of solid solution alloys”. In: *Acta Metallurgica* 2.1 (1954), pp. 9–10.

[96] J. Ding, Q. Yu, M. Asta, and R. O. Ritchie. “Tunable stacking fault energies by tailoring local chemical order in CrCoNi medium-entropy alloys”. In: *Proceedings of the National Academy of Sciences of the United States of America* 115.36 (2018), pp. 8919–8924.

[97] S. I. Hong and C. Laird. “Mechanisms of slip mode modification in F.C.C. solid solutions”. In: *Acta Metallurgica Et Materialia* 38.8 (1990), pp. 1581–1594.

[98] W. G. Nöhring and W. A. Curtin. “Dislocation cross-slip in fcc solid solution alloys”. In: *Acta Materialia* 128 (2017), pp. 135–148.

[99] W. G. Nöhring and W. A. Curtin. “Cross-slip of long dislocations in FCC solid solutions”. In: *Acta Materialia* 158 (2018), pp. 95–117.

[100] F. Otto, A. Dlouhý, C. Somsen, H. Bei, G. Eggeler, and E. P. George. “The influences of temperature and microstructure on the tensile properties of a CoCrFeMnNi high-entropy alloy”. In: *Acta Materialia* 61.15 (2013), pp. 5743–5755.

[101] P. Jackson. “Dislocation modelling of shear in f.c.c. crystals”. In: *Progress in Materials Science* 29.1-2 (1985), pp. 139–175.

[102] J. M. Cowley. “An approximate theory of order in alloys”. In: *Physical Review* 77.5 (1950), pp. 669–675.

[103] P. A. Flinn. “Solute hardening of close-packed solid solutions”. In: *Acta Metallurgica* 6.10 (1958), pp. 631–635.

[104] T. Mohri, D. de Fontaine, and J. M. Sanchez. “Short range order hardening with second neighbor interactions in fcc solid solutions”. In: *Metallurgical transactions. A, Physical metallurgy and materials science* 17 A.2 (1986), pp. 189–194.

[105] T. Mohri, J. Tsutsumi, O. Sasaki, and K. Watanabe. “Computer simulation study of short-range order hardening”. In: *Metallurgical transactions. A, Physical metallurgy and materials science* 21 A.12 (1990), pp. 3165–3169.

[106] P. Schwander, B. Schönfeld, and G. Kostorz. “Configurational Energy Change Caused by Slip in Short-Range Ordered Ni–Mo”. In: *Physica Status Solidi (B)* 172.1 (1992), pp. 73–85.

[107] B. Schönfeld and P. Schwander. “Slip Induced Configurational Energy Change in Binary Alloys”. In: *Stability of Materials*. 1996, pp. 657–662.

[108] A. van de Walle and M. Asta. “First-principles investigation of perfect and diffuse antiphase boundaries in HCP-based Ti-Al alloys”. In: *Metallurgical and Materials Transactions A* 33.3 (2002), pp. 735–741.

[109] Q. J. Li, H. Sheng, and E. Ma. “Strengthening in multi-principal element alloys with local-chemical-order roughened dislocation pathways”. In: *Nature Communications* 10.1 (2019).

[110] E. Antillon, C. Woodward, S. I. Rao, B. Akdim, and T. A. Parthasarathy. “Chemical short range order strengthening in a model FCC high entropy alloy”. In: *Acta Materialia* 190 (2020), pp. 29–42.

[111] W.-R. Jian, Z. Xie, S. Xu, Y. Su, X. Yao, and I. J. Beyerlein. “Effects of lattice distortion and chemical short-range order on the mechanisms of deformation in medium entropy alloy CoCrNi”. In: *Acta Materialia* (2020).

[112] Y. Zeng, X. Cai, and M. Koslowski. “Effects of the stacking fault energy fluctuations on the strengthening of alloys”. In: *Acta Materialia* 164 (2019), pp. 1–11.

[113] L. T. Smith, Y. Su, S. Xu, A. Hunter, and I. J. Beyerlein. "The effect of local chemical ordering on Frank-Read source activation in a refractory multi-principal element alloy". In: *International Journal of Plasticity* 134 (2020), p. 102850.

[114] K. Kang, J. Yin, and W. Cai. "Stress dependence of cross slip energy barrier for face-centered cubic nickel". In: *Journal of the Mechanics and Physics of Solids* 62.1 (2014), pp. 181–193.

[115] E. Oren, E. Yahel, and G. Makov. "Kinetics of dislocation cross-slip: A molecular dynamics study". In: *Computational Materials Science* 138 (2017), pp. 246–254.

[116] S. Xu, L. Xiong, Y. Chen, and D. L. McDowell. "Shear stress- and line length-dependent screw dislocation cross-slip in FCC Ni". In: *Acta Materialia* 122 (2017), pp. 412–419.

[117] G. Esteban-Manzanares, R. Santos-Güemes, I. Papadimitriou, E. Martínez, and J. LLorca. "Influence of the stress state on the cross-slip free energy barrier in Al: An atomistic investigation". In: *Acta Materialia* 184 (2020), pp. 109–119.

[118] W. P. Kuykendall, Y. Wang, and W. Cai. "Stress effects on the energy barrier and mechanisms of cross-slip in FCC nickel". In: *Journal of the Mechanics and Physics of Solids* 144 (2020), p. 104105.

[119] J. P. Du, C. Y. Wang, and T. Yu. "Cross-slip process in model Ni(Al) solid solution: An embedded-atom method study". In: *Computational Materials Science* 91 (2014), pp. 192–199.

[120] S. I. Rao, C. Woodward, T. A. Parthasarathy, and O. Senkov. "Atomistic simulations of dislocation behavior in a model FCC multicomponent concentrated solid solution alloy". In: *Acta Materialia* 134 (2017), pp. 188–194.

[121] F. Klaiber, B. Schönfeld, and G. Kostorz. "Investigation of short-range order in Ni–10 at.% Al single crystals by diffuse X-ray scattering". In: *Acta Crystallographica Section A* 43.4 (1987), pp. 525–533.

[122] F. Chassagne, M. Bessiere, Y. Calvayrac, P. Cenedese, and S. Lefebvre. "X-ray diffuse scattering investigation of different states of local order in Ni-Al solid solutions". In: *Acta Metallurgica* 37.9 (1989), pp. 2329–2338.

[123] B. Schönfeld, L. Reinhard, G. Kostorz, and W. Bührer. "Short-Range Order and Atomic Displacements in Ni–20 at% Cr Single Crystals". In: *physica status solidi (b)* 148.2 (1988), pp. 457–471.

[124] W. Schweika and H. G. Haubold. "Neutron-scattering and Monte Carlo study of short-range order and atomic interaction in Ni0.89Cr0.11". In: *Physical Review B* 37.16 (1988), pp. 9240–9248.

[125] R. Caudron, M. Sarfati, M. Barrachin, A. Finel, F. Ducastelle, and F. Solal. "In situ diffuse scattering of neutrons in alloys and application to phase diagram determination". In: *Journal de Physique I* 2.6 (1992), pp. 1145–1171.

[126] J. S. Wróbel, D. Nguyen-Manh, M. Y. Lavrentiev, M. Muzyk, and S. L. Dudarev. “Phase stability of ternary fcc and bcc Fe-Cr-Ni alloys”. In: *Physical Review B - Condensed Matter and Materials Physics* 91.2 (2015), p. 24108.

[127] S. C. Moss. “X-Ray Measurement of Short-Range Order in Cu 3 Au”. In: *Journal of Applied Physics* 35.12 (1964), pp. 3547–3553.

[128] B. Schönfeld, M. J. Portmann, S. Y. Yu, and G. Kostorz. “Type of order in Cu-10 at.% Au - evidence from the diffuse scattering of X-rays”. In: *Acta Materialia* 47.5 (1999), pp. 1413–1416.

[129] L. Reinhard, B. Schönfeld, G. Kostorz, and W. Bührer. “Short-range order in α-brass”. In: *Physical Review B* 41.4 (1990), pp. 1727–1734.

[130] H. Roelofs, B. Schönfeld, G. Kostorz, and W. Büher. “Atomic Short-Range Order in Cu-17 at% Mn”. In: *physica status solidi (b)* 187.1 (1995), pp. 31–42.

[131] B. Schönfeld, R. Bucher, G. Kostorz, and M. Zolliker. “Magnetic and atomic short-range order in Cu-rich Cu-Mn”. In: *Physical Review B* 69.22 (2004), p. 224205.

[132] B. Schönfeld, H. Roelofs, A. Malik, G. Kostorz, J. Plessing, and H. Neuhäuser. “The microstructure of Cu-Al”. In: *Acta Materialia* 44.1 (1996), pp. 335–342.

[133] J. Guénolé, W. G. Nöhring, A. Vaid, F. Houllé, Z. Xie, A. Prakash, and E. Bitzek. “Assessment and optimization of the fast inertial relaxation engine (FIRE) for energy minimization in atomistic simulations and its implementation in LAMMPS”. In: *Computational Materials Science* 175 (2020), p. 109584.

[134] F. Pettinari-Sturmel, J. Douin, A. Coujou, and N. Clément. “Characterisation of short-range order using dislocations”. In: *Zeitschrift fuer Metallkunde/Materials Research and Advanced Techniques* 97.3 (2006), pp. 200–204.

[135] P. Hirel. “Atomsk: A tool for manipulating and converting atomic data files”. In: *Computer Physics Communications* 197 (2015), pp. 212–219.

[136] P. Virtanen, R. Gommers, T. E. Oliphant, M. Haberland, T. Reddy, D. Cournapeau, E. Burovski, P. Peterson, W. Weckesser, J. Bright, S. J. van der Walt, M. Brett, J. Wilson, K. J. Millman, N. Mayorov, A. R. J. Nelson, E. Jones, R. Kern, E. Larson, C. J. Carey, İ. Polat, Y. Feng, E. W. Moore, J. VanderPlas, D. Laxalde, J. Perktold, R. Cimrman, I. Henriksen, E. A. Quintero, C. R. Harris, A. M. Archibald, A. H. Ribeiro, F. Pedregosa, P. van Mulbregt, and SciPy 1.0 Contributors. “SciPy 1.0: Fundamental Algorithms for Scientific Computing in Python”. In: *Nature Methods* 17 (2020), pp. 261–272.

[137] C. H. Henager and R. G. Hoagland. “Dislocation and stacking fault core fields in fcc metals”. In: *Philosophical Magazine* 85.36 (2005), pp. 4477–4508.

[138] B. Efron. “Nonparametric estimates of standard error: The jackknife, the bootstrap and other methods”. In: *Biometrika* 68.3 (1981), pp. 589–599.

[139] S. Nag and W. A. Curtin. “Effect of solute-solute interactions on strengthening of random alloys from dilute to high entropy alloys”. In: *Acta Materialia* 200 (2020), pp. 659–673.

[140] L. Zhang, Y. Xiang, J. Han, and D. J. Srolovitz. “The effect of randomness on the strength of high-entropy alloys”. In: *Acta Materialia* 166 (2019), pp. 424–434.

[141] G. Saada, J. Douin, F. Pettinari-Sturmel, A. Coujou, and N. Clément. “Pile-ups in thin foils: Application to transmission electron microscopy analysis of short-range-order”. In: *Philosophical Magazine* 84.8 (2004), pp. 807–824.

[142] T. C. Pekin, C. Gammer, J. Ciston, C. Ophus, and A. M. Minor. “In situ nanobeam electron diffraction strain mapping of planar slip in stainless steel”. In: *Scripta Materialia* 146 (2018), pp. 87–90.

[143] R. Ahmad, Z. Wu, and W. A. Curtin. “Analysis of double cross-slip of pyramidal I screw dislocations and implications for ductility in Mg alloys”. In: *Acta Materialia* (2019).

[144] T. Hatano, T. Kaneko, Y. Abe, and H. Matsui. “Void-induced cross slip of screw dislocations in fcc copper”. In: *Physical Review B - Condensed Matter and Materials Physics* 77.6 (2008), pp. 1–6.

[145] H. Mughrabi and R. Wang. “Cyclic Strain Localization and Fatigue Crack Initiation in Persistent Slip Bands in Face-Centred Cubic Metals and Single-Phase Alloys”. In: *Defects and Fracture*. Dordrecht: Springer Netherlands, 1982, pp. 15–28. ISBN: 9024725364.

[146] F. Hamdi and S. Asgari. “Influence of stacking fault energy and short-range ordering on dynamic recovery and work hardening behavior of copper alloys”. In: *Scripta Materialia* 62.9 (2010), pp. 693–696.

[147] U. F. Kocks. “Laws for Work-Hardening and Low-Temperature Creep”. In: *Journal of Engineering Materials and Technology* 98.1 (1976), pp. 76–85.

[148] A. Abu-Odeh, T. Allaparti, and M. Asta. “Structure and glide of Lomer and Lomer-Cottrell dislocations: Atomistic simulations for model concentrated alloy solid solutions”. In: *Physical Review Materials* 6.10 (2022), p. 103603.

[149] J. Friedel. “CXXX. On the linear work hardening rate of face-centred cubic single crystals”. In: *London, Edinburgh, Dublin Philos. Mag. J. Sci.* 46.382 (1955), pp. 1169–1186.

[150] B. Uzer, S. Picak, J. Liu, T. Jozaghi, D. Canadinc, I. Karaman, Y. Chumlyakov, and I. Kireeva. “On the mechanical response and microstructure evolution of NiCoCr single crystalline medium entropy alloys”. In: *Mater. Res. Lett.* 6.8 (2018), pp. 442–449.

[151] S. Picak, J. Liu, C. Hayrettin, W. Nasim, D. Canadinc, K. Xie, Y. Chumlyakov, I. Kireeva, and I. Karaman. “Anomalous work hardening behavior of Fe40Mn40Cr10Co10 high entropy alloy single crystals deformed by twinning and slip”. In: *Acta Mater.* 181 (2019), pp. 555–569.

[152] X. D. Xu, P. Liu, Z. Tang, A. Hirata, S. X. Song, T. G. Nieh, P. K. Liaw, C. T. Liu, and M. W. Chen. “Transmission electron microscopy characterization of dislocation structure in a face-centered cubic high-entropy alloy Al0.1CoCrFeNi”. In: *Acta Mater.* 144 (2018), pp. 107–115.

[153] Y. Ma, F. Yuan, M. Yang, P. Jiang, E. Ma, and X. Wu. “Dynamic shear deformation of a CrCoNi medium-entropy alloy with heterogeneous grain structures”. In: *Acta Mater.* 148 (2018), pp. 407–418.

[154] X. Gao, Y. Lu, J. Liu, J. Wang, T. Wang, and Y. Zhao. “Extraordinary ductility and strain hardening of Cr26Mn20Fe20Co20Ni14 TWIP high-entropy alloy by cooperative planar slipping and twinning”. In: *Materialia* 8.June (2019), p. 100485.

[155] L. Qi, C. Q. Liu, H. W. Chen, and J. F. Nie. “Atomic scale characterization of complex stacking faults and their configurations in cold deformed Fe42Mn38Co10Cr10 high-entropy alloy”. In: *Acta Mater.* 199 (2020), pp. 649–668.

[156] J. Wang, H. Yang, H. Huang, J. Zou, S. Ji, and Z. Liu. “High strength-ductility Co23Cr23Ni23Mn31 medium-entropy alloy achieved via defect engineering”. In: *Mater. Sci. Eng., A* 796.August (2020), p. 139974.

[157] J. Cohen and J. Weertman. “A dislocation model for twinning in f.c.c. metals”. In: *Acta Metall.* 11.8 (1963), pp. 996–998.

[158] I. Karaman, H. Sehitoglu, K. Gall, Y. I. Chumlyakov, and H. J. Maier. “Deformation of single crystal hadfield steel by twinning and slip”. In: *Acta Mater.* 48.6 (2000), pp. 1345–1359.

[159] B. C. De Cooman, Y. Estrin, and S. K. Kim. “Twinning-induced plasticity (TWIP) steels”. In: *Acta Mater.* 142 (2018), pp. 283–362.

[160] D. Rodney. “Activation enthalpy for kink-pair nucleation on dislocations: Comparison between static and dynamic atomic-scale simulations”. In: *Phys. Rev. B* 76.14 (2007), p. 144108.

[161] M. Carrard and J. L. Martin. “A study of (001) glide in [112] aluminium single crystals II. Microscopic mechanism”. In: *Philos. Mag. A* 58.3 (1988), pp. 491–505.

[162] M. J. Mills and P. Stadelmann. “A study of the structure of Lomer and 60° dislocations in aluminium using high-resolution transmission electron microscopy”. In: *Philos. Mag. A* 60.3 (1989), pp. 355–384.

[163] G. Saada and J. Douin. “On the stability of dissociated dislocations”. In: *Philos. Mag. Lett.* 64.2 (1991), pp. 67–70.

[164] F. Gao and D. J. Bacon. “On the structure and energy of dissociated dislocations in F.C.C. metals”. In: *Philos. Mag. A* 66.5 (1992), pp. 839–847.

[165] A. Korner, H. Schmid, and F. Prinz. “Asymmetrical equilibrium postions and line tensions of composite dislocations”. In: *Phys. Status Solidi A* 51.2 (1979), pp. 613–621.

[166] J. Bonneville and J. Douin. “On the asymmetrical dissociation of lomer dislocations”. In: *Philos. Mag. Lett.* 62.4 (1990), pp. 247–251.

[167] A. N. Stroh. “LI. The strength of lomer-cottrell sessile dislocations”. In: *Philos. Mag.* 1.6 (1956), pp. 489–502.

[168] D. Rodney and R. Phillips. “Structure and Strength of Dislocation Junctions: An Atomic Level Analysis”. In: *Phys. Rev. Lett.* 82.8 (1999), pp. 1704–1707.

[169] A. Korner and H. P. Karnthaler. “The study of glide dislocation loops on 001 planes in a f.c.c. alloy”. In: *Philos. Mag. A* 42.6 (1980), pp. 753–762.

[170] A. Korner and H. P. Karnthaler. “Glide dislocations on cube planes in a low stacking-fault energy alloy”. In: *Phys. Status Solidi A* 75.2 (1983), pp. 525–535.

[171] D. R. Trinkle. “Lattice Green function for extended defect calculations: Computation and error estimation with long-range forces”. In: *Phys. Rev. B* 78.1 (2008), p. 014110.

[172] M. Ghazisaeidi and D. R. Trinkle. “Convergence rate for numerical computation of the lattice Green’s function”. In: *Phys. Rev. E* 79.3 (2009), p. 037701.

[173] A. M. Z. Tan and D. R. Trinkle. “Computation of the lattice Green function for a dislocation”. In: *Phys. Rev. E* 94.2 (2016), p. 023308.

[174] L. Anand and S. Govindjee. *Continuum mechanics of solids*. Oxford University Press, 2020.

[175] C. R. Weinberger and W. Cai. “The stability of Lomer–Cottrell jogs in nanopillars”. In: *Scr. Mater.* 64.6 (2011), pp. 529–532.

[176] A. Stukowski and K. Albe. “Extracting dislocations and non-dislocation crystal defects from atomistic simulation data”. In: *Modell. Simul. Mater. Sci. Eng.* 18.8 (2010), p. 085001.

[177] V. Vítek, R. C. Perrin, and D. K. Bowen. “The core structure of $\frac{1}{2}(111)$ screw dislocations in b.c.c. crystals”. In: *Philos. Mag.* 21.173 (1970), pp. 1049–1073.

[178] M. I. Baskes, R. G. Hoagland, and T. Tsuji. “An atomistic study of the strength of an extended-dislocation barrier”. In: *Modell. Simul. Mater. Sci. Eng.* 6.1 (1998), pp. 9–18.

[179] Z. Wang, W. Lu, F. An, M. Song, D. Ponge, D. Raabe, and Z. Li. “High stress twinning in a compositionally complex steel of very high stacking fault energy”. In: *Nat. Commun.* 13.1 (2022), p. 3598.

[180] M. Poschmann, I. S. Winter, M. Asta, and D. C. Chrzan. “Molecular dynamics studies of a-type screw dislocation core structure polymorphism in titanium”. In: *Phys. Rev. Mater.* 6.1 (2022), p. 013603.

[181] T. D. Swinburne and M.-C. Marinica. “Unsupervised Calculation of Free Energy Barriers in Large Crystalline Systems”. In: *Physical Review Letters* 120.13 (2018), p. 135503.

[182] S. M. Foiles. “Evaluation of harmonic methods for calculating the free energy of defects in solids”. In: *Physical Review B* 49.21 (1994), pp. 14930–14938.

[183] S. Akhondzadeh, M. Kang, R. B. Sills, K. Ramesh, and W. Cai. “Direct comparison between experiments and dislocation dynamics simulations of high rate deformation of single crystal copper”. In: *Acta Materialia* 250.March (2023), p. 118851.